Detecting Supermassive Black Hole Binaries with LISA

Dissertation

zur

Erlangung der naturwissenschaftlichen Doktorwürde
(Dr. sc. nat.)

vorgelegt der

Mathematisch-naturwissenschaftlichen Fakultät

der

Universität Zürich

von

Antoine Klein

von

La Baroche, JU

Promotionskomitee

Prof. Dr. Philippe Jetzer (Vorsitz)
Prof. Dr. Monica Colpi
Prof. Dr. Daniel Wyler

Zürich, 2011

Abstract

Gravitational waves are predicted by General Relativity to be emitted by binary systems, and to take away from them rotational energy. The observation of the loss of angular momentum by binary pulsar systems has been a major success of this theory, although gravitational waves have not yet been directly observed.

Once the direct detection of gravitational waves is made possible, it will allow observations in a regime that would not be accessible by other means. General Relativity is a very successful theory, as it has been able to explain every observable effect of gravitation that we have measured so far. However, all of these tests were made in the weak field regime, i.e. far from the source of the gravitational field, where the deviations from Newtonian theory are small. The most promising source of gravitational waves for next generation detectors are compact object mergers, which probe the strongest gravitational fields accessible in our Universe. On a different level, gravitational waves are emitted by any massive object, and do not need the source to be interacting electromagnetically. Thus, gravitational wave detectors could be a powerful tool to measure the properties and distribution of compact objects such as black holes, neutron stars, or white dwarves inside a galaxy, the observation of which is difficult or impossible with conventional astronomy instruments.

In this thesis, we focus on the planned space-based interferometer LISA, designed to be most sensitive to systems containing a supermassive black hole (of mass $\gtrsim 10^5$ Solar masses). In particular, we build wave templates, or waveforms, for comparable mass binary systems, including various known physical effects that affect these systems, and estimate the precision that the use of these waveforms would induce for LISA.

In Chapter 1, we present a brief history of parameter estimation in the context of LISA, and discuss general properties of gravitational waves, how they can be detected by laser interferometers, and how they are produced by binary systems. In Chapter 2, we focus on LISA and how its configuration affects the observed signal of a monochromatic gravitational wave. We also introduce the different data analysis techniques that we used for parameter estimation. In Chapter 3, we describe the different physical effects that can affect a waveform, and define the different waveforms that we used in our studies. In Chapter 4, we present the outcome of the study that we performed using circular templates, comparing waveforms with spin-orbit precession, with or without subdominant harmonics and amplitude modulation. In Chapter 5, we present a current study that we are performing using eccentric templates. Finally, we summarize our results in Chapter 6.

Zusammenfassung

Nach der Allgemeinen Relativitätstheorie werden Gravitationswellen von binären Systemen emittiert, die dadurch ihre Rotationsenergie reduzieren. Die Beobachtung des Drehimplusabfalls von binären Pulsarsystemen ist ein grosser Erfolg dieser Theorie, obwohl Gravitationswellen noch nicht direkt beobachtet wurden.

Sobald die direkte Messung von Gravitationswellen ermöglicht wird, werden Beobachtungen in einem Bereich ermöglicht, der mit anderen Methoden unerreichbar ist. Die Allgemeine Relativität ist so erfolgreich, weil sie alle beobachtbaren Effekte der Gravitation erklären kann, die man bis jetzt gemessen hat. Allerdings wurden alle diese Tests für schwache Felder durchgeführt, d.h. weit entfernt von der Quelle des Gravitationsfeldes, wo die Abweichungen von der Newtonschen Theorie klein sind. Die aussichtsreichsten Quellen von Gravitationswellen für Detektoren der nächsten Generation sind Verschmelzungen von kompakten Objekten, welche die stärksten Gravitationsfelder unseres Universums prüfen. Anderseits werden Gravitationswellen von beliebigen massbehafteten Objekten emittiert, wobei die Quelle nicht elektromagnetisch zu wechselwirken braucht. Deshalb wären Gravitationswellen Detektoren ein grosses Hilfsmittel um die Eigenschaften und die Verteilung kompakter Objekte wie schwarzer Löcher, Neutronsterne oder weisser Zwerge innerhalb einer Galaxie zu messen, Beobachtungen die mit konventionalen astronomischen Instrumente schwierig oder unmöglich sind.

Die vorliegende Arbeit beschäftigt sich mit dem geplanten Weltraum-Interferometer LISA, welches am sensibelsten für Systeme angelegt ist, die ein supermassives schwarzes Loch (der Masse $\gtrsim 10^5$ Sonnenmassen) enthalten. Insbesondere entwickeln wir Wellentemplates, oder Wellenformen, für binäre Systeme vergleichbarer Masse, wobei wir verschiedene bekannte physikalische Effekte einbauen, die diese Systeme beeinflussen, und die Präzision abschätzen, die die Anwendung dieser Wellentemplates für LISA verursachen würde.

In Kapitel 1 legen wir eine kurze Zusammenfassung für die Parameter-Abschätzung im LISA-Kontext dar und behandeln allgemeine Eigenschaften von Gravitationswellen: wie sie von Laser-Interferometern gemessen werden können, und wie sie von binären Systemen produziert werden. In Kapitel 2 konzentrieren wir uns auf LISA, und wie dessen Konfiguration das gemessene Signal einer monochromatischen Gravitationswelle beeinflusst. Wir führen auch die verschiedenen Methoden der Datenanalyse ein, die wir für die Parameter-Abschätzung angewendet haben. In Kapitel 3 beschreiben wir die verschiedenen Effekte, die die Wellenform beeinflussen können, und definieren die verschiedenen Wellenformen, die wir in unseren Studien angewendet haben. In Kapitel 4 präsentieren wir die Resultate einer Studie, die wir mit kreisförmigen Templates durchgeführt haben, um Wellenformen mit Spin-Orbit Präzession zu vergleichen, jeweils mit oder ohne untergeordnetet Oberwellen und Amplituden Modulation. In Kapitel 5 beschreiben wir eine aktuelle Studie, die wir mit exzentrischen Templates durchführen. Schliesslich fassen wir unsere Resultate in Kapitel 6 zusammen.

Acknowledgements

First of all, I am most grateful to my PhD supervisor Philippe Jetzer with whom it has been a real pleasure to work. His scientific insight has been greatly influential on the direction of my research, and his advice has always helped me going forward. Furthermore, he is a very nice person, whom it is very pleasant to talk to.

The working atmosphere in Zurich has been really stimulating and enjoyable during my whole stay here, thanks to the fantastic people that make our institute. They include, but are not limited to, Aaron, Aaron, Andreas, Andreas, Aurel, Ben, Cedric, Cedric, Christian, Christine, Crescenzo, Daniel, Dan, Darren, Davide, Donnino, Doug, Erich, Fabiana, Fabio, Francis, George, Gianfranco, Hana, Jaiyul, Joachim, Joachim, Jonathan, Jonathan, José, Justin, Lea, Lorenzo, Lucas, Lucia, Lucio, Marina, Mario, Marc, Marco, Michael, Miguel, Nico, Nico, Oskar, Pier Francesco, Pedro, Pedro, Philipp, Philippe, Prasenjit, Ray, Rikkert, Robert, Rok, Romain, Sebastian, Simone, Suzanne, Teppei, Thomas, Thomas, Timo, Tina, Tobias, Tobias, Vincent, Zvonimir. My deepest apologies for those whose name I forgot to put on the list, I did not mean to. Thank you all for making life in Zurich such a great experience. Special thanks to Ray, who carefully proof-read everything I have written here, adding a significant amount of clarity to it. Special thanks also to Nico, who took the time to correct every second word of what I thought was a good German text, saving me from the shame of publishing it as it was.

I am also grateful to my friends in Lausanne, whom it is always a pleasure to visit. Special thanks to Nicos for stimulating discussions, and to Przemek for is coding advice when I really needed it.

And last but not least, thanks to my family who have always supported me, and what I am proud being part of.

Publications

The third chapter is partly based on works published in Phys. Rev. D **81**, 124001 (2010). The fourth chapter is based on works published in Phys. Rev. D **80**, 064027 (2009).

Conventions

Throughout this thesis, we follow the following conventions.

Greek indices denote four-dimensional space-time indices, as

$$x^\mu \in \{x^0, x^1, x^2, x^3\} = \{ct, x, y, z\},$$

and Latin indices denote three-dimensional space indices, as

$$x^i \in \{x^1, x^2, x^3\} = \{x, y, z\}.$$

Dots denote time derivatives, for example

$$\dot{A} = \frac{dA}{dt}.$$

We use metrics with mostly-plus signature, for example the Minkowski metric is

$$\eta_{\mu\nu} = \mathrm{diag}(-1, 1, 1, 1), \qquad \text{and} \qquad ds^2 = g_{\mu\nu} dx^\mu dx^\nu = -c^2 d\tau^2.$$

We use the convention that repeated upper and lower space-time indices imply summation, like

$$A^\mu B_\mu = \sum_{\mu=0}^{3} A^\mu B_\mu,$$

and that repeated space indices, whether upper or lower or mixed, also imply summation, like

$$A^i B^i = \sum_{i=1}^{3} A^i B^i, \qquad A^i B_i = \sum_{i=1}^{3} A^i B_i, \qquad A_i B_i = \sum_{i=1}^{3} A_i B_i.$$

Boldface symbols denote three-dimensional vectors; we denote the Euclidean scalar product by a centered dot, the three-dimensional vector product by a cross, like

$$\boldsymbol{A} \cdot \boldsymbol{B} = A^i B^i, \qquad (\boldsymbol{A} \times \boldsymbol{B})_i = \epsilon_{ijk} A^j B^k,$$

where ϵ_{ijk} is the three-dimensional totally antisymmetric Levi-Civita symbol with $\epsilon_{123} = 1$.

Three-dimensional unit vectors are denoted by a hat, and the norm of vectors are denoted by non-boldface symbols, as

$$A = |\boldsymbol{A}|, \qquad \hat{\boldsymbol{A}} = \frac{\boldsymbol{A}}{A}.$$

We use the Christoffel symbols

$$\Gamma^\mu_{\nu\rho} = \frac{1}{2} g^{\mu\alpha} \left(\partial_\nu g_{\alpha\rho} + \partial_\rho g_{\alpha\nu} - \partial_\alpha g_{\nu\rho} \right),$$

the Riemann tensor

$$R^\mu{}_{\nu\rho\sigma} = \partial_\rho \Gamma^\mu_{\nu\sigma} - \partial_\sigma \Gamma^\mu_{\nu\rho} + \Gamma^\alpha_{\nu\sigma} \Gamma^\mu_{\alpha\rho} - \Gamma^\alpha_{\nu\rho} \Gamma^\mu_{\alpha\sigma},$$

and the Ricci tensor

$$R_{\mu\nu} = R^{\alpha}{}_{\mu\alpha\nu}.$$

The Einstein equation is written as

$$R_{\mu\nu} = \frac{8\pi G}{c^4}\left(T_{\mu\nu} - \frac{1}{2}g_{\mu\nu}T^{\alpha}{}_{\alpha}\right).$$

We will use a definiton of the Fourier transform of a signal that is common in gravitational wave science, and we will denote Fourier transforms with a tilde, as

$$\tilde{h}(f) = \int h(t)e^{2\pi i f t}dt \qquad \Longleftrightarrow \qquad h(t) = \int \tilde{h}(f)e^{-2\pi i f t}df.$$

Contents

Chapter 1

Introduction

General Relativity describes gravitation as an effect of the curvature of space-time. The fact that distant objects are attracted to each other reflect the fact that massive objects deform the space-time surrounding them, so that objects passing in their neighbourhood are attracted to them. In this framework, if we imagine a system undergoing a periodic motion, such as a system of two stars orbiting each other, the space-time surrounding them is deformed in a periodic manner. Such a periodic deformation of space-time is called a gravitational wave, and is a prediction of General Relativity.

Gravitational waves represent a completely new window to observe our Universe, and their direct detection would be of great interest both theoretically and astrophysically. Gravitational waves have already been detected indirectly through the spin-down of binary pulsars and the observation thereof is in remarkable agreement with General Relativity. However, these kinds of systems as well as other tests of General Relativity are all in the weak-field regime, and therefore cannot probe effects that occur in the strong field regime, accessible near the surface of compact objects such as black holes, neutron stars or white dwarves. Gravitational waves, on the other hand, are emitted throughout the merging process of compact objects, and can therefore probe the strong-field structure of gravity, whether described by General Relativity or by another theory consistent with the former in the weak-field regime. On a different level, gravitational wave detection is sensitive to all compact systems, and does not require the observed system to be interacting electromagnetically. In particular, the detection of gravitational wave signals could be used to constrain the distribution of dark objects like black holes or neutron stars inside a galaxy with unprecedented confidence. The detection of gravitational waves could also be used to constrain galaxy formation scenarios by tracing the evolution history of supermassive black holes that we expect to be present at the center of almost all spiral galaxies, measuring their masses and spins to very high precision. Cosmic inflation, as we currently understand it, is expected to leave a background gravitational wave remnant in the Universe. The search for gravitational waves in this regime could help constrain inflation scenarios, and maybe even detect inflation directly.

In this thesis, we focus on supermassive binary black hole systems, and their detection prospects by the planned Laser Interferometer Space Antenna (LISA). We believe that

most galaxies in our Universe host a central supermassive black hole (of mass greater than 10^5 Solar masses), and therefore most galaxy merger events should be associated with a supermassive black hole merger event. LISA has been designed to be most sensitive to black holes in the mass range 10^5 to a few 10^7 solar masses.

The first attempt to estimate the accuracy at which an interferometer could measure the properties of a compact object binary was made in 1992 by Finn [1], who first introduced the Fisher matrix analysis, which is now widely used in this context. In 1998, Cutler [2] applied this formalism to LISA, focusing on the angular resolution that the space-based detector could achieve for black hole binaries, using the Newtonian quadrupole formula. In 2002 Hughes [3] repeated the study including the PN expansion for the wave frequency. Vecchio [4], in 2004, considered the case of the "simple precession" [5] of the angular momenta for spinning BH's. Lang and Hughes [6] then used in 2006 the full precession equations to further refine the parameter estimation. Then, Arun et al. [7] in 2007 and Porter and Cornish [8] in 2008 included the full post-Newtonian waveform in the context of nonspinning black holes, and the same year Trias and Sintes [9] used it for spinning black holes, albeit neglecting spin-precession effects. The LISA Parameter Estimation Taskforce [10] used the full waveform with spin-precession effects in 2009, without publishing a detailed study of the expected statistical errors. It is worth noting that, as more and more precise waveforms were used, all of the effects that these works studied helped to improve subsequently the expected measurement accuracy of LISA. In this thesis, we try to compare the measurement capabilities of waveforms including different effects, notably the inclusion of subdominant harmonics together with spin-induced precession for binaries on eccentric orbits, and the impact of the eccentricity on such a waveform.

1.1 Gravitational waves

In this section, we review the basics of gravitational wave theory, and introduce the tools needed for building post-Newtonian waveforms. It is mostly based on [11, 12, 13, 14], and we refer the interested reader to these books and reviews for further information.

1.1.1 Linearized metric perturbations

Gravitational waves are perturbations around a background metric that propagate through space-time and that carry energy and momentum. Far away from the source, at the level of the detector, let us consider a perturbation around a flat background described by

$$g_{\mu\nu} = \eta_{\mu\nu} + h_{\mu\nu}, \qquad |h_{\mu\nu}| \ll 1, \tag{1.1}$$

where $\eta_{\mu\nu}$ is the Minkowski metric, and let us work in linearized theory, discarding any term contributing at second order or higher in $h_{\mu\nu}$. We use the usual convention that indices are raised and lowered with the Minkowski metric, and we define the trace of the perturbation as $h = h^{\alpha}{}_{\alpha}$.

Let us introduce the trace-reversed perturbation

$$\bar{h}_{\mu\nu} = h_{\mu\nu} - \frac{1}{2}\eta_{\mu\nu}h. \tag{1.2}$$

We can always perform a coordinate change $x^\mu \to x^\mu + \xi^\mu$ with ξ^μ of the order of $h_{\mu\nu}$ to put the perturbation in the harmonic gauge, described by $\partial^\mu \bar{h}_{\mu\nu} = 0$. The linearized Einstein equations then become simply

$$\partial^\alpha \partial_\alpha \bar{h}_{\mu\nu} = -\frac{16\pi G}{c^4} T^{\mu\nu}, \tag{1.3}$$

where $T^{\mu\nu}$ is the energy-momentum tensor of matter. In a flat, empty background, it vanishes and thus the linearized Einstein equation becomes a wave equation. Let us for the rest of this subsection consider that these waves propagate in empty space.

To make the physical degrees of freedom appear explicitly, it is convenient to introduce the transverse-traceless (TT) gauge. Indeed, the harmonic gauge condition does not fix the gauge completely, and we are still free to perform a coordinate transformation $x^\mu \to x^\mu + \xi^\mu$ with $\partial^\alpha \partial_\alpha \xi^\mu = 0$ without destroying the harmonic gauge condition. We are thus left with the freedom to choose four supplementary gauge conditions. The TT gauge consists of choosing them so as to ensure $\bar{h} = 0$ and $\bar{h}_{0i} = 0$. The full TT gauge condition is then described by

$$h_{0\mu} = 0, \qquad h^i{}_i = 0, \qquad \partial^i h_{ij} = 0. \tag{1.4}$$

As the perturbation is traceless, we have $\bar{h}_{\mu\nu} = h_{\mu\nu}$.

Note that the TT gauge makes clear that outside the source, only two degrees of freedom can describe physical propagating waves. The wave equation can be written as

$$\left(\frac{1}{c^2}\frac{\partial^2}{\partial t^2} - \delta^{ij}\frac{\partial}{\partial x^i}\frac{\partial}{\partial x^j} \right) h_{\mu\nu} = 0. \tag{1.5}$$

This equation accepts plane-wave solutions travelling at the speed of light. Let us, for definiteness, examine one plane wave travelling in the z direction. In the TT gauge we have $h_{0\mu} = h_{z\mu} = 0$. We can write the solution as

$$h^{TT}_{ij}(t,z) = \begin{pmatrix} h_+ & h_\times \\ h_\times & -h_+ \end{pmatrix} \cos\left[\omega\left(t - \frac{z}{c}\right)\right], \tag{1.6}$$

where $i, j \in \{1, 2\}$.

The perturbed line element is then

$$\begin{aligned} ds^2 = &-c^2dt^2 + \left\{1 + h_+ \cos\left[\omega\left(t - \frac{z}{c}\right)\right]\right\} dx^2 + \left\{1 - h_+ \cos\left[\omega\left(t - \frac{z}{c}\right)\right]\right\} dy^2 \\ &+ 2h_\times \cos\left[\omega\left(t - \frac{z}{c}\right)\right] dxdy + dz^2. \end{aligned} \tag{1.7}$$

Let us finally note that the plane wave described by (1.6) can be put in the diagonal form by rotating the coordinate system by an angle $\alpha = \arctan(h_\times/h_+)/2$.

1.1.2 Interactions with interferometers

We present in this subsection how gravitational waves influence the measurements done with Michelson-type interferometers. The functioning principle of a Michelson interferometer is to split a coherent light signal into two separate beams, so that each of them travels on a different path, and to recombine them afterwards to obtain an interference light pattern. We sketch a minimalistic Michelson interferometer setup in Fig. 1.1.

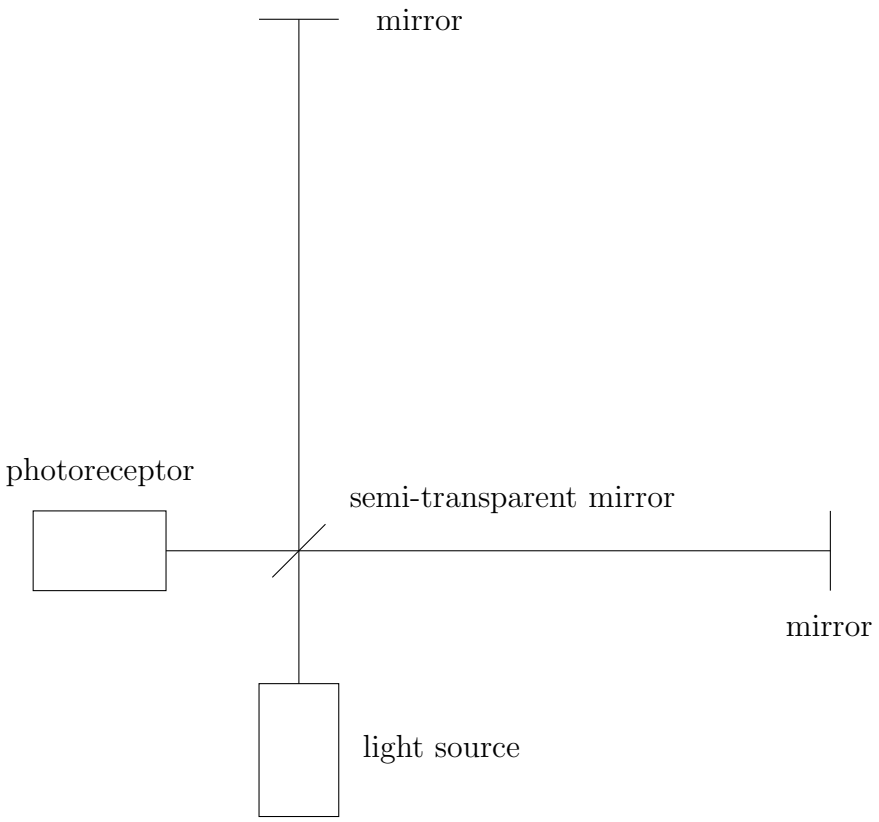

Figure 1.1: Functioning principle of a Michelson interferometer. A coherent light signal is emitted from a source, and split into two beams. Both beams are then reflected, recombined, and then measured in a photodetector. The fact that they travel along a different path induces an interference pattern in the recombined signal.

Interferometric gravitational wave detectors are built so that the lasers, the mirrors and the photoreceptors stay at rest. Let us thus look at the evolution of their coordinates in the TT gauge when a gravitational wave passes through. Masses at rest follow timelike geodesics, and their coordinates obey the geodesic equation

$$\frac{d^2x^\mu}{d\tau^2} + \Gamma^\mu_{\nu\rho}\frac{dx^\nu}{d\tau}\frac{dx^\rho}{d\tau} = 0. \tag{1.8}$$

The assumption that they are at rest at $\tau = 0$ implies that $dx^i/d\tau|_{\tau=0} = 0$, and we can write, at $\tau = 0$:

$$\frac{d^2x^\mu}{d\tau^2} + \Gamma^\mu_{00}\left(\frac{dx^0}{d\tau}\right)^2 = 0. \tag{1.9}$$

In the TT gauge, we have (with no summation on μ)

$$\Gamma^\mu_{00} = \eta^{\mu\mu}\left(\partial_0 h_{0\mu} - \frac{1}{2}\partial_\mu h_{00}\right) = 0. \tag{1.10}$$

Thus, in the TT gauge, a mass initially at rest stays at rest. This means that the coordinates are fixed by the position of test masses and that the distance between fixed points shrinks and stretches in response to the passage of a gravitational wave.

Let us now examine the situation of an equal-arm interferometer whose arms are located along the x and y axes, while a gravitational wave travelling in the z direction passes through. We fix the positions of the mirrors at $(L, 0, 0)$ and $(0, L, 0)$, and assume that the gravitational wave tensor is diagonal. The metric is given by

$$ds^2 = -c^2dt^2 + [1 + h_+(t, z)]\, dx^2 + [1 - h_+(t, z)]\, dy^2 + dz^2. \tag{1.11}$$

Light signals travel on null geodesics satisfying $ds^2 = 0$. Therefore, the position of a light beam travelling in the x direction satisfies

$$dx = \pm cdt\, [1 + h_+(t, 0)]^{-1/2} \approx \pm cdt\left[1 - \frac{1}{2}h_+(t)\right], \tag{1.12}$$

the sign depending on in which direction the beam is travelling.

Let us consider a light beam of angular frequency ω_l emitted at the origin at time t_0, travelling along the x arm, hitting the mirror at time t_1, and getting back to the origin at time t_2. Integrating the equation above, we get

$$L = c(t_1 - t_0) - \frac{1}{2}\int_{t_0}^{t_1} h_+(t)dt, \tag{1.13}$$

$$L = c(t_2 - t_1) - \frac{1}{2}\int_{t_1}^{t_2} h_+(t)dt. \tag{1.14}$$

Using (1.6), we find

$$\begin{aligned} c(t_2 - t_0) &= 2L + \frac{1}{2}\int_{t_0}^{t_0+2L/c} h_+(t)dt \\ &= 2L + \frac{h_+}{2\omega}[\sin\omega(t_0 + 2L/c) - \sin\omega t_0], \end{aligned} \tag{1.15}$$

where we replaced t_2 in the bounds of the integral with $t_0 + 2L/c$. This is consistent with staying at linear order, since the error introduced by this approximation is of order h^2.

Using the same reasoning for the beam travelling in the y direction, we find

$$c(t_{2,y} - t_0) = 2L - \frac{h_+}{2\omega}[\sin\omega(t_0 + 2L/c) - \sin\omega t_0]. \tag{1.16}$$

Thus, the two signals arrive back at the photoreceptor with a time difference of

$$\Delta t = \frac{h_+}{\omega}[\sin\omega(t_0 + 2L/c) - \sin\omega t_0]. \tag{1.17}$$

Now, we can compute the phase difference between two continuous signals observed in the photoreceptor at time t after they have travelled back and forth along the two arms of the interferometer. The times of emission are

$$t_{0,x} = t - 2L/c - \frac{h_+}{2\omega}[\sin\omega t - \sin\omega(t - 2L/c)], \tag{1.18}$$

$$t_{0,y} = t - 2L/c + \frac{h_+}{2\omega}[\sin\omega t - \sin\omega(t - 2L/c)], \tag{1.19}$$

and thus the phase difference is

$$\Delta\phi_l = \omega_l \Delta t = h_+ \frac{\omega_l}{\omega}[\sin\omega t - \sin\omega(t - 2L/c)], \tag{1.20}$$

allowing us to observe the effect of a gravitational wave in the interferomeric pattern of the detector.

It is standard practice in the literature to express the arrival time difference (1.17) in the long wavelength approximation $\lambda = c/\omega \gg L$ by a differential length change of the arms:

$$\frac{\Delta L(t)}{L} = \frac{1}{2L} c\Delta t(t) = h_+ \cos\omega t = h_+(t). \tag{1.21}$$

One can generalize this reasoning to a wave coming from an arbitrary direction, with arbitrary polarization, and a general opening angle between the arms of the interferometer (see [14]). The gravitational wave signal that one would observe, defined by $h(t) = \Delta L(t)/L$, takes the form

$$h(t) = F_+(\theta, \phi, \psi)h_+(t) + F_\times(\theta, \phi, \psi)h_\times(t), \tag{1.22}$$

where F_+ and $F_\times$ are the *antenna pattern functions*, θ and ϕ are the spherical angles of the position of the source in the sky, and ψ is an angle dependent on the polarization of the wave in a frame tied to the detector.

1.2 Generation of gravitational waves

After we have studied the interactions of gravitational waves with a detector, let us focus on the emission process of these waves by compact binary systems. The merging process of two compact objects is traditionally separated into three distinct phases: the

inspiral phase, where the two bodies are well separated; the merging phase, where the two bodies have come so close together that they can no longer be considered as distinct objects; and the ringdown phase, where the excess in multipole moments of the final object is gravitationally radiated away so that it becomes gradually static. In this thesis, we will focus on the inspiral phase, where the post-Newtonian (PN) formalism can be applied. The Newtonian theory of gravity, in which Kepler's third law applies, describes the leading order solution for the motion of self-gravitating systems. Therefore, at leading order $GM/d \sim v^2$, where M is the total mass of the system, d is the typical length scale associated with it, and v is its typical velocity. We can rewrite this as $r_s/d \sim (v/c)^2$, where $r_s = GM/c^2$ is the Schwartzschild radius associated with M. The PN expansion consists of an expansion in powers of $\epsilon \sim (r_s/d)^{1/2} \sim v/c$.

1.2.1 The post-Newtonian expansion

To use the PN formalism that we will describe below, we demand that the PN expansion parameter ϵ defined above is small, and that the energy-momentum tensor of the source $T^{\mu\nu}$ has spatially compact support, i.e. that it is zero outside some finite region of space at all times. We consider two distinct regions: the near zone, enclosing the source and smaller than the typical wavelength of the radiation emitted; and the far zone, sufficiently far away from the source so that the linear approximation used in the last section can be applied.

We denote the term of order n in ϵ in the quantity A by ${}^{(n)}A$. To write the expansion of the metric and of the energy-momentum tensor of the source, we note that, if we neglect the backreaction of the system to its energy loss, the system should be invariant under time reversal. Since the 00 and ij components of these objects are even under time reversal, they can only contain even powers of v and thus of ϵ. Similarly, their $0i$ components are odd under time reversal and can only contain odd powers of ϵ. To correctly compute the order of a quantity, we must further take into account that time derivatives are one order higher than spatial derivatives:

$$\frac{\partial}{\partial x^0} = \frac{1}{c}\frac{\partial}{\partial t} \sim \frac{1}{c}\frac{\partial x^i}{\partial t}\frac{\partial}{\partial x^i} \sim \frac{v}{c}\frac{\partial}{\partial x^i} \sim \epsilon\frac{\partial}{\partial x^i}. \tag{1.23}$$

In particular, the d'Alembertian is a Laplacian at leading order, and retardation effects are small corrections. Therefore, the expansion of a retarded quantity is computed as an expansion for small retardations

$$A(t - r/c) = A(t) - \frac{r}{c}\dot{A}(t) + \frac{1}{2}\frac{r^2}{c^2}\ddot{A}(t) + \dots. \tag{1.24}$$

Since each time derivative contains one power of the typical angular frequency of the system, this equation is actually an expansion in powers of r/λ, where λ is the typical wavelength associated with the gravitational radiation emitted by the system. Thus, the PN expansion is only applicable in the near zone, and we must resort to another formalism in the far zone.

Let us then expand the metric in the near zone in powers of ϵ around the Minkowski metric:

$$\begin{aligned} g_{00} &= -1 + {}^{(2)}g_{00} + {}^{(4)}g_{00} + \dots , \\ g_{0i} &= {}^{(3)}g_{0i} + \dots , \\ g_{ij} &= \delta_{ij} + {}^{(2)}g_{ij} + \dots . \end{aligned} \tag{1.25}$$

We ordered the terms in this way because terms on top of each other will appear at the same order in the equations of motion that we will later infer. The first order to contain ${}^{(2)}g_{00}$ is called the Newtonian order, the first to contain ${}^{(4)}g_{00}$ is called the first post-Newtonian (1PN) order, and so on for higher orders. We can preform a similar expansion of the energy-momentum tensor of the source as

$$\begin{aligned} T^{00} &= {}^{(0)}T^{00} + {}^{(2)}T^{00} + \dots , \\ T^{0i} &= {}^{(1)}T^{0i} + {}^{(3)}T^{0i} + \dots , \\ T^{ij} &= {}^{(2)}T^{ij} + {}^{(4)}T^{ij} + \dots , \end{aligned} \tag{1.26}$$

where we used the requirement that the source is weakly stressed, i.e. that $|T^{ij}| \sim \epsilon^2 |T^{00}|$.

We can also expand the inverse metric $g^{\mu\nu}$, and using the fact that $g^{\mu\rho} g_{\rho\nu} = \delta^\mu_\nu$ allows us to write the coefficients of the expansion of $g^{\mu\nu}$ in terms of the coefficients in (1.25).

We can now insert the PN expansions above into Einstein's equations, and solve them order by order to find the metric components. Subsequently, we can insert these results into the geodesic equation to find the equations of motion. Let us see how this works at the 1PN order.

First, let us investigate the geodesic equation. We will need the relationship between proper time and coordinate time at 1PN, which reads:

$$c^2 \left(\frac{d\tau}{dt}\right)^2 = -g_{\mu\nu} \frac{dx^\mu}{dt} \frac{dx^\nu}{dt} \tag{1.27}$$

$$\Longrightarrow \qquad \frac{dt}{d\tau} = 1 + \frac{1}{2}\frac{\boldsymbol{v}^2}{c^2} + \frac{1}{2}\, {}^{(2)}g_{00} \, . \tag{1.28}$$

The Newtonian equations of motion are given by the leading-order spatial components of the geodesic equation:

$$a^i + {}^{(2)}\Gamma^i_{00}\, c^2 = 0, \tag{1.29}$$

where $a^i = d^2x^i/dt^2$ is the acceleration of the body. The first post-Newtonian corrections are given by

$$\frac{d}{dt}\left(\frac{dt}{d\tau}\right) + {}^{(3)}\Gamma^0_{00}\, c + 2\, {}^{(2)}\Gamma^0_{i0}\, v^i = 0, \tag{1.30}$$

$$\frac{d}{dt}\left(\frac{dt}{d\tau} v^i\right) + \frac{dt}{d\tau}\, {}^{(2)}\Gamma^i_{00}\, c^2 + {}^{(4)}\Gamma^i_{00}\, c^2 + 2\, {}^{(3)}\Gamma^i_{j0}\, v^j c + {}^{(2)}\Gamma^i_{jk}\, v^j v^k = 0. \tag{1.31}$$

This tells us at which PN order we need each Christoffel symbol, and by examining their expressions, this justifies the ordering of the metric expansion terms we used in (1.25).

Let us now define the Newtonian potential ϕ by

$$ {}^{(2)}g_{00} = -2\phi. \tag{1.32} $$

At Newtonian order, the 00-component of Einstein's equations then reads

$$ \nabla^2\phi = \frac{4\pi G}{c^4}\, {}^{(0)}T^{00}\,, \tag{1.33} $$

whose solution with the boundary condition that it vanishes at infinity is

$$ \phi(t,\boldsymbol{x}) = -\frac{G}{c^4}\int \frac{d^3x'}{|\boldsymbol{x}-\boldsymbol{x}'|}\, {}^{(0)}T^{00}(t,\boldsymbol{x}')\,. \tag{1.34} $$

To write Einstein's equations at 1PN order, it proves useful to work in the harmonic gauge, defined by the condition $\partial_\mu\left(\sqrt{-g}\,g^{\mu\nu}\right)=0$.

At 1PN order, the ij-component of Einstein's equations reads

$$ \nabla^2\left[{}^{(2)}g_{ij}\right] = -\frac{8\pi G}{c^4}\, {}^{(0)}T^{00}\,\delta_{ij}, \tag{1.35} $$

which is solved by

$$ {}^{(2)}g_{ij} = -2\phi\delta_{ij}. \tag{1.36} $$

If we define the potential $\boldsymbol{\zeta}$ by

$$ {}^{(3)}g_{0i} = \zeta^i, \tag{1.37} $$

the 1PN $0i$-components of Einstein's equations read

$$ \nabla^2\zeta^i = \frac{16\pi G}{c^4}\, {}^{(1)}T^{0i}\,, \tag{1.38} $$

whose solution with the boundary condition that it vanishes at infinity is

$$ \zeta^i(t,\boldsymbol{x}) = -\frac{4G}{c^4}\int \frac{d^3x'}{|\boldsymbol{x}-\boldsymbol{x}'|}\, {}^{(1)}T^{0i}(t,\boldsymbol{x}')\,. \tag{1.39} $$

Finally, if we define the potential ψ by

$$ {}^{(4)}g_{00} = -2\left(\phi^2+\psi\right), \tag{1.40} $$

the 1PN 00-component of Einstein's equations reads

$$ \nabla^2\psi = \partial_0^2\phi + \frac{4\pi G}{c^4}\left[{}^{(2)}T^{00} + {}^{(2)}T^{ii}\right]. \tag{1.41} $$

We can first note that if we define another potential χ by

$$ \chi(t,\boldsymbol{x}) = -\frac{G}{2c^4}\int d^3x'|\boldsymbol{x}-\boldsymbol{x}'|\, {}^{(0)}T^{00}(t,\boldsymbol{x}')\,, \tag{1.42} $$

it satisfies

$$ \nabla^2\chi = \phi. \tag{1.43} $$

We can thus write the solution of Eq. (1.41) as

$$ \psi(t,\boldsymbol{x}) = \partial_0^2\chi(t,\boldsymbol{x}) - \int \frac{d^3x'}{|\boldsymbol{x}-\boldsymbol{x}'|}\left\{\frac{G}{c^4}\left[{}^{(2)}T^{00}(t,\boldsymbol{x}') + {}^{(2)}T^{ii}(t,\boldsymbol{x}')\right]\right\}. \tag{1.44} $$

This gives the metric in the near zone at 1PN order.

1.2.2 Application to binary systems

Let us now apply this formalism to the problem of binary systems, to deduce an action for black hole binaries. At 1PN order, we can consider the masses as point-like, which yields the following energy-momentum tensor:

$$T^{\mu\nu}(t,\boldsymbol{x}') = \sum_a \frac{1}{\sqrt{-g}} m_a \frac{dx_a^\mu}{dt}\frac{dx_a^\nu}{dt}\frac{dt}{d\tau_a}\delta(\boldsymbol{x}_a - \boldsymbol{x}'), \tag{1.45}$$

where the sum is performed on both bodies indexed by a, and τ_a is the proper time of body a.

Thus, using (1.28), (1.32), (1.36), (1.37), and (1.40), the lowest PN terms in the expansion of the energy-momentum tensor are

$$^{(0)}T^{00}(t,\boldsymbol{x}') = \sum_a m_a c^2 \delta[\boldsymbol{x}_a(t) - \boldsymbol{x}'], \tag{1.46}$$

$$^{(2)}T^{00}(t,\boldsymbol{x}') = \sum_a m_a \left\{\frac{1}{2}\boldsymbol{v}_a^2(t) + \phi[t,\boldsymbol{x}_a(t)]c^2\right\}\delta[\boldsymbol{x}_a(t) - \boldsymbol{x}'], \tag{1.47}$$

$$^{(1)}T^{0i}(t,\boldsymbol{x}') = \sum_a m_a c v_a^i(t) \delta[\boldsymbol{x}_a(t) - \boldsymbol{x}'], \tag{1.48}$$

$$^{(2)}T^{ij}(t,\boldsymbol{x}') = \sum_a m_a v_a^i(t) v_a^j(t) \delta[\boldsymbol{x}_a(t) - \boldsymbol{x}']. \tag{1.49}$$

Using (1.34), we find for the Newtonian potential

$$\phi(t,\boldsymbol{x}) = -\sum_a \frac{Gm_a}{|\boldsymbol{x} - \boldsymbol{x}_a(t)|\, c^2}. \tag{1.50}$$

Now, if we plug the expressions for the Christoffel symbols into the equations of motion (1.29), we get

$$a^i + c^2\partial_i\phi = 0. \tag{1.51}$$

As one would expect, the equations of motion are those of Newtonian gravity:

$$\boldsymbol{a}_a = \frac{Gm_b(\boldsymbol{x}_b - \boldsymbol{x}_a)}{|\boldsymbol{x}_b - \boldsymbol{x}_a|^3}, \tag{1.52}$$

where $b \neq a$.

We then find that the 0-component of the geodesic equation at 1PN order (1.30) reads

$$v^i\left(a^i + c^2\partial_i\phi\right) = 0. \tag{1.53}$$

As this equation is a 1PN equation, we can use the Newtonian equation of motion to show that it is satisfied. The error made by using such an approximate relation comes one post-Newtonian order higher, at 2PN.

The i-component (1.31) reads

$$a^i + c^2\partial_i\phi + \left(\frac{\boldsymbol{a}\cdot\boldsymbol{v}}{c^2}\right)v^i + \frac{\boldsymbol{v}^2}{2c^2}a^i - \phi a^i - 3v^i\partial_t\phi + \frac{3}{2}\boldsymbol{v}^2\partial_i\phi + 3c^2\phi\partial_i\phi \\ - 3v^iv^j\partial_j\phi + cv^j\partial_j\zeta^i - cv^j\partial_i\zeta^j + c\partial_t\zeta^i + c^2\partial_i\psi = 0. \quad (1.54)$$

We can now compute the potentials by putting the expressions for the energy-momentum tensor into the integrals (1.39), (1.42) and (1.44). We find

$$\boldsymbol{\zeta}(t,\boldsymbol{x}) = -\sum_a \frac{4Gm_a\boldsymbol{v}_a(t)}{|\boldsymbol{x}-\boldsymbol{x}_a(t)|\,c^3}, \quad (1.55)$$

$$\chi(t,\boldsymbol{x}) = -\sum_a \frac{Gm_a\,|\boldsymbol{x}-\boldsymbol{x}_a(t)|}{2c^2}, \quad (1.56)$$

and

$$\psi(t,\boldsymbol{x}) = \partial_0^2\chi(t,\boldsymbol{x}) - \int\frac{d^3x'}{|\boldsymbol{x}-\boldsymbol{x}'|}\left\{\frac{G}{c^4}\left[{}^{(2)}T_2^{00}(t,\boldsymbol{x}') + {}^{(2)}T_2^{ii}(t,\boldsymbol{x}')\right]\right\} \\ = \sum_a \frac{Gm_a}{|\boldsymbol{x}-\boldsymbol{x}_a(t)|\,c^4}\left\{\frac{1}{2}\frac{\{\boldsymbol{v}_a(t)\cdot[\boldsymbol{x}-\boldsymbol{x}_a(t)]\}^2}{|\boldsymbol{x}-\boldsymbol{x}_a(t)|^2} \right. \\ \left. - 2\boldsymbol{v}_a^2(t) + \frac{Gm_b}{r(t)} + \frac{1}{2}\boldsymbol{a}_a(t)\cdot[\boldsymbol{x}-\boldsymbol{x}_a(t)]\right\}. \quad (1.57)$$

We can now use the expressions for these potentials in the equations of motion to get for mass a

$$\boldsymbol{a}_a - \frac{Gm_b}{r^2}\hat{\boldsymbol{r}} + \left(\frac{\boldsymbol{a}_a\cdot\boldsymbol{v}_a}{c^2}\right)\boldsymbol{v}_a + \frac{\boldsymbol{v}_a^2}{2c^2}\boldsymbol{a}_a + \frac{Gm_b}{rc^2}\left[\boldsymbol{a}_a - \frac{7}{2}\boldsymbol{a}_b - \frac{1}{2}(\boldsymbol{a}_b\cdot\hat{\boldsymbol{r}})\,\hat{\boldsymbol{r}}\right. \\ + 3\frac{\boldsymbol{v}_a\cdot\hat{\boldsymbol{r}}}{r}\boldsymbol{v}_a - 3\frac{\boldsymbol{v}_b\cdot\hat{\boldsymbol{r}}}{r}\boldsymbol{v}_a - 4\frac{\boldsymbol{v}_a\cdot\hat{\boldsymbol{r}}}{r}\boldsymbol{v}_b + 3\frac{\boldsymbol{v}_b\cdot\hat{\boldsymbol{r}}}{r}\boldsymbol{v}_b \\ \left. - \frac{3}{2}\frac{\boldsymbol{v}_a^2}{r}\hat{\boldsymbol{r}} + 4\frac{\boldsymbol{v}_a\cdot\boldsymbol{v}_b}{r}\hat{\boldsymbol{r}} - 2\frac{\boldsymbol{v}_b^2}{r}\hat{\boldsymbol{r}} + \frac{3}{2}\frac{(\boldsymbol{v}_b\cdot\hat{\boldsymbol{r}})^2}{r}\hat{\boldsymbol{r}} + \frac{G(m_a+3m_b)}{r^2}\hat{\boldsymbol{r}}\right] = 0, \quad (1.58)$$

where $\boldsymbol{r} = \boldsymbol{x}_b - \boldsymbol{x}_a$.

We now want to write one Lagrangian for both bodies that would lead to these equations of motion. To this purpose, we need to symmetrize the last term in the equations of motion. This can be done using the Newtonian equations of motion, similar to what we did with Eq. (1.53). The equation

$$\boldsymbol{a}_a + \frac{G(m_a+3m_b)}{r^2}\hat{\boldsymbol{r}} = 3\boldsymbol{a}_a + \frac{G(m_a+m_b)}{r^2}\hat{\boldsymbol{r}} \quad (1.59)$$

is correct at Newtonian order. Once symmetrized, if we want to write a Lagrangian that does not depend on second time derivatives, each term in the equations of motion containing

an acceleration must come from a term containing a velocity, and each term containing no time derivative must come from a term independent of velocities. From the structure of the equations of motion, we guess

$$L = \frac{1}{2}m_1\boldsymbol{v}_1^2 + \frac{1}{2}m_2\boldsymbol{v}_2^2 + \frac{Gm_1m_2}{r} + \frac{1}{8}m_1\frac{\boldsymbol{v}_1^4}{c^2} + \frac{1}{8}m_2\frac{\boldsymbol{v}_2^4}{c^2} + \frac{Gm_1m_2}{2rc^2}\left[3\left(\boldsymbol{v}_1^2+\boldsymbol{v}_2^2\right) - 7\boldsymbol{v}_1\cdot\boldsymbol{v}_2 - (\boldsymbol{v}_1\cdot\hat{\boldsymbol{r}})\,(\boldsymbol{v}_2\cdot\hat{\boldsymbol{r}}) - \frac{G(m_1+m_2)}{r}\right]. \tag{1.60}$$

We can verify that the equations of motion that we get from this Lagrangian are indeed those that we computed.

Similarly to the Newtonian problem, we get an effective one-body problem by transforming to the center-of-mass frame where $m_1\boldsymbol{x}_1 + m_2\boldsymbol{x}_2 = 0$, defining the total mass $M = m_1 + m_2$, the reduced mass $\mu = m_1m_2/M$, the symmetric mass ratio $\nu = \mu/M$, the separation $\boldsymbol{r} = \boldsymbol{x}_2 - \boldsymbol{x}_1$, and the velocity $\boldsymbol{v} = \boldsymbol{v}_2 - \boldsymbol{v}_1$. We get

$$\frac{L}{\mu} = \frac{1}{2}\boldsymbol{v}^2 + \frac{GM}{r} + \frac{1}{8}(1-3\nu)\frac{\boldsymbol{v}^4}{c^2} + \frac{GM}{2rc^2}\left[(3+\nu)\boldsymbol{v}^2 + \nu\,(\boldsymbol{v}\cdot\hat{\boldsymbol{r}})^2 - \frac{GM}{r}\right]. \tag{1.61}$$

Normally, we should use the 1PN center of mass frame to express the effective Lagrangian, defined through the application of Noether's theorem to the two-body Lagrangian with respect to Poincaré transformations. However, as showed in [15], it is sufficient to use the Newtonian center of mass, which we used here.

We can rewrite the equations of motion (1.58) as a correction to the Newtonian acceleration, by replacing each acceleration in the 1PN terms by its Newtonian value. We get

$$\boldsymbol{a}_{a,\mathrm{1PN}} = \frac{Gm_b}{r^2}\hat{\boldsymbol{r}} + \frac{Gm_b}{r^2c^2}\left\{[(4\boldsymbol{v}_a - 3\boldsymbol{v}_b)\cdot\hat{\boldsymbol{r}}](\boldsymbol{v}_b - \boldsymbol{v}_a) + \left[\boldsymbol{v}_a^2 - 4\boldsymbol{v}_a\cdot\boldsymbol{v}_b + 2\boldsymbol{v}_b^2 - \frac{3}{2}(\boldsymbol{v}_b\cdot\hat{\boldsymbol{r}})^2 - \frac{G(5m_a+4m_b)}{r}\right]\hat{\boldsymbol{r}}\right\}. \tag{1.62}$$

One could in principle extend this reasoning to find the equations of motion at higher orders. However, as we extend this framework to higher post-Newtonian orders, several problems appear. Firstly, as more nonlinearities are present in the field equations, integrals such as (1.34) diverge. The problem is that we cannot use the boundary condition that the field vanishes at infinity, but must be careful when choosing them. Secondly, the backreaction to GW emission is a 2.5PN order effect. We therefore must take this into account when it becomes necessary to do so. To tackle the problem of higher post-Newtonian corrections, as well as contructing waveforms for binary systems, we refer the interested reader to [16].

Chapter 2

Detecting gravitational waves with LISA

In this chapter, we introduce the main data analysis techniques needed for gravitational wave detection and parameter estimation using interferometers, and apply this to the properties of the LISA constellation.

2.1 Data analysis

In practice, detecting gravitational waves proves to be a rather complicated task, due to the weakness of the expected signal. The strongest astrophysical sources are expected to produce a signal at the location of the Solar System of the order $h \sim 10^{-18}$ or lower. Therefore, the signal we will be looking for will be buried deeply inside the measurement noise, and one must rely on potent data analysis techniques to extract it. In this section, we introduce the basis of matched filtering, a powerful data analysis tool that we can use in the context of gravitational wave experiments. We then introduce Fisher matrix formalism as a tool to perform parameter estimation. This section is primarily based on [1, 17, 18], and we refer the interested reader to these articles for further information.

2.1.1 Matched filtering

Matched filtering is an efficient data analysis technique that one can use to extract a signal from noise if one knows the structure of the signal one is looking for. This technique requires building a set of templates to perform the search, and we will see in the next chapter how such templates are built.

The signal coming from the detector $s(t)$ consists of a superposition of the gravitational wave signal $h(t)$ with some random noise $n(t)$, like

$$s(t) = h(t) + n(t). \tag{2.1}$$

To characterize the noise of the instrument, let us define the noise autocorrelation function as

$$\kappa(t_1, t_2) = \langle n(t_1) n(t_2) \rangle \,, \tag{2.2}$$

where $\langle \cdot \rangle$ denotes the average over an ensemble of noise realizations. We implicitly assume here that the noise has zero average. This is appropriate when characterizing an interferometry experiment.

When the performance of the detector is (in the statistical sense) time independent, the autocorrelation function depends only on $|T| = |t_2 - t_1|$. This property of the noise, called *stationarity*, is of course an approximation, but is valid if the time scale of the evolution of the detector performance is greater than the typical observation time scale. We assume in the following that the instrument noise is stationary. In this case, the one-sided power spectral density is defined as the Fourier transform of the autocorrelation function:

$$S_n(f) = \begin{cases} 2 \displaystyle\int_{-\infty}^{\infty} \kappa(T) e^{2\pi i f T} dT, & f \geq 0 \\ \\ 0, & f < 0 \end{cases} , \tag{2.3}$$

where we included a factor 2 by convention. This function satisfies

$$\langle \tilde{n}(f) \tilde{n}^*(f') \rangle = \frac{1}{2} \delta(f - f') S_n(f), \tag{2.4a}$$

$$\langle \tilde{n}(f) \tilde{n}(f') \rangle = \frac{1}{2} \delta(f + f') S_n(f), \tag{2.4b}$$

$$\langle \tilde{n}^*(f) \tilde{n}^*(f') \rangle = \frac{1}{2} \delta(f + f') S_n^*(f), \tag{2.4c}$$

where A^* denotes the complex conjugate of A.

Matched filtering consists of correlating the signal with a given template, in such a way so as to maximize some signal-to-noise ratio (SNR). Let us define the correlation of the signal with a real filter $q(t)$ by

$$c(\tau) = \int_{-\infty}^{\infty} s(t) q(t + \tau) dt. \tag{2.5}$$

Going to the Fourier domain, we can rewrite this expression as

$$c(\tau) = \int_{-\infty}^{\infty} \tilde{s}(f) \tilde{q}^*(f) e^{2\pi i f \tau} df. \tag{2.6}$$

Since the noise n is generated by a random process, so is the signal s, and hence the correlation c as well. Our purpose now is to find the optimal filter $q(t)$ that on average maximizes the SNR. What we wish to do is to use a filter whose correlation with the signal (2.5) is maximal, with minimal variance. In practice, the quantity we wish to maximize is the mean correlation divided by its standard deviation, or equivalently, $\langle c \rangle^2 / \langle (c - \langle c \rangle)^2 \rangle$.

Since the noise has zero average, the average correlation $S = \langle c \rangle$ is

$$\langle c(\tau) \rangle = \int_{-\infty}^{\infty} \tilde{h}(f) \tilde{q}^*(f) e^{2\pi i f \tau} df, \tag{2.7}$$

and the variance $N^2 = \langle (c - \langle c \rangle)^2 \rangle$ is given by

$$\left\langle [c(\tau) - \langle c(\tau) \rangle]^2 \right\rangle = \frac{1}{2} \int_{-\infty}^{\infty} S_n(f) |\tilde{q}(f)|^2 df. \tag{2.8}$$

If we now define a scalar product in the space of signals by

$$(a|b) = 2 \int_0^{\infty} \frac{\tilde{a}(f)\tilde{b}^*(f) + \tilde{a}^*(f)\tilde{b}(f)}{S_n(f)} df, \tag{2.9}$$

we see that the SNR $\rho = S/N$ satisfies

$$\rho = \frac{\left(h e^{2\pi i f \tau} \middle| S_n q\right)}{\sqrt{(S_n q | S_n q)}}. \tag{2.10}$$

Therefore, the template that maximizes the SNR is a multiple of the optimal filter

$$\tilde{q}_{\text{opt}}(f) = \frac{\tilde{h}(f)}{S_n(f)} e^{2\pi i f \tau}, \tag{2.11}$$

and we find for the optimal SNR

$$\rho = (h|h)^{1/2} = 2 \left(\int_0^{\infty} \frac{|\tilde{h}(f)|^2}{S_n(f)} df \right)^{1/2}. \tag{2.12}$$

2.1.2 Parameter estimation

Let us now see how we can estimate the capabilities of a set of N detectors, i.e. how precise measurements can be done with these instruments. If we assume that the noise is generated by a Gaussian process, the probability that a given noise realization is occuring in detector a is proportional to

$$p\left(n^{(a)} = n_0^{(a)}\right) \propto \exp\left[-\frac{1}{2} \left(n_0^{(a)} \middle| n_0^{(a)} \right)_{(a)} \right], \tag{2.13}$$

where $(\cdot|\cdot)_{(a)}$ denotes the scalar product (2.9) with the noise spectral density for detector a.

With this assumption, we can introduce a measure of the expected measurement accuracy in the instrument. Consider that we observe some signal consisting of a gravitational wave signal and a Gaussian stationary random noise in each detector, as in (2.1). Let us consider that the gravitational wave signal is a waveform which depends smoothly on some

finite set of parameters described by $\boldsymbol{\theta}$, and that the true gravitational wave present in the detector signal is described by some vector in the parameter space $\tilde{\boldsymbol{\theta}}$. We now wish to estimate the error on θ^i that we would make by inferring some best-fit parameter vector $\bar{\boldsymbol{\theta}}$.

The probability that the source parameters are described by $\boldsymbol{\theta}$ given the observed signal s is the same as the probability for the noise to take the particular realization that it would imply in each detector, i.e.

$$p\left(\boldsymbol{\theta}|\left\{s^{(a)}\right\}\right) \propto \prod_a \exp\left[-\frac{1}{2}\Big(s^{(a)}-h(\boldsymbol{\theta})\Big|s^{(a)}-h(\boldsymbol{\theta})\Big)_{(a)}\right], \tag{2.14}$$

where we assumed a flat prior on the parameters. The best-fit parameter vector $\bar{\boldsymbol{\theta}}$ is then the one that maximizes this likelihood, or equivalently, that minimizes the sum of the scalar products inside the exponentials.

We now want to estimate the probability distribution of $\Delta\boldsymbol{\theta} = \tilde{\boldsymbol{\theta}} - \bar{\boldsymbol{\theta}}$, the difference between the true and the maximum likelihood parameters, given the maximum likelihood parameters that we can infer from our likelihood distribution. As $\bar{\boldsymbol{\theta}}$ is a maximum of the likelihood function, we can write

$$\sum_a \Big(s^{(a)}-h(\bar{\boldsymbol{\theta}})\Big|h_{,i}(\bar{\boldsymbol{\theta}})\Big)_{(a)} = 0, \tag{2.15}$$

where $h_{,i} = \partial h/\partial\theta^i$. Therefore, if we write the observed signal as the true gravitational wave plus the instrumental noise, we get

$$\sum_a (h(\tilde{\boldsymbol{\theta}})-h(\bar{\boldsymbol{\theta}})|h_{,i}(\bar{\boldsymbol{\theta}}))_{(a)} = -\sum_a \Big(n^{(a)}\Big|h_{,i}(\bar{\boldsymbol{\theta}})\Big)_{(a)}. \tag{2.16}$$

Since $n^{(a)}$ are Gaussian random variables with zero mean, so are $\nu_i^{(a)} = (n^{(a)}|h_{,i}(\bar{\boldsymbol{\theta}}))_{(a)}$. Furthermore, we can use (2.4) to calculate their variance:

$$\begin{aligned}
\left\langle \nu_i^{(a)}\nu_j^{(b)}\right\rangle &= \left\langle \Big(n^{(a)}\Big|h_{,i}(\bar{\boldsymbol{\theta}})\Big)_{(a)}\Big(n^{(b)}\Big|h_{,j}(\bar{\boldsymbol{\theta}})\Big)_{(b)}\right\rangle \\
&= 4\int_0^\infty\int_0^\infty \frac{df\,df'}{S_n^{(a)}(f)S_n^{(b)}(f')}\Big\langle \Big[\tilde{n}_{(a)}(f)\tilde{h}^*_{,i}(f)+\tilde{n}^*_{(a)}(f)\tilde{h}_{,i}(f)\Big] \\
&\qquad\qquad \times\Big[\tilde{n}_{(b)}(f')\tilde{h}^*_{,j}(f')+\tilde{n}^*_{(b)}(f')\tilde{h}_{,j}(f')\Big]\Big\rangle \\
&= \delta_{ab}(h_{,i}(\bar{\boldsymbol{\theta}})|h_{,j}(\bar{\boldsymbol{\theta}}))_{(a)} \\
&= \delta_{ab}\Gamma^{(a)}_{ij}(\bar{\boldsymbol{\theta}}),
\end{aligned} \tag{2.17}$$

where $\Gamma^{(a)}$ is called the Fisher matrix.

Now, if the SNR (2.12) for the maximum likelihood parameters is large, we can expand the difference $h(\tilde{\boldsymbol{\theta}}) - h(\bar{\boldsymbol{\theta}})$ at linear order in $\Delta\boldsymbol{\theta}$. We therefore get

$$\sum_a (h(\tilde{\boldsymbol{\theta}})-h(\bar{\boldsymbol{\theta}})|h_{,i}(\bar{\boldsymbol{\theta}}))_{(a)} = \sum_a (h_{,j}(\bar{\boldsymbol{\theta}})|h_{,i}(\bar{\boldsymbol{\theta}}))_{(a)}\Delta\theta^j = \sum_a \Gamma^{(a)}_{ij}\Delta\theta^j = -\sum_a \nu_i^{(a)}. \tag{2.18}$$

Thus, if we define

$$\Gamma = \sum_a \Gamma^{(a)}, \tag{2.19}$$

$$\nu_i = \sum_a \nu_i^{(a)}, \tag{2.20}$$

$$\Sigma = \Gamma^{-1}, \tag{2.21}$$

the $\Delta\theta^i$ are related to the ν_i by a linear transformation:

$$\Delta\theta^i = -\Sigma^{ij}\nu_j. \tag{2.22}$$

The variance of ν_i is

$$\langle \nu_i \nu_j \rangle = \sum_a \sum_b \left\langle \nu_i^{(a)} \nu_j^{(b)} \right\rangle = \sum_a \Gamma_{ij}^{(a)} = \Gamma_{ij}. \tag{2.23}$$

The $\Delta\theta_i$ are thus Gaussian random variables with zero mean, and with variance

$$\left\langle \Delta\theta^i \Delta\theta^j \right\rangle = \Sigma^{ij}. \tag{2.24}$$

Therefore, the matrix Σ is called the covariance matrix.

The fact that in the limit of high SNR, the $\Delta\theta^i$ have zero mean means that the maximum likelihood estimator $\bar{\boldsymbol{\theta}}$ is unbiased. Furthermore, the standard deviation of the measurement error on a given parameter is given by

$$\sigma\left(\Delta\theta^i\right) = \sqrt{\Sigma^{ii}}, \tag{2.25}$$

and the correlation factor between two given parameters is given by

$$c\left(\Delta\theta^i, \Delta\theta^j\right) = \frac{\Sigma^{ij}}{\sqrt{\Sigma^{ii}\Sigma^{jj}}}. \tag{2.26}$$

2.2 The LISA mission

The LISA constellation will consist of three spacecrafts launched in orbit around the Sun, at a mean distance of 1 AU, on slightly eccentric orbits so that the spacecrafts stay at the same distance from each other over the year, approximately of 17 light-seconds. The barycenter of LISA will be located on the orbit of the Earth, 20° behind it, and the normal to the plane on which the spacecrafts lie will make a 60° angle with the normal to the ecliptic, see Fig. 2.1.

Each spacecraft will contain a drag-free test mass, and a set of lasers and photoreceptors so as to monitor the distance from each spacecraft to the test mass inside it, as well as the distance between each spacecraft.

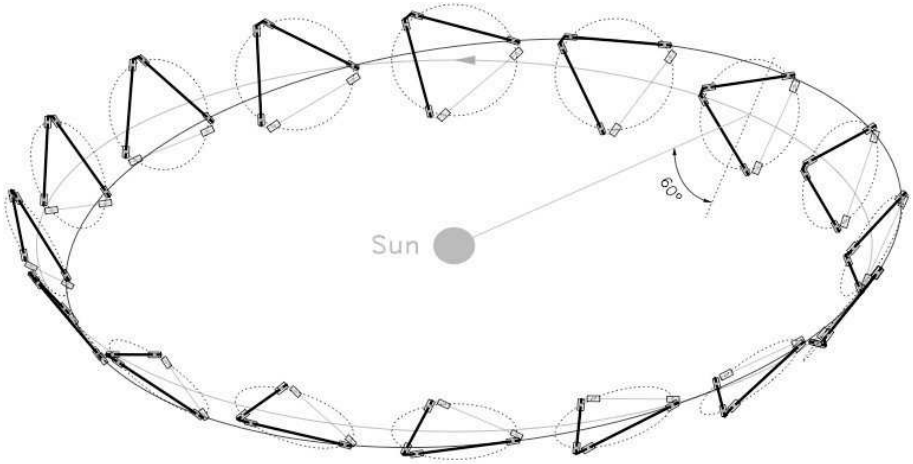

Figure 2.1: The orbit of LISA around the Sun as currently planned. Image taken from the LISA pre-phase-A report [19].

Using time-delay interferometry, we can show that we can build a pair of two-arm detectors with linear combinations of the different distance measurements, but with a response scaled by a $\sqrt{3}/2$ factor due to the 60° opening angle of the constellation, following the pattern ($k = 1, 2$):

$$h_k = \frac{\sqrt{3}}{2}\left(F_k^+ h_+ + F_k^\times h_\times\right), \tag{2.27}$$

$$F_1^+(\theta_N, \phi_N, \psi_N) = \frac{1}{2}\left(1 + \cos^2\theta_N\right)\cos 2\phi_N \cos 2\psi_N - \cos\theta_N \sin 2\phi_N \sin 2\psi_N, \tag{2.28}$$

$$F_1^\times(\theta_N, \phi_N, \psi_N) = F_1^+(\theta_N, \phi_N, \psi_N - \pi/4), \tag{2.29}$$

$$F_2^+(\theta_N, \phi_N, \psi_N) = F_1^+(\theta_N, \phi_N - \pi/4, \psi_N), \tag{2.30}$$

$$F_2^\times(\theta_N, \phi_N, \psi_N) = F_1^+(\theta_N, \phi_N - \pi/4, \psi_N - \pi/4), \tag{2.31}$$

where θ_N and ϕ_N are the spherical angles of the position of the binary in the detector frame, and ψ_N is defined through

$$\tan\psi_N \equiv \frac{\hat{\boldsymbol{L}} \cdot \hat{\boldsymbol{z}} - (\hat{\boldsymbol{L}} \cdot \hat{\boldsymbol{N}})(\hat{\boldsymbol{z}} \cdot \hat{\boldsymbol{N}})}{\hat{\boldsymbol{N}} \cdot (\hat{\boldsymbol{L}} \times \hat{\boldsymbol{z}})}, \tag{2.32}$$

where $\hat{\boldsymbol{L}}$ is the Newtonian orbital angular momentum of the source, $\hat{\boldsymbol{z}}$ is the normal to the detector plane, and $\hat{\boldsymbol{N}}$ is the unit vector in the direction of the source.

The two combinations of the response of the three arms of LISA have uncorrelated detector noise [2], so that we can use the Fisher matrix formalism that we introduced in the last section for parameter estimation.

The noise present in the LISA data will consist of two separate types: instrumental noise, which is noise due to the intrinsic properties of the interferometers; and confusion

noise, which arises from the confusion due to unresolvable binaries, whose signal will be present in the LISA data, but too close to each other in frequency for us to extract them. The instrumental noise can be separated into two parts: acceleration noise, dominant at low frequencies, coming e.g. from acceleration of the test masses due to the passage of a nearby object; and position noise, dominant at high frequencies, coming e.g. from the laser shot noise. In this thesis, we adopt the noise model used in [10], and consider the LISA band as the interval between 3×10^{-5} Hz and 1 Hz.

The instrumental noise one-sided power spectral density is given in Hertz by (f is also given in Hertz)

$$S_n^i(f) = \frac{1}{L^2}\left\{ \left[1 + \frac{1}{2}\left(\frac{f}{f_*}\right)^2\right] S_p + \left[1 + \left(\frac{10^{-4}}{f}\right)^2\right] \frac{4S_a}{(2\pi f)^4}\right\}, \tag{2.33a}$$

and the confusion noise is given by

$$S_n^c(f) = \begin{cases} 10^{-44.62} f^{-2.3} & (f \leqslant 10^{-3}), \\ 10^{-50.92} f^{-4.4} & (10^{-3} < f \leqslant 10^{-2.7}), \\ 10^{-62.8} f^{-8.8} & (10^{-2.7} < f \leqslant 10^{-2.4}), \\ 10^{-89.68} f^{-20} & (10^{-2.4} < f \leqslant 10^{-2}), \\ 0 & (10^{-2} < f). \end{cases}, \tag{2.33b}$$

where $L = 5 \times 10^9$ m is the arm length of LISA, $S_p = 4 \times 10^{-22}$ m^2 Hz^{-1} is the white position noise level, $S_a = 9 \times 10^{-30}$ m^2 s^{-4} Hz^{-1} is the white acceleration noise level, and $f_* = c/(2\pi L)$ is the arm transfer frequency. This way, we have $S_n(f) = S_n^i(f) + S_n^c(f)$. The different contributions to the noise power spectral density are depicted in Fig. 2.2.

2.2.1 Extrinsic effects in the waveform

To describe extrinsic effects that depend on the position of LISA, we follow [2] and define two different frames: a frame tied to the detector, (x, y, z), and a fixed, Solar System frame, tied to the distant stars $(\bar{x}, \bar{y}, \bar{z})$ (we consider that the motion of the Sun with respect to the distant stars can be neglected during the lifetime of the LISA mission).

The unit vectors along the arms of LISA $\hat{\boldsymbol{l}}_i$, $i \in \{1, 2, 3\}$ are defined in the detector frame by

$$\hat{\boldsymbol{l}}_i = \cos\gamma_i \hat{\boldsymbol{x}} + \sin\gamma_i \hat{\boldsymbol{y}}, \tag{2.34}$$

$$\gamma_i = \frac{\pi}{12} + (i-1)\frac{\pi}{3}. \tag{2.35}$$

The $(\bar{x}, \bar{y})$ plane of the Solar System frame is defined to be the ecliptic, so that the spherical angles of the barycenter of LISA are

$$\bar{\Theta} = \frac{\pi}{2}, \qquad \bar{\Phi}(t) = 2\pi t/T, \tag{2.36}$$

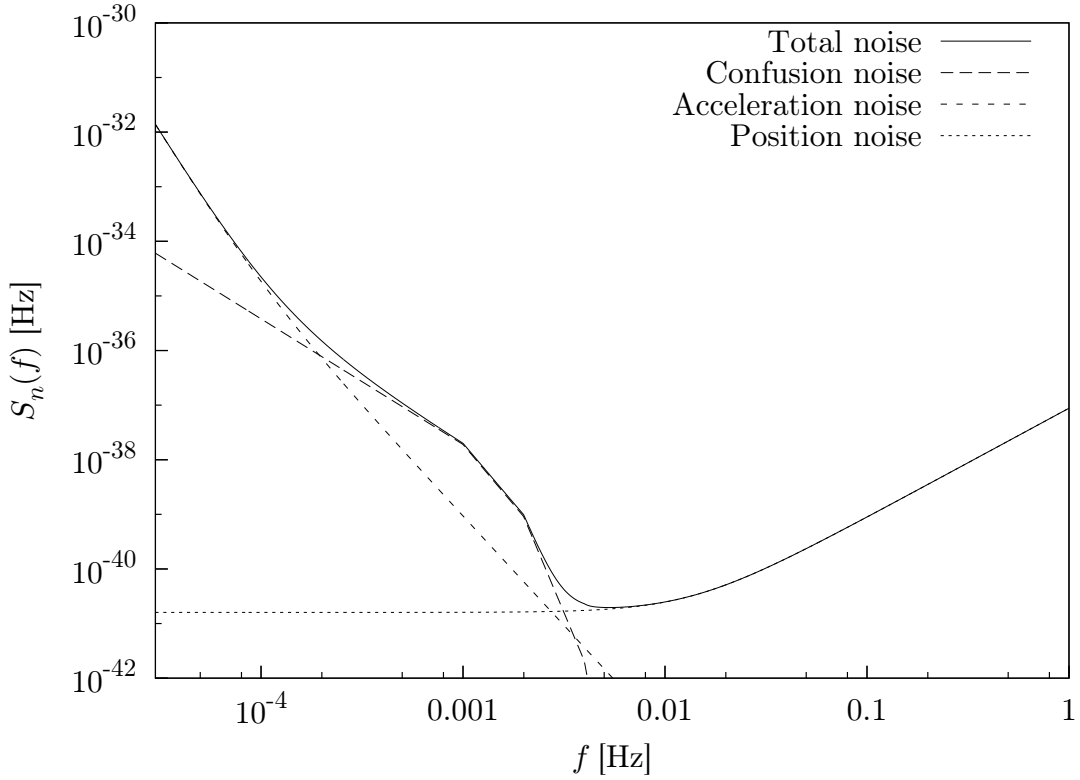

Figure 2.2: One-sided power spectral density of the noise in the LISA detector.

where $T = 1$ yr, and we choose that $\bar{\Phi} = 0$ at $t = 0$.

The normal to the detector plane $\hat{\boldsymbol{z}}$ is at constant angle $\bar{\theta}_z = \pi/3$ from the normal to the ecliptic $\hat{\bar{\boldsymbol{z}}}$, and constantly points in the direction of the $\bar{z}$-axis from the barycenter of LISA. Furthermore, each satellite rotates around the $\hat{\boldsymbol{z}}$-axis once a year (see Fig. 2.1). Let us express the detector frame in the Solar System frame, assuming that $\hat{\boldsymbol{y}} \cdot \hat{\bar{\boldsymbol{y}}} = 1$ at $t = 0$:

$$\hat{\boldsymbol{x}} = \left(\frac{3}{4} - \frac{1}{4}\cos 2\bar{\Phi}(t)\right)\hat{\bar{\boldsymbol{x}}} - \frac{1}{4}\sin 2\bar{\Phi}(t)\hat{\bar{\boldsymbol{y}}} + \frac{\sqrt{3}}{2}\cos\bar{\Phi}(t)\hat{\bar{\boldsymbol{z}}}, \tag{2.37}$$

$$\hat{\boldsymbol{y}} = -\frac{1}{4}\sin 2\bar{\Phi}(t)\hat{\bar{\boldsymbol{x}}} + \left(\frac{3}{4} + \frac{1}{4}\cos 2\bar{\Phi}(t)\right)\hat{\bar{\boldsymbol{y}}} + \frac{\sqrt{3}}{2}\sin\bar{\Phi}(t)\hat{\bar{\boldsymbol{z}}}, \tag{2.38}$$

$$\hat{\boldsymbol{z}} = -\frac{\sqrt{3}}{2}\cos\bar{\Phi}(t)\hat{\bar{\boldsymbol{x}}} - \frac{\sqrt{3}}{2}\sin\bar{\Phi}(t)\hat{\bar{\boldsymbol{y}}} + \frac{1}{2}\hat{\bar{\boldsymbol{z}}}. \tag{2.39}$$

Imagine now a monochromatic gravitational wave coming from a source located on the sky with the spherical angles $(\bar{\theta}_N, \bar{\phi}_N)$ in the Solar System frame. The peculiar motion of the source with respect to the Solar System barycenter can be considered constant during the observation time, and therefore contributes only to the overall redshift. Thus, we can describe the waveform with respect to the Solar System barycenter. However, the motion of

the barycenter of LISA with respect to the one of the Solar System will vary on a timescale of one year, comparable to the observation timescale. Therefore, we have to consider the gravitational wave phase at the position of the barycenter of LISA, and not the one at the barycenter of the Solar System. This is equivalent to adding the so-called *Doppler phase* to the gravitational wave phase:

$$\phi_D(t) = \frac{\omega R}{c} \sin\bar{\theta}_N \cos(\bar{\Phi}(t) - \bar{\phi}_N), \tag{2.40}$$

where $R = 1$ AU, and ω is the angular frequency of the gravitational wave.

Chapter 3

Waveform approximations

In this chapter, we describe the different waveforms that we used in our parameter estimation studies, each based on different assumptions. We begin by introducing spin-induced precession, and the effect it has on our waveforms. Later, we also show how to derive the spin couplings at 2PN order for binaries on eccentric orbits in the evolution equations of the mean motion and the eccentricity [20], together with a smooth circular limit.

The state of a binary system of two Kerr black holes at a given time in the center of mass frame is fully described by 17 parameters. These reduce to 15 if we assume that the binary lies on a circular orbit. We choose them to be

- m_1 and m_2, the individual masses of the black holes,

- $\boldsymbol{S}_1$ and $\boldsymbol{S}_2$, their spins,

- $\hat{\boldsymbol{L}}$, a unit vector pointing in the direction of the orbital angular momentum,

- $\hat{\boldsymbol{N}}$, a unit vector pointing in the direction of the system from the Solar System,

- d_L, the luminosity distance between the source and the Solar System;

we use for binaries on circular orbits

- ω, the orbital angular frequency, and

- φ, the orbital phase;

and we use for binaries on eccentric orbits

- e, the eccentricity,

- n, the periastron-to-periastron frequency or mean motion,

- l, the mean anomaly, and

- λ, a linearly increasing mean phase whose derivative coincides with the mean orbital angular frequency.

Another parameter, the redshift, also plays a role in the determination of the waveform, but it cannot be detected by GW observations. Indeed, redshift causes the observed frequency of the wave f_o to decrease with respect to the emitted one f_e, as $f_o = f_e/(1+z)$. But (see the derivation of the different waveforms) the exact same wave, within the post-Newtonian framework, is emitted by a second system with parameters $m_i^{(2)} = (1+z)m_i^{(1)}$, $d_L^{(2)} = (1+z)d_L^{(1)}$, which is at a redshift of $z = 0$. Therefore, the redshift and luminosity distance cannot be measured separately with a gravitational wave observation, so we must assume a relationship between these two parameters. This implies that observations of a light signal emitted during a merger, the redshift of which is possible to determine, are of great astrophysical interest.

We will sometimes use different parameters, to simplify the equations. For spin parameters, $\boldsymbol{\zeta} = \boldsymbol{S}_1 + \boldsymbol{S}_2$, and $\boldsymbol{\xi} = m_2\boldsymbol{S}_1/m_1 + m_1\boldsymbol{S}_2/m_2$. For mass parameters, the total mass $M = m_1 + m_2$, the reduced mass $\mu = m_1 m_2/M$, and the symmetric mass ratio $\nu = \mu/M$.

3.1 Spin-induced precession

It is well known that a gyroscope on orbit in a Kerr space-time precesses, due to relativistic effects called de Sitter and Lense-Thirring precession. Similarly, a rotating black hole in orbit around another one is affected by the same effects, and its spin precesses. However, if both black holes have comparable mass, their spins give a important contribution to the conserved total angular momentum, and their precession induces a precession of the orbital angular momentum, and therefore of the orbital plane. This in turn affects the phase of the gravitational waves emitted.

This effect was first described in [21]. The time derivatives of the spins and of the orbital angular momentum are given for a system on an eccentric orbit by

$$\dot{\boldsymbol{S}}_i = \frac{\omega_m^2}{Mc^2\left(1-e^2\right)^{3/2}}\left[\left(2+\frac{3m_j}{2m_i}\right)\boldsymbol{L} + \frac{1}{2}\boldsymbol{S}_j - \frac{3}{2}\left(\hat{\boldsymbol{L}}\cdot\boldsymbol{S}_j\right)\hat{\boldsymbol{L}}\right]\times\boldsymbol{S}_i, \tag{3.1}$$

$$\dot{\hat{\boldsymbol{L}}} = \frac{\omega_m^2}{Mc^2\left(1-e^2\right)^{3/2}}\left\{2\boldsymbol{\zeta} + \frac{3}{2}\boldsymbol{\xi} - \frac{3}{2L}\left[\left(\hat{\boldsymbol{L}}\cdot\boldsymbol{S}_2\right)\boldsymbol{S}_1 + \left(\hat{\boldsymbol{L}}\cdot\boldsymbol{S}_1\right)\boldsymbol{S}_2\right]\right\}\times\hat{\boldsymbol{L}}, \tag{3.2}$$

where ω_m is the mean orbital frequency of the system. As these relationships are leading order ones, we can use Newtonian quantities to compute them, in particular the norm of the orbital angular momentum.

Gravitational waveforms in the literature are commonly defined with respect to an orbital phase taken relative to the principal+ direction, which is defined as the direction of the vector $\hat{\boldsymbol{L}}\times\hat{\boldsymbol{N}}$ [5]. As the orbital angular momentum precesses, the principal+ direction changes, and this must be taken into account in the waveform.

To calculate the correction to the orbital phase arising from this effect, we define a set of two basis vectors in the orbital plane, as

$$\boldsymbol{e}_1 = \frac{\hat{\boldsymbol{L}} \times \hat{\boldsymbol{N}}}{\sqrt{1 - \left(\hat{\boldsymbol{L}} \cdot \hat{\boldsymbol{N}}\right)^2}}, \tag{3.3}$$

$$\boldsymbol{e_2} = \hat{\boldsymbol{L}} \times \boldsymbol{e}_1. \tag{3.4}$$

The orbital separation is then, by definition, along the vector

$$\hat{\boldsymbol{r}} = \cos\varphi \boldsymbol{e}_1 + \sin\varphi \boldsymbol{e}_2, \tag{3.5}$$

where φ denotes the orbital phase, and we have that

$$\dot{\hat{\boldsymbol{r}}} = \omega \hat{\boldsymbol{L}} \times \hat{\boldsymbol{r}} - \hat{\boldsymbol{L}} \left(\dot{\hat{\boldsymbol{L}}} \cdot \hat{\boldsymbol{r}}\right), \tag{3.6}$$

where ω denotes the instantaneous orbital frequency of the system.

From (3.5), we have

$$\cos\varphi = \hat{\boldsymbol{r}} \cdot \boldsymbol{e}_1, \tag{3.7}$$

and thus

$$-\dot{\varphi}\sin\varphi = -\omega\sin\varphi + \hat{\boldsymbol{r}} \cdot \dot{\boldsymbol{e}}_1 = -\sin\varphi\left(\omega - \boldsymbol{e}_2 \cdot \dot{\boldsymbol{e}}_1\right). \tag{3.8}$$

This effect thus leads to a correction to the orbital phase, given by

$$\delta\varphi(t) = -\int \boldsymbol{e}_2 \cdot \dot{\boldsymbol{e}}_1 dt = \int \frac{\hat{\boldsymbol{L}} \cdot \hat{\boldsymbol{N}}}{1 - \left(\hat{\boldsymbol{L}} \cdot \hat{\boldsymbol{N}}\right)^2} \left(\hat{\boldsymbol{L}} \times \hat{\boldsymbol{N}}\right) \cdot \dot{\hat{\boldsymbol{L}}} dt. \tag{3.9}$$

We must mention that when we describe an eccentric waveform, this effect only affects the orbital phase, but neither the mean, true, nor eccentric anomaly, which are defined relative to the periastron line. Indeed, this effect arises from the fact that in a frame tied to the orbital plane, $\hat{\boldsymbol{N}}$ is seen to precess, and this in turn induces a precession of $\boldsymbol{e}_1$ and $\boldsymbol{e}_2$, but not of the periastron line.

3.2 Circular waveforms

To calculate the waveform for a binary system at 2PN order, we need to solve the 2PN equations of motion and find a suitable parametrization for the orbit. From this, we can compute the gravitational radiation emitted by the system, equate the luminosity and angular momentum thereof with the time derivative of the 2PN energy and angular momentum of the system, and infer the evolution equations of the orbital parameters from this.

This has been done in [22], and we get that the 2PN orbit-averaged relation between the orbital angular frequency ω and the orbital separation in harmonic coordinates r is given by

$$\omega = \frac{c^3}{GM}\gamma^{3/2}\left[1+\left(\frac{\nu}{2}-\frac{3}{2}\right)\gamma-\frac{1}{2}\beta(2,3)\gamma^{3/2}+\left(\frac{15}{8}+\frac{47\nu}{8}+\frac{3\nu^2}{8}-\frac{3}{4}\sigma(1,3)\right)\gamma^2\right], \quad (3.10)$$

where the orbital separation parameter γ and the spin-orbit and spin-spin couplings β and σ are given by

$$\gamma = \frac{GM}{rc^2}, \quad (3.11)$$

$$\beta(a,b) = \frac{c}{GM^2}\left(a\boldsymbol{\zeta}+b\boldsymbol{\xi}\right)\cdot\hat{\boldsymbol{L}}, \quad (3.12)$$

$$\sigma(a,b) = \frac{c^2}{G^2M^4\nu}\left[a\boldsymbol{S}_1\cdot\boldsymbol{S}_2-b\left(\boldsymbol{S}_1\cdot\hat{\boldsymbol{L}}\right)\left(\boldsymbol{S}_2\cdot\hat{\boldsymbol{L}}\right)\right]. \quad (3.13)$$

The orbital frequency parameter x is given by

$$x \equiv \left(\frac{GM\omega}{c^3}\right)^{2/3}, \quad (3.14)$$

and the evolution equation for the orbital angular frequency is

$$\frac{dx}{dt} = \frac{64\nu}{5}\frac{c^3}{GM}x^5\left[1-\left(\frac{743}{336}+\frac{11\nu}{4}\right)x+\left(4\pi-\frac{1}{12}\beta(113,75)\right)x^{3/2}\right.$$
$$\left.+\left(\frac{34\,103}{18\,144}+\frac{13\,661\nu}{2016}+\frac{59\nu^2}{18}-\frac{1}{48}\sigma(247,721)\right)x^2\right]. \quad (3.15)$$

We can integrate Eq. (3.15) to get

$$t = t_c-\frac{5GM}{256\nu c^3}x^{-4}\left[1+\left(\frac{743}{252}+\frac{11\nu}{3}\right)x+\left(\frac{2}{15}\beta(113,75)-\frac{32}{5}\pi\right)x^{3/2}\right.$$
$$\left.+\left(\frac{3\,058\,673}{508\,032}+\frac{5429\nu}{504}+\frac{617\nu^2}{72}+\frac{1}{24}\sigma(247,721)\right)x^2\right]. \quad (3.16)$$

Integrating once more yields the orbital phase $\varphi = \int\omega dt$, as a function of the orbital frequency parameter

$$\varphi(x) = \varphi_c-\frac{x^{-5/2}}{32\nu}\left[1+\left(\frac{3715}{1008}+\frac{55\nu}{12}\right)x+\left(\frac{5}{24}\beta(113,75)-10\pi\right)x^{3/2}\right.$$
$$\left.+\left(\frac{15\,293\,365}{1\,016\,064}+\frac{27\,145\nu}{1008}+\frac{3085\nu^2}{144}+\frac{5}{48}\sigma(247,721)\right)x^2\right]. \quad (3.17)$$

Using the spin-induced precession equations together with the first order of Eq. (3.15), we can change variables from time to orbital angular frequency, and use the relations to write the precession equations as

$$\frac{d\boldsymbol{S}_i}{d\omega} = \frac{5}{96}\frac{c^3}{GM}\omega^{-2}\left[\hat{\boldsymbol{L}}\times\boldsymbol{\Sigma}_i + \frac{1}{2L}\left(\boldsymbol{S}_j - 3\left(\boldsymbol{S}_j\cdot\hat{\boldsymbol{L}}\right)\hat{\boldsymbol{L}}\right)\times\boldsymbol{S}_i\right], \tag{3.18}$$

$$\begin{aligned}\frac{d\hat{\boldsymbol{L}}}{d\omega} &= \frac{5}{96}\frac{c^3}{GM}\omega^{-2}\frac{1}{L}\left[\boldsymbol{\Sigma}_1 + \boldsymbol{\Sigma}_2 - \frac{3}{2L}\left(\boldsymbol{\sigma}_1 + \boldsymbol{\sigma}_2\right)\right]\times\hat{\boldsymbol{L}} \\ &= -\frac{1}{L}\left(\frac{d\boldsymbol{S}_1}{d\omega} + \frac{d\boldsymbol{S}_2}{d\omega}\right),\end{aligned} \tag{3.19}$$

where

$$L = \mu\left(\frac{G^2M^2}{\omega}\right)^{1/3}, \tag{3.20}$$

$$\boldsymbol{\Sigma}_i = \left(2 + \frac{3m_j}{2m_i}\right)\boldsymbol{S}_i, \tag{3.21}$$

$$\boldsymbol{\sigma}_i = \left(\boldsymbol{S}_j\cdot\hat{\boldsymbol{L}}\right)\boldsymbol{S}_i. \tag{3.22}$$

The waveform is a series of harmonics of the orbital frequency:

$$h_{+,\times} = \frac{2GM\nu x}{d_L c^2}\left[\sum_{n\geq 0}\left(A^{(n)}_{+,\times}\cos n\phi + B^{(n)}_{+,\times}\sin n\phi\right)\right], \tag{3.23}$$

where ϕ is the orbital phase (3.17) corrected by the factor coming from spin-induced precession (3.9), like

$$\phi = \varphi + \delta\varphi. \tag{3.24}$$

The coefficients of the series take the form of post-Newtonian series:

$$A^{(n)}_{+,\times} = \sum_{i\geq 0} a^{(n,i/2)}_{+,\times}x^{i/2}, \tag{3.25}$$

$$B^{(n)}_{+,\times} = \sum_{i\geq 0} b^{(n,i/2)}_{+,\times}x^{i/2}. \tag{3.26}$$

The exact form of the coefficients for a nonspinning system can be found in [23, 24]. Note however, that both express their final result using another phase which differs from the orbital phase at 1.5PN order: $\Psi = \phi - 2\log(\omega/\bar{\omega})x^{3/2}$, where $\bar{\omega}$ is an arbitrary constant. We included for completeness the expressions that we used in our study described in Chapter 4 in appendix A.

To take the Doppler phase (2.40) into account, it is sufficient to add a correction to the orbital phase as

$$\psi = \phi + \phi_D = \phi + \frac{\omega R}{c}\sin\bar{\theta}_N\cos(\bar{\Phi} - \bar{\phi}_N). \tag{3.27}$$

This way, each harmonic contains the correct correction.

Using this, we find the response function of the detectors (2.27) ($k = 1, 2$):

$$h_k = \frac{\sqrt{3}GM\nu x}{d_L c^2} \sum_{n\geq 0} \left[\sum_{i\geq 0} \left(F_k^+(t) a_+^{(n,i/2)} + F_k^\times(t) a_\times^{(n,i/2)} \right) x^{i/2} \cos n\psi \right.$$
$$\left. + \sum_{i\geq 0} \left(F_k^+(t) b_+^{(n,i/2)} + F_k^\times(t) b_\times^{(n,i/2)} \right) x^{i/2} \sin n\psi \right] \tag{3.28}$$
$$= \frac{\sqrt{3}GM\nu x}{d_L c^2} \sum_{n\geq 0} \left[A_{k,n}(t) \cos n\psi + B_{k,n}(t) \sin n\psi \right]. \tag{3.29}$$

We can change this into the phase-amplitude representation:

$$h_k = \frac{\sqrt{3}GM\nu x}{d_L c^2} \left[A_+^{(0)}(t) F_k^+(t) + \sum_{n\geq 1} A_{k,n}^{pol}(t) \cos\left(n\psi + \phi_{k,n}^{pol}(t) \right) \right], \tag{3.30}$$

where $\phi_{k,n}^{pol}$ is the polarization phase, and $A_{k,n}^{pol}$ is the polarization amplitude:

$$\tan \phi_{k,n}^{pol} = -\frac{B_{k,n}}{A_{k,n}}, \tag{3.31}$$
$$A_{k,n}^{pol} = \mathrm{sgn}(A_{k,n}) \sqrt{A_{k,n}^2 + B_{k,n}^2}. \tag{3.32}$$

The final form of the gravitational wave signal is thus

$$h_k = \frac{\sqrt{3}GM\nu x}{d_L c^2} \left[A_+^{(0)} F_k^+ + \sum_{n\geq 1} A_{k,n}^{pol} \cos \psi_{k,n} \right], \tag{3.33}$$
$$\psi_{k,n} = n(\varphi + \delta\varphi + \phi_D) + \phi_{k,n}^{pol}. \tag{3.34}$$

To estimate the measurement error in the different parameters of the binary, we need to know the Fourier transform of the signal $\tilde{h}_k(f)$ [1].

$$\tilde{h}_k(f) = \int_{-\infty}^{\infty} h_k(t) e^{2\pi i f t} dt$$
$$= \frac{\sqrt{3}GM\nu}{d_L c^2} \left[\int_{-\infty}^{\infty} x \sum_{n\geq 1} A_{k,n}^{pol} \cos \psi_{k,n} e^{2\pi i f t} dt + \int_{-\infty}^{\infty} x A_+^{(0)} F_k^+ e^{2\pi i f t} dt \right]$$
$$\approx \frac{\sqrt{3}GM\nu}{2d_L c^2} \sum_{n\geq 1} \left[\int_{-\infty}^{\infty} x A_{k,n}^{pol} e^{i(2\pi f t + \psi_{k,n})} dt + \int_{-\infty}^{\infty} x A_{k,n}^{pol} e^{i(2\pi f t - \psi_{k,n})} dt \right]. \tag{3.35}$$

[1] Note that the symbol f here and in the following pages denotes the argument of the Fourier transform of the signal, and not the orbital frequency.

Note that in the last line, we neglect the Fourier transform of the so-called memory effect $A_+^{(0)}$. This is based on the fact that the Fourier transform of the function $xA_+^{(0)}F_k^+$ accumulates around frequencies which are separated from the orbital frequency range, at least during most of the inspiral. It thus does not contribute to the frequencies of interest.

To compute the integrals, we rely on the stationary phase approximation. Neglecting the integrals with factors of $e^{i(2\pi ft+\psi_{k,n})}$ (as they only contribute to negative frequencies) the stationary points for the other integrals are given by

$$2\pi f = \psi'_{k,n}(t_{k,n}) = n\omega(t_{k,n}) + n\phi'_D(t_{k,n}) + (\phi^{pol}_{k,n})'(t_{k,n}). \tag{3.36}$$

For the same reasons as before, we can safely neglect the derivatives of the Doppler phase and of the polarization phase. We get the following expression for the stationary point:

$$t_{k,n} = t_n = t(f/n), \tag{3.37}$$

where the function $t(f)$ is defined at 2PN order by Eq. (3.16).

Thus, we arrive at the following expression for the Fourier transform of the gravitational wave signal:

$$\begin{aligned}\tilde{h}_k(f) = \frac{\sqrt{5\pi\nu}G^2M^2}{8d_Lc^5}\sum_{n\geq 1} A^{pol}_{k,n}[t(f/n)]x_n{}^{-7/4}S(f/n)\\ \cdot\exp\left\{i\Big[n\Big(\Psi(f/n)-\delta\varphi(f/n)-\phi_D[t(f/n)]\Big)-\phi^{pol}_{k,n}[t(f/n)]\Big]\right\},\end{aligned} \tag{3.38}$$

where $x_n = x(f/n) = n^{-2/3}x$, and

$$\begin{aligned}S(f) = \left[1+\left(\frac{743}{672}+\frac{11\nu}{8}\right)x+\left(\frac{1}{24}\beta(113,75)-2\pi\right)x^{3/2}\right.\\ \left.+\left(\frac{7\,266\,251}{8\,128\,512}+\frac{18\,913\nu}{16\,128}+\frac{1379\nu^2}{1152}+\frac{1}{96}\sigma(247,721)\right)x^2\right],\end{aligned} \tag{3.39}$$

$$\begin{aligned}\Psi(f) = \left(\frac{t_cc^3}{GM}\right)x^{3/2}-\varphi_c-\frac{\pi}{4}+\frac{3x^{-5/2}}{256\nu}\left[1+\left(\frac{3715}{756}+\frac{55\nu}{9}\right)x+\left(\frac{1}{3}\beta(113,75)\right.\right.\\ \left.\left.-16\pi\right)x^{3/2}+\left(\frac{15\,293\,365}{508\,032}+\frac{27\,145\nu}{504}+\frac{3085\nu^2}{72}+\frac{5}{24}\sigma(247,721)\right)x^2\right],\end{aligned} \tag{3.40}$$

where we used here $x = x(\omega = 2\pi f)$, a different orbital frequency parameter for each harmonic.

Finally, we must take into account that a binary will be observed with LISA during a finite amount of time. Therefore, if we denote t_i and t_f to be the initial and final times of observation respectively, the orbital frequencies available for the Fourier transform will lie between $f_{orb}(t_i)$ and $f_{orb}(t_f)$. This means that the final Fourier transform is of the form:

$$\tilde{h}_k(f) = \sum_{n\geq 1}\tilde{h}_{k,n}(f)\theta(f-nf_{orb}(t_i))\theta(nf_{orb}(t_f)-f), \tag{3.41}$$

where θ is the Heaviside step function.

In our work, we used three different approximations, all based on this circular waveform: the full waveform (FWF), the simplified waveform (SWF), and the restricted waveform (RWF).

The FWF contains all post-Newtonian corrections to the frequency and amplitude of the wave up to 2PN order. It is obtained using the amplitudes given in appendix A in Eqs. (3.31) and (3.32), and inserting the results in Eq. (3.38).

The SWF contains all post-Newtonian corrections of the frequency up to 2PN order, and the lowest order amplitude of each harmonic present at the 2PN level. With this approximation, we find particularly simple forms for the polarization amplitudes and phases (with $F_{+,\times} = F_k^{+,\times}$, $c_i = \hat{\boldsymbol{L}} \cdot \hat{\boldsymbol{N}}$, $s_i = |\hat{\boldsymbol{L}} \times \hat{\boldsymbol{N}}|$):

$$A_{k,1}^{pol} = -\mathrm{sgn}(F_+)\frac{x^{1/2}s_i}{8}\sqrt{1-4\nu}\,\sqrt{F_+^2\left(5+c_i^2\right)^2 + 36F_\times^2 c_i^2}, \tag{3.42a}$$

$$A_{k,2}^{pol} = -\mathrm{sgn}(F_+)\sqrt{F_+^2\left(1+c_i^2\right)^2 + 4F_\times^2 c_i^2}, \tag{3.42b}$$

$$A_{k,3}^{pol} = -\frac{9x^{1/2}s_i}{8}\sqrt{1-4\nu}A_{k,2}^{pol}, \tag{3.42c}$$

$$A_{k,4}^{pol} = \frac{4xs_i^2}{3}(1-3\nu)A_{k,2}^{pol}, \tag{3.42d}$$

$$A_{k,5}^{pol} = -\frac{625x^{3/2}s_i^3}{384}\sqrt{1-4\nu}(1-2\nu)A_{k,2}^{pol}, \tag{3.42e}$$

$$A_{k,6}^{pol} = \frac{81x^2s_i^4}{40}(1-5\nu+5\nu^2)A_{k,2}^{pol}, \tag{3.42f}$$

$$\phi_{k,1}^{pol} = -\arctan\left(\frac{6c_iF_\times}{(5+c_i^2)F_+}\right), \tag{3.42g}$$

$$\phi_{k,n}^{pol} = -\arctan\left(\frac{2c_iF_\times}{(1+c_i^2)F_+}\right), \qquad n \geq 2. \tag{3.42h}$$

The SWF is obtained by inserting the polarization amplitudes and phases above into Eq. (3.38) and, consistently with neglecting all amplitude corrections, taking the lowest order of the overall amplitude correction, i.e. $S(f) = 1$.

The RWF contains all post-Newtonian corrections of the frequency up to 2PN order, and the lowest-order amplitude of the second harmonic. It is identical to the SWF, with the further approximation $A_{k,n}^{pol} = \phi_{k,n}^{pol} = 0,\ n \neq 2$.

3.3 Spin couplings for binaries on eccentric orbits

To find a waveform for binaries on eccentric orbits, we need to have a suitable parametrization of the orbit, as well as evolution equations for the orbital parameters.

Let us consider a system of two Kerr black holes orbiting each other. What we want to find is a quasi-Keplerian parametrization, i.e. a parametrization of the orbit that reduces

to a Keplerian one in the Newtonian limit, valid at 2PN order, and regular in the circular limit. After that, we will find the evolution equations for the mean motion, defined as the periastron-to-periastron frequency, and for the eccentricity in the adiabatic approximation, i.e. neglecting the backreaction to gravitational wave emission. This prescription is safe, as we are looking for the 2PN order solution, and backreaction occurs at 2.5PN order. As this has already been solved in [25] for the case of binaries without spin, we focus on the spin effects only. As spin-orbit couplings appear at 1.5PN order and spin-spin couplings at 2PN order, it is sufficient to consider only the Newtonian and spin-coupling terms in the equations of motion.

For brevity, we use in this section a system of units where $G = c = M = 1$. We also denote the orbital angular momentum of the system by $\boldsymbol{J}$, and reserve the symbol L for the angular average of its norm. We start from the generalized Lagrangian in the center of mass frame used in [26, 27]:

$$\mathcal{L} = \frac{\nu}{2}\boldsymbol{v}^2 + \frac{\nu}{r} + \frac{\nu}{2}(\boldsymbol{v}\times\boldsymbol{a})\cdot\boldsymbol{\xi} - \frac{2\nu}{r^2}(\hat{\boldsymbol{r}}\times\boldsymbol{v})\cdot(\boldsymbol{\zeta}+\boldsymbol{\xi}) \quad + \frac{1}{r^3}\boldsymbol{S}_1\cdot\boldsymbol{S}_2 - \frac{3}{r^3}\left(\hat{\boldsymbol{r}}\cdot\boldsymbol{S}_1\right)\left(\hat{\boldsymbol{r}}\cdot\boldsymbol{S}_2\right), \tag{3.43}$$

where $\boldsymbol{r}$ is the binary separation.

The equations of motion are

$$p^i = \frac{\partial\mathcal{L}}{\partial v^i} - \frac{d}{dt}s^i, \tag{3.44}$$

$$\frac{dp^i}{dt} = \frac{\partial\mathcal{L}}{\partial x^i}, \tag{3.45}$$

where $s^i = \partial\mathcal{L}/\partial a^i$.

We can solve them order-by-order, which gives at 2PN order

$$\boldsymbol{p} = \nu\boldsymbol{v} + \frac{\nu}{r^2}\hat{\boldsymbol{r}}\times(2\boldsymbol{\zeta}+\boldsymbol{\xi}), \tag{3.46}$$

$$\begin{aligned}\boldsymbol{a} = &-\frac{\hat{\boldsymbol{r}}}{r^2} + \frac{\hat{\boldsymbol{r}}\cdot\boldsymbol{v}}{r^3}\hat{\boldsymbol{r}}\times(6\boldsymbol{\zeta}+3\boldsymbol{\xi}) - \frac{1}{r^3}\boldsymbol{v}\times(4\boldsymbol{\zeta}+3\boldsymbol{\xi}) + \frac{\hat{\boldsymbol{r}}}{r^3}(\hat{\boldsymbol{r}}\times\boldsymbol{v})\cdot(6\boldsymbol{\zeta}+6\boldsymbol{\xi})\\ &- \frac{3\hat{\boldsymbol{r}}}{\nu r^4}\boldsymbol{S}_1\cdot\boldsymbol{S}_2 - \frac{3}{\nu r^4}\left[\left(\hat{\boldsymbol{r}}\cdot\boldsymbol{S}_2\right)\boldsymbol{S}_1 + \left(\hat{\boldsymbol{r}}\cdot\boldsymbol{S}_1\right)\boldsymbol{S}_2\right] + \frac{15\hat{\boldsymbol{r}}}{\nu r^4}\left(\hat{\boldsymbol{r}}\cdot\boldsymbol{S}_1\right)\left(\hat{\boldsymbol{r}}\cdot\boldsymbol{S}_2\right).\end{aligned} \tag{3.47}$$

The reduced energy and reduced orbital angular momentum are given by

$$\begin{aligned}\boldsymbol{J} &= \frac{1}{\nu}\left(\boldsymbol{r}\times\boldsymbol{p} + \boldsymbol{v}\times\boldsymbol{s}\right)\\ &= \boldsymbol{r}\times\boldsymbol{v} + \frac{1}{r}\hat{\boldsymbol{r}}\times[\hat{\boldsymbol{r}}\times(2\boldsymbol{\zeta}+\boldsymbol{\xi})] - \frac{1}{2}\boldsymbol{v}\times(\boldsymbol{v}\times\boldsymbol{\xi}),\end{aligned} \tag{3.48}$$

$$\begin{aligned}E &= \frac{1}{\nu}\left(\boldsymbol{p}\cdot\boldsymbol{v} + \boldsymbol{s}\cdot\boldsymbol{a} - \mathcal{L}\right)\\ &= \frac{1}{2}\boldsymbol{v}^2 - \frac{1}{r} + \frac{1}{r^2}(\hat{\boldsymbol{r}}\times\boldsymbol{v})\cdot\boldsymbol{\xi} - \frac{1}{\nu r^3}\boldsymbol{S}_1\cdot\boldsymbol{S}_2 + \frac{3}{\nu r^3}\left(\hat{\boldsymbol{r}}\cdot\boldsymbol{S}_1\right)\left(\hat{\boldsymbol{r}}\cdot\boldsymbol{S}_2\right).\end{aligned} \tag{3.49}$$

The magnitude of $\boldsymbol{J}$ is not constant along an orbit [28]. Indeed, due to spin-spin interactions, both spin vectors undergo a precessional motion (see Section 3.1) and thus, from the conservation of the total angular momentum, it follows that J changes at 2PN order. If we denote its angular average (with respect to the true anomaly v, defined later) by L, and define $A = \sqrt{1+2EL^2}$, we get

$$\begin{aligned} J &= L - \frac{1}{2\nu L^3}\left|\hat{\boldsymbol{J}}\times\boldsymbol{S}_1\right|\left|\hat{\boldsymbol{J}}\times\boldsymbol{S}_2\right|\{2A\cos(v-2\psi)+(3+2A\cos v)\cos[2(v-\psi)]\} = \\ &= L - \frac{\gamma_2}{2L^3}\{3A\cos(v-2\psi)+3\cos[2(v-\psi)]+A\cos(3v-2\psi)\}, \end{aligned} \tag{3.50}$$

$$\gamma_2 = \frac{1}{\nu}\left|\hat{\boldsymbol{J}}\times\boldsymbol{S}_1\right|\left|\hat{\boldsymbol{J}}\times\boldsymbol{S}_2\right|, \tag{3.51}$$

where ψ is the angle subtended by the bisector of the projections of $\boldsymbol{S}_i$ in the plane of motion and the periastron line.

We can find a two parameter family of quasi-Keplerian parametrization of the equations of motion by taking the ansatz

$$r = a\,(1-e_r\cos u) + f_{r,1}\cos(v-2\psi) + f_{r,2}\cos(2v-2\psi), \tag{3.52}$$

$$\phi = (1+k)v + f_{\phi,1}\sin(v-2\psi) + f_{\phi,2}\sin(2v-2\psi) + f_{\phi,3}\sin(3v-2\psi), \tag{3.53}$$

$$v = 2\arctan\left(\sqrt{\frac{1+e_\phi}{1-e_\phi}}\tan\frac{u}{2}\right), \tag{3.54}$$

$$l = n(t-t_0) = u - e_t\sin u + f_t\sin(v-2\psi), \tag{3.55}$$

where (r,ϕ) is a polar coordinate system in the plane of motion, n is the mean motion, u, v, and l are the eccentric, true, and mean anomalies, a is the semi-major axis, e_t, e_r, and e_ϕ are eccentricities, k accounts for perihelion precession, and the f_i are constants.

The constants are

$$n = (-2E)^{3/2}, \tag{3.56}$$

$$a = -\frac{1}{2E}\left[1 - \frac{E}{L}\beta(4,2) - \frac{E}{L^2}\gamma_1 - \lambda_1 A\frac{E}{L^2}\gamma_2\cos 2\psi\right], \tag{3.57}$$

$$k = -\frac{1}{L^3}\beta\,(4,3) - \frac{3}{2L^4}\gamma_1, \tag{3.58}$$

$$e_t^2 = A^2 + \frac{E}{L}\beta\left(8, 6-2A^2\right) + 2\frac{E}{L^2}\left(\gamma_1 + A\lambda_2\gamma_2\cos 2\psi\right), \tag{3.59}$$

$$e_r^2 = e_t^2 + A^2\left[\frac{E}{L}\beta(8,4) + 2\frac{E}{L^2}\left(\gamma_1 + A\lambda_1\gamma_2\cos 2\psi\right)\right], \tag{3.60}$$

$$e_\phi^2 = e_t^2 + A^2\left[\frac{E}{L}\beta(8,8) + 2\frac{E}{L^2}\left(2\gamma_1 + A\lambda_1\gamma_2\cos 2\psi\right)\right], \tag{3.61}$$

$$f_t = \lambda_1\frac{(-2E)^{3/2}}{L}\gamma_2, \tag{3.62}$$

$$f_{r,1} = -\frac{\lambda_2}{2}\frac{1}{L^2}\gamma_2, \tag{3.63}$$

$$f_{r,2} = -\frac{1+\lambda_1 A}{2}\frac{1}{L^2}\gamma_2, \tag{3.64}$$

$$f_{\phi,1} = -\left[A - \lambda_1\left(1+\frac{3A^2}{4}\right) - \lambda_2\right]\frac{1}{L^4}\gamma_2, \tag{3.65}$$

$$f_{\phi,2} = -\frac{1-4A\lambda_1 - A\lambda_2}{4}\frac{1}{L^4}\gamma_2, \tag{3.66}$$

$$f_{\phi,3} = \frac{\lambda_1 A^2}{4}\frac{1}{L^4}\gamma_2, \tag{3.67}$$

where λ_1 and λ_2 are arbitrary functions of A, and

$$\beta(a,b) = \hat{\boldsymbol{J}}\cdot(a\boldsymbol{\zeta} + b\boldsymbol{\xi}), \tag{3.68}$$

$$\gamma_1 = \frac{1}{\nu}\left[\boldsymbol{S}_1\cdot\boldsymbol{S}_2 - 3\left(\hat{\boldsymbol{J}}\cdot\boldsymbol{S}_1\right)\left(\hat{\boldsymbol{J}}\cdot\boldsymbol{S}_2\right)\right]. \tag{3.69}$$

The Keresztes-Mikóczi-Gergely (KMG) quasi-Keplerian parametrization of the orbit [29] is obtained by imposing $f_{r,i} = 0$, which leads to $\lambda_2 = 0$ and $\lambda_1 = -1/A$. However, this parametrization is singular in the circular limit $e_t \to 0$. To fix λ_1 and λ_2, we prefer to impose that the values of the semi-major axis and of the eccentricities should not depend on the position of the periastron line in the orbital plane. This implies $\lambda_1 = \lambda_2 = 0$, and that this parametrization is free of divergences in the zero eccentricity limit as we will later see.

The quasi-Keplerian parametrization then simplifies to

$$r = a\left(1 - e_r\cos u\right) + f_{r,2}\cos[2(v-\psi)], \tag{3.70}$$

$$\phi = (1+k)v + f_{\phi,1}\sin(v-2\psi) + f_{\phi,2}\sin[2(v-\psi)], \tag{3.71}$$

$$v = 2\arctan\left(\sqrt{\frac{1+e_\phi}{1-e_\phi}}\tan\frac{u}{2}\right), \tag{3.72}$$

$$l = n(t-t_0) = u - e_t\sin u. \tag{3.73}$$

Note that the periastron line (defined by the equation $u = v = 2p\pi$, $p \in \mathbb{Z}$) does no longer correspond to $r = r_{\min}$ as in the Newtonian case.

The singularity in the KMG parametrization comes from the fact that the authors used as a definition of the eccentric anomaly (denoted in their paper by ξ)

$$r(\xi) = \frac{1}{2}\left[r_{\max} + r_{\min} - (r_{\max} - r_{\min})\cos\xi\right], \tag{3.74}$$

which leads to Eq. (3.70) with $f_{r,2} = 0$. The zero eccentricity limit of the equations of motion $r(\phi)$ and $d\phi/dt$ (see section 3.3.1) leads to $r = \bar{r} + \delta r \cos[2(\phi - \psi)]$. If $f_{r,2} = 0$ in Eq. (3.70), this angular dependence must come from the change of variables $u(\phi)$. To cancel the $e_r = O(e)$ factor in front of $\cos(u)$ so that the angular dependence does not vanish in the zero eccentricity limit, the function $u(\phi)$ must be of order $O(e^{-1})$. This is the origin of the apparent singularity in the quasi-Keplerian parametrization found in [29].

The mean motion and time eccentricity are given, in terms of E and L, as

$$n = (-2E)^{3/2}, \tag{3.75}$$

$$e_t^2 = A^2 + \frac{E}{L}\beta\left(8, 6 - 2A^2\right) + 2\frac{E}{L^2}\gamma_1, \tag{3.76}$$

We can invert these relations and find E and L as functions of the post-Newtonian parameter $x = n^{2/3}$ and the eccentricity $e = e_t$. These are

$$E = -\frac{x}{2}, \tag{3.77}$$

$$L = \frac{\sqrt{1-e^2}}{x^{1/2}}\left[1 - \frac{x^{3/2}\beta\left(4, 3 - e^2\right)}{2\left(1-e^2\right)^{3/2}} - \frac{x^2\gamma_1}{2\left(1-e^2\right)^2}\right]. \tag{3.78}$$

These expressions allow us to express the constant parameters of the quasi-Keplerian motion as

$$a = x^{-1}\left[1 + \frac{x^{3/2}\beta(2,1)}{\sqrt{1-e^2}} + \frac{x^2\gamma_1}{2\left(1-e^2\right)}\right], \tag{3.79}$$

$$k = -\frac{x^{3/2}\beta\left(4,3\right)}{\left(1-e^2\right)^{3/2}} - \frac{3x^2\gamma_1}{2\left(1-e^2\right)^2}, \tag{3.80}$$

$$e_r = e\left[1 - \frac{x^{3/2}\beta\left(2,1\right)}{\sqrt{1-e^2}} - \frac{x^2\gamma_1}{2\left(1-e^2\right)}\right], \tag{3.81}$$

$$e_\phi = e\left[1 - \frac{x^{3/2}\beta\left(2,2\right)}{\sqrt{1-e^2}} - \frac{x^2\gamma_1}{\left(1-e^2\right)}\right], \tag{3.82}$$

$$f_r = -\frac{x}{2\left(1-e^2\right)}\gamma_2, \tag{3.83}$$

$$f_{\phi,1} = -\frac{ex^2}{\left(1-e^2\right)^2}\gamma_2, \tag{3.84}$$

$$f_{\phi,2} = -\frac{x^2}{4\left(1-e^2\right)^2}\gamma_2. \tag{3.85}$$

We can now use the results from [30, 28], in which the orbit-averaged values of dE/dt and dL/dt due to the emission of gravitational waves were computed:

$$\frac{dE}{dt} = \nu\left(\dot{E}_N + \dot{E}_{SO} + \dot{E}_{SS}\right), \tag{3.86}$$

$$\frac{dL}{dt} = \nu\left(\dot{L}_N + \dot{L}_{SO} + \dot{L}_{SS}\right), \tag{3.87}$$

where

$$\dot{E}_N = -\frac{(-2E)^{3/2}}{15L^7}\left(96+292A^2+37A^4\right), \tag{3.88}$$

$$\dot{E}_{SO} = \frac{(-2E)^{3/2}}{10L^{10}}\beta\left(2704+7320A^2+2490A^4+65A^6, 1976+5096A^2+1569A^4+32A^6\right), \tag{3.89}$$

$$\begin{aligned}\dot{E}_{SS} = \frac{(-2E)^{3/2}}{960L^{11}}\big[&2\sigma\big(42\,048+154\,272A^2+75\,528A^4+3084A^6, 124\,864+450\,656A^2\\ &+215\,544A^4+8532A^6, 131\,344A^2+127\,888A^4+7593A^6\big)-\tau\big(448+4256A^2\\ &+3864A^4+252A^6, 64+608A^2+552A^4+36A^6, 16A^2+80A^4+9A^6\big)\big],\end{aligned} \tag{3.90}$$

$$\dot{L}_N = -\frac{4(-2E)^{3/2}}{5L^4}\left(8+7A^2\right), \tag{3.91}$$

$$\dot{L}_{SO} = \frac{(-2E)^{3/2}}{15L^7}\beta\left(2264+2784A^2+297A^4, 1620+1852A^2+193A^4\right), \tag{3.92}$$

$$\begin{aligned}\dot{L}_{SS} = \frac{(-2E)^{3/2}}{20L^8}\big[&2\sigma\left(552+996A^2+132A^4, 1616+2868A^2+381A^4, 894A^2+186A^4\right)\\ &-\left(8+24A^2+3A^4\right)\tau\left(2,1,0\right)\big],\end{aligned} \tag{3.93}$$

$$\sigma(a,b,c) = \frac{1}{\nu}\left[a\boldsymbol{S}_1\cdot\boldsymbol{S}_2 - b\left(\hat{\boldsymbol{J}}\cdot\boldsymbol{S}_1\right)\left(\hat{\boldsymbol{J}}\cdot\boldsymbol{S}_2\right) + c\left|\hat{\boldsymbol{J}}\times\boldsymbol{S}_1\right|\left|\hat{\boldsymbol{J}}\times\boldsymbol{S}_2\right|\cos 2\psi\right], \tag{3.94}$$

$$\tau(a,b,c) = \sum_{i=1}^{2}\frac{1}{m_i^2}\left[a\boldsymbol{S}_i^2 - b\left(\hat{\boldsymbol{J}}\cdot\boldsymbol{S}_i\right)^2 + c\left|\hat{\boldsymbol{J}}\times\boldsymbol{S}_i\right|^2\cos 2\psi_i\right], \tag{3.95}$$

where ψ_i is the angle subtended by the projection of $\boldsymbol{S}_i$ in the plane of motion and the periastron line.

We can express these orbit averages in terms of x and e using the post-Newtonian expressions (3.77) and (3.78). Using Eqs. (3.75) and (3.76), we find the time derivatives of the mean motion and of the eccentricity:

$$\begin{aligned}\frac{dn}{dt} = \frac{\nu x^{11/2}}{(1-e^2)^{7/2}}\Bigg[&\frac{1}{5}\left(96+292e^2+37e^4\right) - \frac{x^{3/2}}{10\left(1-e^2\right)^{3/2}}\beta\big(3088+15\,528e^2+7026e^4\\ &+195e^6, 2160+11\,720e^2+5982e^4+207e^6\big) - \frac{x^2}{160\left(1-e^2\right)^2}\sigma\big(21\,952+128\,544e^2\\ &+73\,752e^4+3084e^6, 64\,576+373\,472e^2+210\,216e^4+8532e^6, 131\,344e^2+127\,888e^4\\ &+7593e^6\big) + \frac{x^2}{320\left(1-e^2\right)^2}\tau\big(448+4256e^2+3864e^4+252e^6, 64+608e^2\\ &+552e^4+36e^6, 16e^2+80e^4+9e^6\big)\Bigg],\end{aligned} \tag{3.96}$$

$$\frac{de^2}{dt} = -\frac{\nu x^4}{(1-e^2)^{5/2}}\left[\frac{2e^2}{15}\left(304+121e^2\right) - \frac{e^2x^{3/2}}{15\,(1-e^2)^{3/2}}\beta\big(13\,048+12\,000e^2+789e^4, 9208 \right.$$
$$+ 10\,026e^2+835e^4\big) - \frac{x^2}{240\,(1-e^2)^2}\sigma\big(-320+101\,664e^2+116\,568e^4+9420e^6, -320$$
$$+ 296\,672e^2+333\,624e^4+26\,820e^6, 88\,432e^2+161\,872e^4+16\,521e^6\big)$$
$$+ \frac{x^2}{480\,(1-e^2)^2}\tau\big(-320+2720e^2+5880e^4+540e^6, -320-160e^2+1560e^4+180e^6,$$
$$\left. 16e^2+80e^4+9e^6\big)\right]. \tag{3.97}$$

We find perfect agreement with [30], where the 1.5PN spin-orbit effects were computed in terms of a and e_r. One can worry that these derivatives depend on the angles ψ_i, which are not well-defined in the circular limit. This is however not a problem, as this dependence disappears in this limit both for dn/dt and de^2/dt.

We can see that the spin-spin couplings computed here induce a positive derivative de^2/dt for $e \to 0$. However, in symmetrical situations (if the projections of $\boldsymbol{S}_1/m_1$ and $\boldsymbol{S}_2/m_2$ on the orbital plane coincide), this derivative vanishes, due to the fact that $\tau(1,1,0) - \sigma(2,2,0) = (P\boldsymbol{S}_1/m_1 - P\boldsymbol{S}_2/m_2)^2$, where P is the projection operator on the orbital plane. We can compute the value of e^2 for which the derivative cancels at 2PN order, which is $e^2 = 5x^2[\tau(1,1,0) - \sigma(2,2,0)]/340$. This result does not depend on the particular quasi-Keplerian parametrization that one chooses.

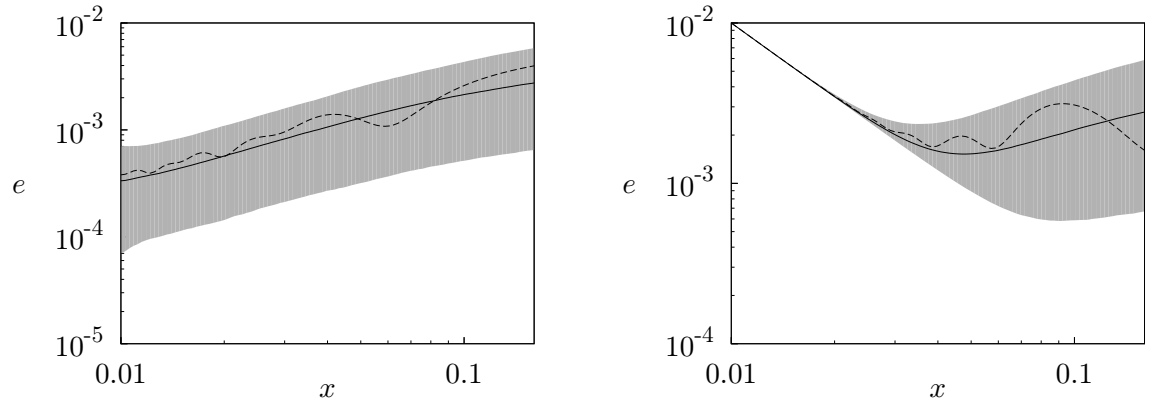

Figure 3.1: Evolution of the eccentricity between $x = 1/100$ and $x = 1/6$ with spin-orbit and spin-spin couplings, for equal-mass binaries, on the left starting from $e^2 = 5x^2[\tau(1,1,0) - \sigma(2,2,0)]/340$, and on the right from $e = 0.01$, with spins uniformly distributed. In each plot, the grey region is between the 5th and the 95th percentile, the solid line is the median, and the dashed line is a typical realization.

In Fig. 3.1, we plot the eccentricity evolution between $x = 1/100$ and $x = 1/6$ with spin-orbit and spin-spin couplings, for equal-mass binaries with spins uniformly distributed, including also the spin-independent PN corrections computed in [25], as well as spin-orbit precession [21]. We see that spin-orbit precession induces a non-trivial pattern in the eccentricity evolution, which could help to reduce the errors on spin parameters in a gravitational wave measurement. We find that the quantiles from Fig. 3.1 are very weakly dependent on the mass ratio, whereas the amplitudes of the modulations of the evolution of the eccentricity are strongly suppressed as the mass ratio decreases.

3.3.1 Circular limit

We define the circular limit of the quasi-Keplerian motion discussed above as the limit $e_t \to 0$. In this limit, we also get $e_r \to 0$ and $e_\phi \to 0$. The periastron line is not well defined, so that the equations of motion can only depend on differences of angles. We find

$$r = x^{-1} + x^{1/2}\beta(2,1) + \frac{x}{2}\gamma_1 - \frac{x}{2}\gamma_2 \cos[2(\phi - \psi)], \tag{3.98}$$

$$\frac{d\phi}{dt} = x^{3/2} - x^3\beta(4,3) - \frac{x^{7/2}}{2}\left\{3\gamma_1 + \gamma_2 \cos[2(\phi - \psi)]\right\}. \tag{3.99}$$

Note that when one includes spin-spin couplings, the orbit can no longer be circular in the sense that the radius depends explicitly on the angle along the orbit, as already mentioned in [26]. This however is not a residual eccentricity, as the radius is symmetric with respect to $\phi \to \phi + \pi$.

The angular frequency $d\phi/dt$ is not constant. However, we can use Eq. (3.71) and define its average along an orbit as

$$\begin{aligned}\omega &= \frac{n}{2\pi}\int_{t(v=-\pi)}^{t(v=\pi)} \frac{d\phi}{dt} dt \\ &= \frac{n}{2\pi}[\phi(v=\pi) - \phi(v=-\pi)] = n(1+k) \\ &= (-2E)^{3/2}\left[1 - \frac{1}{L^3}\beta(4,3) - \frac{3}{2L^4}\gamma_1\right].\end{aligned} \tag{3.100}$$

We can thus define a new post-Newtonian parameter $z = \omega^{2/3}$. In terms of this parameter, the constants E, L, and x are

$$E = -\frac{z}{2} - \frac{z^{5/2}}{3}\beta(4,3) - \frac{z^3}{2}\gamma_1, \tag{3.101}$$

$$L = z^{-1/2} - \frac{z}{6}\beta(20,15) - z^{3/2}\gamma_1, \tag{3.102}$$

$$x = z + \frac{z^{5/2}}{3}\beta(8,6) + z^3\gamma_1. \tag{3.103}$$

Now, we can use Eqs. (3.100), (3.86), and (3.87) to find

$$\frac{d\omega}{dt} = \frac{96\nu z^{11/2}}{5}\left[1 - \frac{z^{3/2}}{12}\beta(113,75) - \frac{z^2}{48}\sigma(247,721,0) + \frac{z^2}{96}\tau(7,1,0)\right], \tag{3.104}$$

which is in agreement with the evolution equations that we used in building our circular templates, which were previously computed in [27, 31].

Alternatively, if we define a circular orbit to have $de^2/dt = 0$, which implies $e^2 = 5z^2[\tau(1,1,0) - \sigma(2,2,0)]/340$, we get

$$\frac{d\omega}{dt} = \frac{96\nu z^{11/2}}{5}\left[1 - \frac{z^{3/2}}{12}\beta(113,75) - \frac{z^2}{1216}\sigma(6519,18\,527,0) + \frac{z^2}{2432}\tau(439,287,0)\right]. \tag{3.105}$$

3.4 Eccentric waveform

Now that we have found a suitable parametrization of the orbit of a binary black hole system on an eccentric orbit and evolution equations for their orbital parameters, we can apply the stationary phase approximation to the resulting gravitational wave signal. In practice, we find that it is convenient to use a post-circular expansion, inspired by [32], to perform the stationary phase approximation.

Let us recall first the evolution equations for the orbital parameters n, the (periastron-to-periastron) mean motion, and e, the time eccentricity (see Eq. (3.55)). We have computed the spin-dependent terms in the previous section, and the spin-independent terms can be found in [25, 33, 34].

$$\frac{dn}{dt} = \frac{\nu c^6 x^{11/2}}{G^2M^2\left(1-e^2\right)^{7/2}}\left(a_N + a_1\frac{x}{(1-e^2)} + a_{1.5}\frac{x^{3/2}}{(1-e^2)^{3/2}} + a_2\frac{x^2}{(1-e^2)^2}\right), \tag{3.106}$$

$$\frac{de^2}{dt} = -\frac{\nu c^3 x^4}{GM\left(1-e^2\right)^{5/2}}\left(b_N + b_1\frac{x}{(1-e^2)} + b_{1.5}\frac{x^{3/2}}{(1-e^2)^{3/2}} + b_2\frac{x^2}{(1-e^2)^2}\right), \tag{3.107}$$

where the coefficients are

$$a_N = \frac{1}{5}\left(96 + 292e^2 + 37e^4\right), \tag{3.108}$$

$$a_1 = \frac{1}{280}\big[20\,368 - 14\,784\nu + (219\,880 - 159\,600\nu)\,e^2 + (197\,022 - 141\,708\nu)\,e^4 + (11\,717 - 8288\nu)\,e^6\big], \tag{3.109}$$

$$a_{1.5} = \frac{1}{10}\big[64\pi\kappa_n - \beta\big(3088 + 15\,528e^2 + 7026e^4 + 195e^6, 2160 + 11\,720e^2 + 5982e^4 + 207e^6\big)\big], \quad (3.110)$$

$$a_2 = \frac{1}{30\,240}\Big[12\,592\,864 - 13\,677\,408\nu + 1\,903\,104\nu^2 + \big(131\,150\,624 - 217\,822\,752\nu + 61\,282\,032\nu^2\big)e^2 + \big(282\,065\,448 - 453\,224\,808\nu + 166\,506\,060\nu^2\big)e^4 + \big(112\,430\,610 - 144\,942\,210\nu + 64\,828\,848\nu^2\big)e^6 + \big(3\,523\,113 - 3\,259\,980\nu + 1\,964\,256\nu^2\big)e^8 + 3024(5-2\nu)\sqrt{1-e^2}\big(96 + 4268e^2 + 4386e^4 + 175e^6\big)\Big] - \frac{1}{160}\sigma\big(21\,952 + 128\,544e^2 + 73\,752e^4 + 3084e^6, 64\,576 + 373\,472e^2 + 210\,216e^4 + 8532e^6, 131\,344e^2 + 127\,888e^4 + 7593e^6\big) + \frac{1}{320}\tau\big(448 + 4256e^2 + 3864e^4 + 252e^6, 64 + 608e^2 + 552e^4 + 36e^6, 16e^2 + 80e^4 + 9e^6\big), \quad (3.111)$$

and

$$b_N = \frac{2e^2}{15}\left(304 + 121e^2\right), \quad (3.112)$$

$$b_1 = \frac{e^2}{1260}\big[340\,968 - 228\,704\nu + (880\,632 - 651\,252\nu)\,e^2 + (125\,361 - 93\,184\nu)\,e^4\big], \quad (3.113)$$

$$b_{1.5} = \frac{e^2}{15}\left[64\pi\kappa_e - \beta\left(13\,048 + 12\,000e^2 + 789e^4, 9208 + 10\,026e^2 + 835e^4\right)\right], \quad (3.114)$$

$$b_2 = \frac{e^2}{15\,120}\Big[20\,621\,680 - 28\,665\,360\nu + 4\,548\,096\nu^2 + \big(86\,398\,044 - 148\,804\,812\nu + 48\,711\,348\nu^2\big)e^2 + \big(69\,781\,286 - 95\,827\,362\nu + 42\,810\,096\nu^2\big)e^4 + \big(3\,786\,543 - 4\,344\,852\nu + 2\,758\,560\nu^2\big)e^6 + 1008(5-2\nu)\sqrt{1-e^2}\big(2672 + 6963e^2 + 565e^4\big)\Big] + \frac{1}{240}\sigma\big(320 - 101\,664e^2 - 116\,568e^4 - 9420e^6, 320 - 296\,672e^2 - 333\,624e^4 - 26\,820e^6, -88\,432e^2 - 161\,872e^4 - 16\,521e^6\big) - \frac{1}{480}\tau\big(320 - 2720e^2 - 5880e^4 - 540e^6, 320 + 160e^2 - 1560e^4 - 180e^6, -16e^2 - 80e^4 - 9e^6\big). \quad (3.115)$$

The two functions κ_n and κ_e are defined through

$$\kappa_n = \left(1-e^2\right)^5 \sum_{p\geq 1} p^3\big\{J_p(pe)^2\left[3e^{-4} - 3e^{-2} + 1 + p^2\left(3e^{-4} - 9e^{-2} + 9 - 3e^2\right)\right] - pJ_p(pe)J_p'(pe)\left[12e^{-3} - 21e^{-1} + 9e\right] + J_p'(pe)^2\left[3e^{-2} - 3 + p^2\left(3e^{-2} - 6 + 3e^2\right)\right]\big\}, \quad (3.116)$$

$$\kappa_e = \left(1-e^2\right)^5 \sum_{p\geq 1} p^2 \big\{ pJ_p(pe)^2 \left[15e^{-6} - 21e^{-4} + 7e^{-2} + p^2\left(3e^{-6} - 9e^{-4} + 9e^{-2} - 3\right)\right] \\ - J_p(pe)J'_p(pe)\left[12e^{-5} - 6e^{-3} + p^2\left(24e^{-5} - 45e^{-3} + 21e^{-1}\right)\right] \\ + pJ'_p(pe)^2\left[15e^{-4} - 15e^{-2} + p^2\left(3e^{-4} - 6e^{-2} + 3\right)\right]\big\}. \tag{3.117}$$

Both are even functions of e that tend to a non-zero constant value when $e \to 0$, so that we can compute the coefficients of their Taylor expansion up to the accuracy needed.

We can solve equations (3.106) and (3.107) numerically, and get

$$n(t) = n_0 + \int_{t_0}^{t} \frac{dn}{dt} dt, \tag{3.118}$$

$$e^2(t) = e_0^2 + \int_{t_0}^{t} \frac{de^2}{dt} dt. \tag{3.119}$$

The mean anomaly l is given by

$$l(t) = l_0 + \int_{t_0}^{t} n dt. \tag{3.120}$$

The polar angle along the orbit ϕ is separated into a "lineraly increasing" mean phase λ and a "periodic" part W, as $\phi = \lambda + W$. λ is

$$\lambda(t) = \lambda_0 + \int_{t_0}^{t} (1+k) n dt, \tag{3.121}$$

$$k = \frac{3x}{1-e^2} - \frac{x^{3/2}}{(1-e^2)^{3/2}}\beta(4,3) + \frac{x^2}{4(1-e^2)^2}\left[78 - 28\nu + (51-26\nu)e^2 - \sigma(6,18,0)\right]. \tag{3.122}$$

The eccentric and true anomalies u and v are given by (without spin effects) [25]

$$l = u - e\sin u - \frac{x^2}{8\sqrt{1-e^2}}\left[e\left(4\nu + \nu^2\right)\sin v + 12(5-2\nu)(u-v)\right], \tag{3.123}$$

$$v = 2\arctan\left(\sqrt{\frac{1+e_\phi}{1-e_\phi}}\tan\frac{u}{2}\right), \tag{3.124}$$

$$e_\phi = e\Bigg\{1 + x(4-\nu) + \frac{x^2}{96\left(1-e^2\right)}\Big[1968 - 1088\nu - 4\nu^2 \\ - \left(1152 - 656\nu + 41\nu^2\right)e^2 + (720 - 288\nu)\sqrt{1-e^2}\Big]\Bigg\}. \tag{3.125}$$

The wave polarisations h_+ and $h_\times$ are given as a series of harmonics of ϕ [35]:

$$h_{+,\times} = \frac{GM\nu x}{d_L c^2}\sum_{p\geq 0}\left(A^{(p)}_{+,\times}\cos p\phi + B^{(p)}_{+,\times}\sin p\phi\right), \tag{3.126}$$

where $A^{(p)}_{+,\times}$ and $B^{(p)}_{+,\times}$ are functions of u. The phase $\phi = \lambda + W$ is defined with respect to the "principal+ direction", defined as the direction of $\hat{\boldsymbol{L}} \times \hat{\boldsymbol{N}}$.

To compute the Fourier transform of this wave in the stationary phase approximation, we transform the dependence on u and W to a dependence on l, which we can consider as linearly increasing in an adiabatic approximation, i.e. when neglecting the energy and angular momentum loss of the system.

We first note that the functions u and v, being periodic functions of l, can be expressed as a Fourier series:

$$u = l + \sum_{p\geq 1} u_p \sin pl, \tag{3.127}$$

$$v = l + \sum_{p\geq 1} v_p \sin pl. \tag{3.128}$$

where we used the fact that both are odd functions of l, and where

$$u_p = \frac{1}{\pi}\int_{-\pi}^{\pi} (u-l)\sin pl dl, \tag{3.129}$$

$$v_p = \frac{1}{\pi}\int_{-\pi}^{\pi} (v-l)\sin pl dl. \tag{3.130}$$

With these definitions, we can write $W(l)$ [25]:

$$W = (1+k)(v-l) + \frac{x^2}{8}\frac{e^2\left(\nu - 3\nu^2\right)\sin 2v}{\left(1-e^2\right)^2} - \frac{3x^2}{32}\frac{e^3\nu^2\sin 3v}{\left(1-e^2\right)^2}, \tag{3.131}$$

which can also be expressed as a Fourier series in l:

$$W = \sum_{p\geq 1} W_p \sin pl, \tag{3.132}$$

with W_p defined similarly to u_p and v_p.

In practice, as W is a complicated function of x and e, we can first perform an expansion of W in x and e, and then compute each expansion coefficient separately. The same reasoning can be applied to u.

The Fourier decomposition of functions of l allows us to transform the gravitational wave signal as

$$\begin{aligned}
&\sum_{p\geq 0}\left(A^{(p)}_{+,\times}\cos p\phi + B^{(p)}_{+,\times}\sin p\phi\right)\\
&= \sum_{p\geq 0}\left[\left(A^{(p)}_{+,\times}\cos pW + B^{(p)}_{+,\times}\sin pW\right)\cos p\lambda + \left(B^{(p)}_{+,\times}\cos pW - A^{(p)}_{+,\times}\sin pW\right)\sin p\lambda\right]\\
&= \sum_{p,q\geq 0}\left[\left(a^{+,\times}_{p,q}\cos ql + b^{+,\times}_{p,q}\sin ql\right)\cos p\lambda + \left(c^{+,\times}_{p,q}\cos ql + d^{+,\times}_{p,q}\sin ql\right)\sin p\lambda\right],
\end{aligned} \tag{3.133}$$

where $a^{+,\times}_{p,q}$, $b^{+,\times}_{p,q}$, $c^{+,\times}_{p,q}$, and $d^{+,\times}_{p,q}$ are given as series in e and x.

Using the spin-orbit precession equations together with Eqs. (3.118-3.121), one can solve for $n(t)$, $e(t)$, $l(t)$, $\lambda(t)$, $\hat{\boldsymbol{L}}(t)$, and $\boldsymbol{S}_i(t)$ using suitable initial conditions.

We can point out that since the mean anomaly l is defined with respect to the periastron line fixed to the orbital plane, it is not corrected by spin-induced precession effects. However, the mean phase receives the correction

$$\delta\lambda = \int_{t_0}^{t} \frac{\hat{\boldsymbol{L}}\cdot\hat{\boldsymbol{N}}}{1-\left(\hat{\boldsymbol{L}}\cdot\hat{\boldsymbol{N}}\right)^2}\left(\hat{\boldsymbol{L}}\times\hat{\boldsymbol{N}}\right)\dot{\hat{\boldsymbol{L}}}dt. \tag{3.134}$$

As for the Doppler phase induced by the motion of LISA around the Sun, it applies to both phases, as

$$\delta l_D = \frac{nR}{c}\sin\bar{\theta}_N\cos(\bar{\Phi}-\bar{\phi}_N), \tag{3.135}$$

$$\delta\lambda_D = (1+k)\delta l_D. \tag{3.136}$$

3.4.1 Stationary phase approximation

To use matched filtering, as used in gravitational wave detectors, one needs the Fourier transform of the signal

$$\tilde{h}(f) = \int h(t)e^{2\pi i f t}dt. \tag{3.137}$$

We can transform the signal $h(t)$ in each detector using (3.126), (3.133), and (2.27) as follows:

$$h(t) = \sum_{p,q\geq 0} h_{p,q}(t), \tag{3.138}$$

$$h_{p,q}(t) = A_{p,q}e^{i(p\lambda+ql)} + B_{p,q}e^{i(p\lambda-ql)} + C_{p,q}e^{-i(p\lambda-ql)} + D_{p,q}e^{-i(p\lambda+ql)}, \tag{3.139}$$

$$A_{p,q} = \frac{1}{4}[a_{p,q} - d_{p,q} - i(b_{p,q}+c_{p,q})], \tag{3.140}$$

$$B_{p,q} = \frac{1}{4}[a_{p,q} + d_{p,q} + i(b_{p,q}-c_{p,q})], \tag{3.141}$$

$$C_{p,q} = \frac{1}{4}[a_{p,q} + d_{p,q} - i(b_{p,q}-c_{p,q})], \tag{3.142}$$

$$D_{p,q} = \frac{1}{4}[a_{p,q} - d_{p,q} + i(b_{p,q}+c_{p,q})], \tag{3.143}$$

where $a_{p,q}$, $b_{p,q}$, $c_{p,q}$, and $d_{p,q}$ are slowly varying functions of time, given as an expansion in e and x, and that also depend on ν, $\hat{\boldsymbol{L}}$, and $\hat{\boldsymbol{N}}$, from Eq. (3.133). The structure of the post-Newtonian expansion is such that if we choose to compute these coefficients at 2PN order, we only have to consider $p \leq 6$, and if we choose to stop the expansion in the eccentricity at order e^n, we only have to consider $q \leq n$. Note that we can neglect spin

effects in the determination of those functions, if we choose to take them into account only in the phase.

We can rewrite the Fourier transform of the signal as

$$\tilde{h}(f) = \sum_{p,q\geq 0} \int \Big[A_{p,q} e^{i(2\pi f t + p\lambda + ql)} + B_{p,q} e^{i(2\pi f t + p\lambda - ql)} + C_{p,q} e^{i(2\pi f t - p\lambda + ql)} + D_{p,q} e^{i(2\pi f t - p\lambda - ql)} \Big] dt. \tag{3.144}$$

The stationary phase approximation consists of considering the Fourier integral to be dominated by portions where the phase is stationary, i.e.

$$\frac{d}{dt}(2\pi f t \pm p\lambda \pm ql) = 0 \quad \Rightarrow \quad 2\pi f = \pm n[p(1+k) \pm q], \tag{3.145}$$

where $dl/dt = n$ (3.120), and $d\lambda/dt = (1+k)n$ (3.121).

As we consider only positive frequencies, we can discard the contribution of the terms that lead to negative frequencies. Thus, we have different contributions:

$$2\pi f = n[p(1+k) + q], \tag{3.146}$$
$$2\pi f = n\,|p(1+k) - q|\,. \tag{3.147}$$

For a given couple (p,q), the Fourier transform then becomes

$$\tilde{h}(f) = H_1(t_1) + H_2(t_2) + H_3(t_3), \tag{3.148}$$
$$H_1(t) = D_{p,q}\sqrt{\frac{2\pi}{|p\partial_t^2\lambda + q\partial_t^2 l|}}\exp\big\{i\big[2\pi f t - p\lambda - ql - \frac{\pi}{4}\big]\big\}, \tag{3.149}$$
$$H_2(t) = C_{p,q}\sqrt{\frac{2\pi}{|p\partial_t^2\lambda - q\partial_t^2 l|}}\exp\big\{i\big[2\pi f t - p\lambda + ql - \mathrm{sign}\big(p\partial_t^2\lambda - q\partial_t^2 l\big)\frac{\pi}{4}\big]\big\}, \tag{3.150}$$
$$H_3(t) = B_{p,q}\sqrt{\frac{2\pi}{|q\partial_t^2 l - p\partial_t^2\lambda|}}\exp\big\{i\big[2\pi f t + p\lambda - ql - \mathrm{sign}\big(q\partial_t^2 l - p\partial_t^2\lambda\big)\frac{\pi}{4}\big]\big\}, \tag{3.151}$$
$$f = \frac{n(t_1)}{2\pi}\left\{p[1+k(t_1)] + q\right\}, \tag{3.152}$$
$$f = \frac{n(t_2)}{2\pi}\left\{p[1+k(t_2)] - q\right\}, \tag{3.153}$$
$$f = \frac{n(t_3)}{2\pi}\left\{q - p[1+k(t_3)]\right\}. \tag{3.154}$$

As we do not have an analytic expression for $n(t)$ and $k(t)$, we cannot invert the relations above to find $t_i(f)$, but must invert these numerically. The final Fourier transform is then found adding the terms coming from all different couples (p,q), taking into acount the fact that for a given (f,p,q) there may be several solutions to (3.153) and (3.154). We note at

this point that terms with phase $p\lambda - ql$, for $p = q$, contribute to frequencies well separated from the others, as k is a 1PN quantity. We can therefore neglect them.

The second time derivative of l is given by $\partial_t^2 l = dn/dt$ in (3.106), and that of λ is given at 2PN order by

$$\partial_t^2 \lambda = \frac{d}{dt}\left[n(1+k)\right] = \frac{dn}{dt} + \frac{\nu c^6 x^{11/2}}{G^2 M^2 \left(1-e^2\right)^{7/2}} \left(c_1 x + c_{1.5} x^{3/2} + c_2 x^2\right), \tag{3.155}$$

where

$$c_1 = \frac{3}{5\left(1-e^2\right)} \left(160 + 284e^2 - 19e^4\right), \tag{3.156}$$

$$c_{1.5} = -\frac{1}{5\left(1-e^2\right)^{3/2}} \left(192 + 280e^2 - 47e^4\right) \beta(4,3), \tag{3.157}$$

$$\begin{aligned} c_2 = \frac{1}{280\left(1-e^2\right)^2} \big[&346\,448 - 161\,728\nu + (1\,188\,712 - 761\,488\nu)e^2 \\ &+ (600\,294 - 389\,844\nu)e^4 - (20\,943 - 18\,620\nu)e^6 \\ &- \sigma\big(18\,816 + 23\,184e^2 - 6300e^4, 56\,448 + 69\,552e^2 - 18\,900e^4\big)\big]. \end{aligned} \tag{3.158}$$

If $q > p$, the function $q\partial_t^2 l - p\partial_t^2 \lambda$ reaches zero during the inspiral. This is clearly a problem for the stationary phase approximation. In practice, we found that the function $q\partial_t^2 l - p\partial_t^2 \lambda$ using (3.155) crosses zero after $q\partial_t^2 l - p\partial_t^2 \lambda$ using (3.120) and (3.121) does, and that it is a good prescription to use (3.155) to compute $|p\partial_t^2 \lambda \pm q\partial_t^2 l|^{-1/2}$ until $p\partial_t^2 \lambda \pm q\partial_t^2 l$ reaches zero, and to use $(|p \pm q| dn/dt)^{-1/2}$ after it does. We show the comparison between the norm of our approximation with the norm of the Fourier transform obtained numerically for a given (p, q) for which $q\partial_t^2 l - p\partial_t^2 \lambda$ reaches zero during the inspiral, with a simplified amplitude and for a typical system in Fig. 3.2. We use $p = 6$, $q = 8$, $A_{6,8} = D_{6,8} = 0$, $B_{6,8} = C_{6,8} = 1/2$ in (3.139), and $t_c = 3$ years, defined as the time when $(GM\partial_t \lambda/c^3)^{2/3} = 1/6$. We also show the comparison between the time series for the same system and the time series reconstructed with our approximation in Fig. 3.3. In these figures, we use black holes with zero spin, to show the validity of our prescription for the amplitude of the Fourier transform. We put a cutoff in our waveform at 10^{-5} Hz. When we add spin effects, the phase of the reconstructed time domain signal is as good as it is without them. However, the small modulation of the phase induces a large modulation of the amplitude of the Fourier transform, which the stationary phase approximation is unable to reproduce.

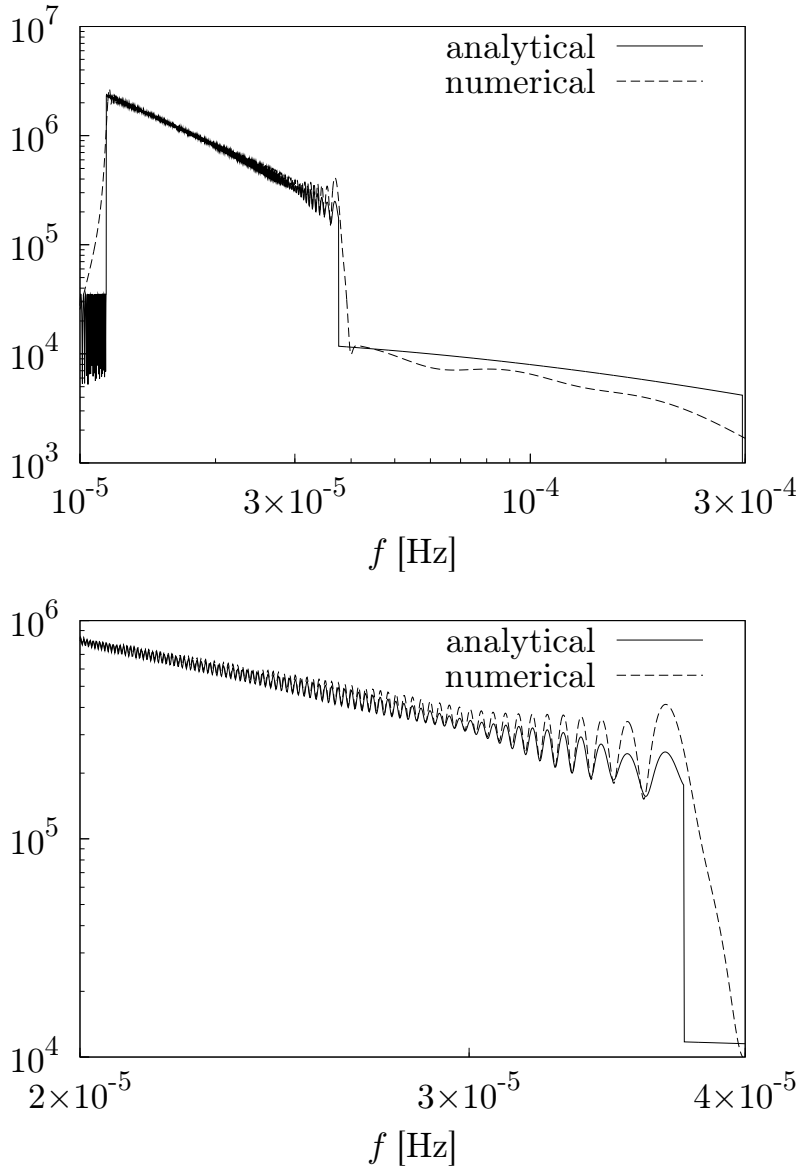

Figure 3.2: Amplitude of the Fourier transform of a fiducial gravitational wave signal, using a discrete Fourier transform and our approximation. The plot below is a zoom of the one above. As the stationary phase approximation does not well reproduce modulations due to the spins in the amplitude, we set the spins of both black holes to zero. The signal shown here was built with the phase of a gravitational wave signal, and with a constant amplitude.

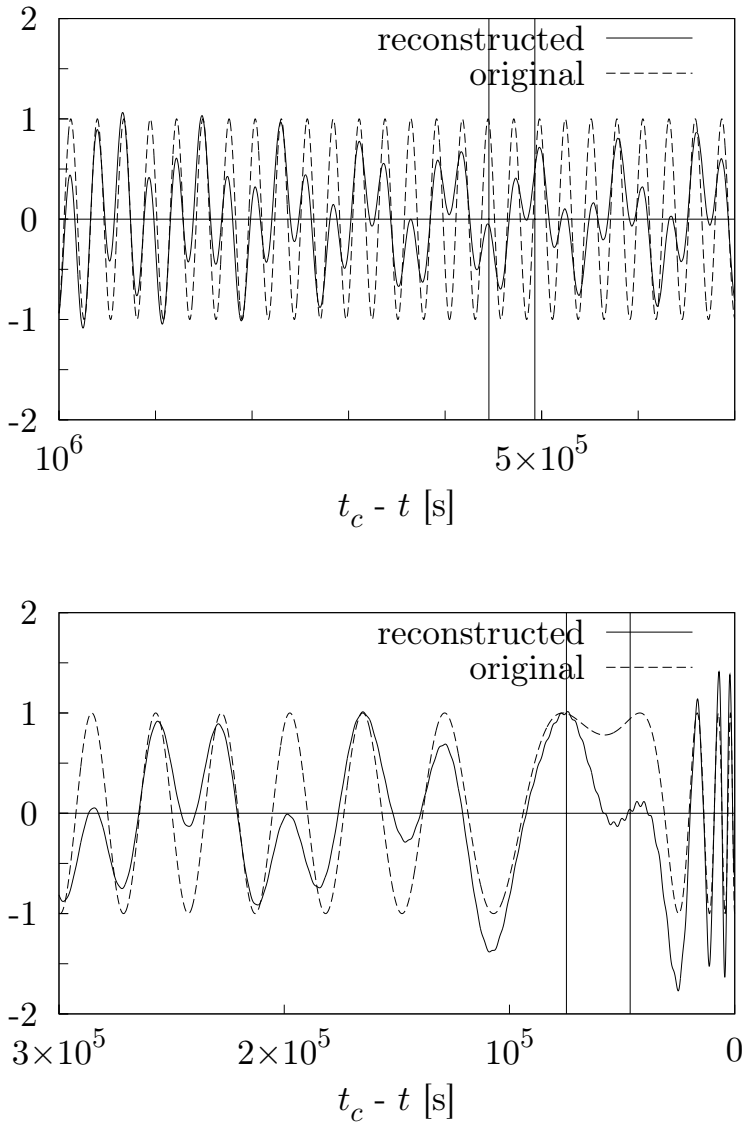

Figure 3.3: We plot here the original time signal with simplified amplitude together with a reconstructed time signal obtained by inverting the Fourier transform from our approximation. We plot only the end of the signal, where the derivative of the frequency changes sign, at $t \approx t_c - 5.3 \times 10^5$ s, and where $n[p(1+k)-q]$ changes sign, at $t \approx t_c - 6 \times 10^4$ s. The vertical lines indicate portions of the signal with a constant sign for $n[p(1+k)-q]$, and with a constant sign for its derivative. The signal we inverted is the same as that shown in Fig. 3.2. We can see that, although the amplitude is subject to oscillations due to the cutoffs we used in the Fourier domain, the phase is well recovered. During the whole inspiral, before $t = t_c - 10^6$ s, the phase is recovered far better, and we do not show it here.

Chapter 4

Full circular waveform

In this chapter, we present a set of simulations which we ran using the circular templates described in Section 3.2, the result of which we published in [36]. The purpose of this study was to compare the parameter estimation capabilities of the RWF, the SWF and the FWF described there. All of these waveforms include spin-orbit precession, but the RWF does not include subdominant harmonics ($n \neq 2$). The SWF includes them, but with a simplified version of their amplitude.

4.1 Simulations

As a set of 12 intrinsic plus 3 extrinsic parameters for our simulations, we used:

- $\log_{10} m_1/M_\odot$ and $\log_{10} m_2/M_\odot$, for the masses of the two black holes.

- $\mu_l = \cos\theta_l$ and ϕ_l, for the spherical angles of the orbital angular momentum $\boldsymbol{L}$ at an orbital separation $r = \frac{6GM}{c^2}$.

- $\mu_1 = \cos\theta_1$ and ϕ_1 for the spherical angles of the spin of the first black hole $\boldsymbol{S}_1$ at an orbital separation $r = \frac{6GM}{c^2}$.

- $\chi_1 = \frac{c}{Gm_1^2}|\boldsymbol{S}_1|$ for the dimensionless strength of the spin of the first black hole, which has to satisfy $0 \leqslant \chi_1 < 1$.

- $\mu_2 = \cos\theta_2$, ϕ_2, and χ_2, same for the second black hole as for the first one.

- t_c, the time of coalescence.

- φ_c, the phase at coalescence. As this phase is random and its determination is not of any astrophysical interest, we can safely neglect constants in the orbital phase, in particular the constant of integration in Eq. (3.9).

- $\mu_N = \cos\theta_N$ and ϕ_N, the spherical angles of the position of the binary in the sky.

- d_L, the luminosity distance between the source and the Solar System.

All angles are taken in the frame tied to the distant stars. We fix the zero point of time by the beginning of the LISA mission.

We performed Monte Carlo simulations in which, given a set of parameters, we evolved the binary backwards in frequency starting from $\omega(r = 6GM/c^2)$ using a fourth order adaptive Runge-Kutta algorithm to find $\hat{\boldsymbol{L}}(\omega)$, $\boldsymbol{S}_1(\omega)$, $\boldsymbol{S}_2(\omega)$, and $\delta\varphi(\omega)$. We stopped the simulations either at $t = 0$, or when the frequency of the highest harmonic had dropped below the LISA band, for $6\omega < 3 \times 10^{-5}$ Hz. We chose to start at $r = 6GM/c^2$ because it is the radius of the innermost stable circular orbit (ISCO) for a Schwartzschild black hole. Of course, when dealing with a spinning black hole, the radius of the ISCO can vary between $r = GM/c^2$ and $r = 9GM/c^2$, depending on the spin parameter of the black hole and on the orientation of the orbit, but the series may not converge when $\gamma = GM/rc^2$ is close to 1, so that we chose to consider the post-Newtonian expansion as accurate for $\gamma \leq 1/6$, which seems to be a good enough prescription [37, 38].

We then put these functions inside the Fourier transforms of the waves (3.38).

Five derivatives $\partial_{\theta^i}\tilde{h}_k$ out of the 15 needed can be found analytically. Three simple ones are:

$$\frac{\partial\tilde{h}_k(\theta^j, f)}{\partial t_c} = 2\pi i f \tilde{h}_k(\theta^j, f), \tag{4.1}$$

$$\frac{\partial\tilde{h}_k(\theta^j, f)}{\partial d_L} = -\frac{\tilde{h}_k(\theta^j, f)}{d_L}, \tag{4.2}$$

$$\frac{\partial\tilde{h}_k(\theta^j, f)}{\partial \varphi_c} = -i\sum_n n\tilde{h}_{k,n}(\theta^j, f), \tag{4.3}$$

where $\tilde{h}_{k,n}$ is the n-th harmonic component of $\tilde{h}_k$. The other two are the derivatives with respect to μ_n and ϕ_n. The only quantities in Eq. (3.38) that depend on these parameters are $A^{pol}_{k,n}$, $\phi^{pol}_{k,n}$, $\delta\varphi$, and ϕ_D.

The derivatives which we could not find analytically have been computed numerically using the relation

$$\frac{\partial\tilde{h}_k(\theta^j, f)}{\partial\theta^i} \approx \frac{\tilde{h}_k(\theta^j + \epsilon\delta^{ij}/2, f) - \tilde{h}_k(\theta^j - \epsilon\delta^{ij}/2, f)}{\epsilon}, \tag{4.4}$$

where ϵ is a small displacement of the parameter θ^i. We used a constant value of $\epsilon = 10^{-7}$ for every parameter, except for ϕ_l for which ϵ was divided by $2 - 2|\mu_l|$, μ_i ($i \in \{1, 2\}$) for which ϵ was divided by $5\chi_i$, and ϕ_i for which ϵ was divided by $10\chi_i(1 - |\mu_i|)$. The formula is accurate up to $O(\epsilon^2)$.

We computed the functions $\hat{\boldsymbol{L}}(\omega)$, $\boldsymbol{S}_1(\omega)$, $\boldsymbol{S}_2(\omega)$, and $\delta\varphi(\omega)$ for each displacement of the parameters.

We then evaluated numerically the integrals $(\partial_{\theta^i}\tilde{h}_k|\partial_{\theta^j}\tilde{h}_k)$ to find the Fisher information matrix. Each harmonic $\tilde{h}_{k,n}(f)$ is truncated if necessary to remain inside the LISA band, which we take to be $[3 \cdot 10^{-5}, 1]$ Hz.

We added the contributions from both detectors, and then inverted the matrix numerically to find the statistical error estimates.

We found that in some extreme situations, when $\hat{\boldsymbol{L}}\cdot\hat{\boldsymbol{N}}$ gets close to 1, the Runge-Kutta method fails to converge when computing $\delta\varphi$, because

$$\frac{d\delta\varphi}{d\omega} = \frac{\hat{\boldsymbol{L}}\cdot\hat{\boldsymbol{N}}}{1-\left(\hat{\boldsymbol{L}}\cdot\hat{\boldsymbol{N}}\right)^2}\left(\hat{\boldsymbol{L}}\times\hat{\boldsymbol{N}}\right)\cdot\frac{d\hat{\boldsymbol{L}}}{d\omega} \sim \frac{1}{\left|\hat{\boldsymbol{L}}\times\hat{\boldsymbol{N}}\right|},\ \hat{\boldsymbol{L}}\cdot\hat{\boldsymbol{N}}\to 1. \tag{4.5}$$

For this reason, we chose to compute $\delta\varphi(\omega)$ whenever $\hat{\boldsymbol{L}}\cdot\hat{\boldsymbol{N}}$ is to close to 1 with an approximate value, which is

$$\delta\varphi(\omega+\delta\omega) \approx \delta\varphi(\omega) + \text{angle}\left[\left(\hat{\boldsymbol{L}}(\omega+\delta\omega)\times\hat{\boldsymbol{N}}\right),\left(\hat{\boldsymbol{L}}(\omega)\times\hat{\boldsymbol{N}}\right)\right]. \tag{4.6}$$

We ran different sets of simulations fixing the redshift and the masses, and selected the other parameters randomly, using a flat distribution. The bounds to put on the Monte Carlo selection of the different parameters are clear, except for t_c. We chose the following bounds, consistently with [6]: the lower bound for t_c is for the physical separation parameter γ to be equal to 1/6 at $t=0$ (combining Eqs. (3.10) and (3.16)), and the upper bound is $t_c = 3$ yrs (this is in fact the minimum science requirement of the mission), which we take to be the duration of the LISA mission, so that the coalescence is visible during it. We computed for each set the mean measurement errors for the parameters and signal-to-noise ratio (SNR), comparing the output for the RWF, the SWF, and the FWF defined at the end of section 3.2.

4.2 Results

We ran different sets of simulations, each of them at a redshift of $z=1$, varying the masses between $O(10^5 M_\odot)$ and $O(10^8 M_\odot)$, and the mass ratio between 1:1 and 1:10. We did not vary the redshift, because, as described in chapter 3, it cannot be measured by a gravitational wave experiment. Furthermore, with the redshift-to-luminosity distance relationship fixed, the only parameter varying with the redshift for constant redshifted masses is the luminosity distance. The statistical errors in this case scale for all parameters as $(1+z)d_L$, as this parameter appears only as an overall factor in the waveforms. For example, the statistical error estimates on the parameters for a system with $m_1 = 5\times 10^6 M_\odot$, $m_2 = 5\times 10^5 M_\odot$, and $z=1$ are exactly the same as those for a system with $m_1 = 2\times 10^6 M_\odot$, $m_2 = 2\times 10^5 M_\odot$, and $z=4$ (same redshifted masses), multiplied by $2.5 d_L(z=4)/d_L(z=1)$. For binaries with masses higher than $10^7 M_\odot$, the results for the RWF cannot be trusted, as the second harmonic spends typically only a few orbits inside the LISA band, and no signal at all can be observed for $10^8 M_\odot$ binaries. Each of our sets of simulations consisted of over a thousand binaries. We performed *a posteriori* statistical checks showing that the medians should be correctly estimated up to a few percent.

The following tables contain a best-case measurement error (5% quantile), a typical error (the median), and a worst-case error (95% quantile) for all samples and parameter values of interest. The parameters we are interested in are the (redshifted) individual masses of the black holes, shown in Tables 4.1 and 4.2; their spin parameters, shown in Tables 4.3 and 4.4; the principal axes of the localization ellipse in the sky, shown in Tables 4.5 and 4.6; and the (redshifted) luminosity distance to the source, shown in Table 4.7.

We follow [6] to present as sky localization parameters the principal axes $2a$ and $2b$ of the ellipse enclosing the region outside of which there is a $1/e$ probability of finding the binary.

For binaries for which no signal can be extracted from the data, we fix the errors to infinity. For apparently meaningless errors, such as $\Delta d_L/d_L > 1$ or $2a > 2\pi$, we still provide the error as computed, because it can give an indication as the limit to what redshift quantities can be computed using the scaling property of the error with respect to $(1+z)d_L$.

We find that the binaries can be roughly separated into three classes: low unequal-mass binaries, low equal-mass binaries ($M \lesssim 10^7 M_\odot$), and high-mass binaries ($M \gtrsim 10^7 M_\odot$). We discuss below these three distinct cases, and plot the estimated error distributions for a representative sample of each one of the three classes for the parameters $\Delta m_1/m_1$, $\Delta\chi_1$, $2a$, and $\Delta d_L/d_L$. The distributions for $\Delta m_2/m_2$ are similar to those for $\Delta m_1/m_1$, those for $\Delta\chi_2$ to those for $\Delta\chi_1$, and those for $2b$ to those for $2a$.

In general, for lower-mass binaries and independently of the mass ratio, we find that the errors expected for extrinsic parameters using the FWF are ~ 1.5 times the ones expected for the RWF. This factor is ~ 1.2 comparing the SWF to the RWF. This is changed when considering higher-mass binaries, because the second harmonic, the only one present in the RWF, spends very few cycles inside the LISA band.

To discuss the mass limit above which no information can be extracted from a system, we shall present the proportion of systems for which the individual masses and the luminosity distance can be measured with 50% and 25% accuracy, for all samples. We also plot the maximum redshift at which information can be extracted from a binary system, as a function of m_1, for different mass ratios.

We shall then present how far the measurement of supermassive black hole mergers could help determining the Hubble diagram for each waveform. To do so, we compute up to what redshift half of the systems can be localized inside the field of view of Hubble and/or XMM-Newton (see e.g. [39]) which we take to be $30'$ wide, with an error on d_L less than 10%.

4.2.1 Low unequal-mass binaries

In this class, we place all systems with total mass smaller than $10^7 M_\odot$, and with a mass ratio of at least 1:3. As a representative sample, we choose to present systems with $m_1 = 10^6 M_\odot$ and $m_2 = 3 \cdot 10^5 M_\odot$. We plot the estimated distribution of the errors on m_1 in Fig. 4.1, on χ_1 in Fig. 4.2, on the sky positioning in Fig. 4.3, and on d_L in Fig. 4.4.

$m_1[M_\odot]$	$m_2[M_\odot]$	$\Delta m_1/m_1$								
		5% quantile			Median			95% quantile		
		RWF	SWF	FWF	RWF	SWF	FWF	RWF	SWF	FWF
$3 \cdot 10^5$	10^5	$1.85 \cdot 10^{-4}$	$1.69 \cdot 10^{-4}$	$1.44 \cdot 10^{-4}$	$8.06 \cdot 10^{-4}$	$6.71 \cdot 10^{-4}$	$4.76 \cdot 10^{-4}$	$8.17 \cdot 10^{-3}$	$2.54 \cdot 10^{-3}$	$1.58 \cdot 10^{-3}$
10^6	10^5	$2.44 \cdot 10^{-4}$	$1.99 \cdot 10^{-4}$	$1.63 \cdot 10^{-4}$	$7.13 \cdot 10^{-4}$	$5.36 \cdot 10^{-4}$	$4.25 \cdot 10^{-4}$	$4.63 \cdot 10^{-3}$	$2.82 \cdot 10^{-3}$	$2.13 \cdot 10^{-3}$
10^6	$3 \cdot 10^5$	$4.08 \cdot 10^{-4}$	$3.59 \cdot 10^{-4}$	$2.90 \cdot 10^{-4}$	$1.36 \cdot 10^{-3}$	$1.10 \cdot 10^{-3}$	$8.01 \cdot 10^{-4}$	$1.11 \cdot 10^{-2}$	$3.95 \cdot 10^{-3}$	$2.60 \cdot 10^{-3}$
$3 \cdot 10^5$	$3 \cdot 10^5$	$1.69 \cdot 10^{-4}$	$1.62 \cdot 10^{-4}$	$1.19 \cdot 10^{-4}$	$1.24 \cdot 10^{-3}$	$1.17 \cdot 10^{-3}$	$2.91 \cdot 10^{-4}$	$1.14 \cdot 10^{-2}$	$8.82 \cdot 10^{-3}$	$6.52 \cdot 10^{-4}$
10^6	10^6	$3.59 \cdot 10^{-4}$	$3.53 \cdot 10^{-4}$	$2.53 \cdot 10^{-4}$	$2.48 \cdot 10^{-3}$	$2.42 \cdot 10^{-3}$	$7.16 \cdot 10^{-4}$	$2.98 \cdot 10^{-2}$	$2.29 \cdot 10^{-2}$	$1.57 \cdot 10^{-3}$
10^7	10^6	$1.21 \cdot 10^{-3}$	$7.93 \cdot 10^{-4}$	$4.46 \cdot 10^{-4}$	$4.34 \cdot 10^{-3}$	$2.49 \cdot 10^{-3}$	$1.37 \cdot 10^{-3}$	$4.21 \cdot 10^{-2}$	$1.12 \cdot 10^{-2}$	$5.09 \cdot 10^{-3}$
10^7	$3 \cdot 10^6$	$3.39 \cdot 10^{-3}$	$1.89 \cdot 10^{-3}$	$8.23 \cdot 10^{-4}$	$1.59 \cdot 10^{-2}$	$4.26 \cdot 10^{-3}$	$1.79 \cdot 10^{-3}$	0.140	$1.18 \cdot 10^{-2}$	$5.86 \cdot 10^{-3}$
10^7	10^7	$2.20 \cdot 10^{-2}$	$1.21 \cdot 10^{-2}$	$2.04 \cdot 10^{-3}$	0.213	$8.97 \cdot 10^{-2}$	$5.79 \cdot 10^{-3}$	1.47	0.825	$1.57 \cdot 10^{-2}$
$3 \cdot 10^7$	10^7	0.377	$8.64 \cdot 10^{-3}$	$4.35 \cdot 10^{-3}$	1.01	$1.99 \cdot 10^{-2}$	$9.48 \cdot 10^{-3}$	3.23	$5.35 \cdot 10^{-2}$	$2.43 \cdot 10^{-2}$
$3 \cdot 10^7$	$3 \cdot 10^7$	3.74	0.525	$5.55 \cdot 10^{-2}$	23.1	2.26	0.120	115	9.05	0.386
10^8	10^7	∞	$9.67 \cdot 10^{-2}$	$9.45 \cdot 10^{-2}$	∞	0.276	0.246	∞	1.27	1.00
10^8	$3 \cdot 10^7$	∞	0.896	0.963	∞	2.57	2.86	∞	53.6	59.7

Table 4.1: Median, 5% and 95% quantiles of the estimated measurement errors on m_1 for different sets of binaries located at redshift $z = 1$, with low unequal-mass binaries above, low equal-mass binaries in the middle, and high-mass binaries below.

$m_1[M_\odot]$	$m_2[M_\odot]$	$\Delta m_2/m_2$								
		5% quantile			Median			95% quantile		
		RWF	SWF	FWF	RWF	SWF	FWF	RWF	SWF	FWF
$3 \cdot 10^5$	10^5	$1.50 \cdot 10^{-4}$	$1.37 \cdot 10^{-4}$	$1.18 \cdot 10^{-4}$	$6.54 \cdot 10^{-4}$	$5.44 \cdot 10^{-4}$	$3.87 \cdot 10^{-4}$	$6.64 \cdot 10^{-3}$	$2.06 \cdot 10^{-3}$	$1.28 \cdot 10^{-3}$
10^6	10^5	$1.76 \cdot 10^{-4}$	$1.41 \cdot 10^{-4}$	$1.18 \cdot 10^{-4}$	$5.05 \cdot 10^{-4}$	$3.78 \cdot 10^{-4}$	$3.03 \cdot 10^{-4}$	$3.27 \cdot 10^{-3}$	$2.00 \cdot 10^{-3}$	$1.50 \cdot 10^{-3}$
10^6	$3 \cdot 10^5$	$3.26 \cdot 10^{-4}$	$2.89 \cdot 10^{-4}$	$2.33 \cdot 10^{-4}$	$1.08 \cdot 10^{-3}$	$8.84 \cdot 10^{-4}$	$6.41 \cdot 10^{-4}$	$8.91 \cdot 10^{-3}$	$3.15 \cdot 10^{-3}$	$2.09 \cdot 10^{-3}$
$3 \cdot 10^5$	$3 \cdot 10^5$	$1.64 \cdot 10^{-4}$	$1.59 \cdot 10^{-4}$	$1.21 \cdot 10^{-4}$	$1.25 \cdot 10^{-3}$	$1.17 \cdot 10^{-3}$	$2.90 \cdot 10^{-4}$	$1.15 \cdot 10^{-2}$	$8.75 \cdot 10^{-3}$	$6.55 \cdot 10^{-4}$
10^6	10^6	$3.53 \cdot 10^{-4}$	$3.48 \cdot 10^{-4}$	$2.56 \cdot 10^{-4}$	$2.52 \cdot 10^{-3}$	$2.41 \cdot 10^{-3}$	$7.13 \cdot 10^{-4}$	$2.97 \cdot 10^{-2}$	$2.30 \cdot 10^{-2}$	$1.57 \cdot 10^{-3}$
10^7	10^6	$1.19 \cdot 10^{-3}$	$7.20 \cdot 10^{-4}$	$4.25 \cdot 10^{-4}$	$3.48 \cdot 10^{-3}$	$1.84 \cdot 10^{-3}$	$1.04 \cdot 10^{-3}$	$2.94 \cdot 10^{-2}$	$7.89 \cdot 10^{-3}$	$3.59 \cdot 10^{-3}$
10^7	$3 \cdot 10^6$	$3.20 \cdot 10^{-3}$	$1.66 \cdot 10^{-3}$	$7.45 \cdot 10^{-4}$	$1.33 \cdot 10^{-2}$	$3.56 \cdot 10^{-3}$	$1.54 \cdot 10^{-3}$	0.110	$9.44 \cdot 10^{-3}$	$4.74 \cdot 10^{-3}$
10^7	10^7	$2.20 \cdot 10^{-2}$	$1.20 \cdot 10^{-2}$	$2.05 \cdot 10^{-3}$	0.208	$9.15 \cdot 10^{-2}$	$5.79 \cdot 10^{-3}$	1.49	0.820	$1.57 \cdot 10^{-2}$
$3 \cdot 10^7$	10^7	0.412	$1.06 \cdot 10^{-2}$	$5.78 \cdot 10^{-3}$	1.57	$2.34 \cdot 10^{-2}$	$1.30 \cdot 10^{-2}$	4.91	$5.54 \cdot 10^{-2}$	$3.27 \cdot 10^{-2}$
$3 \cdot 10^7$	$3 \cdot 10^7$	3.57	0.557	$5.54 \cdot 10^{-2}$	23.0	2.21	0.120	108	8.89	0.386
10^8	10^7	∞	0.264	0.336	∞	0.867	1.05	∞	3.23	3.95
10^8	$3 \cdot 10^7$	∞	3.19	3.56	∞	9.75	10.3	∞	145	160

Table 4.2: Median, 5% and 95% quantiles of the estimated measurement errors on m_2 for different sets of binaries located at redshift $z = 1$, with low unequal-mass binaries above, low equal-mass binaries in the middle, and high-mass binaries below.

$m_1[M_\odot]$	$m_2[M_\odot]$	$\Delta\chi_1$								
		5% quantile			Median			95% quantile		
		RWF	SWF	FWF	RWF	SWF	FWF	RWF	SWF	FWF
$3 \cdot 10^5$	10^5	$4.95 \cdot 10^{-4}$	$4.11 \cdot 10^{-4}$	$2.94 \cdot 10^{-4}$	$1.47 \cdot 10^{-3}$	$1.17 \cdot 10^{-3}$	$8.12 \cdot 10^{-4}$	$9.63 \cdot 10^{-3}$	$4.83 \cdot 10^{-3}$	$3.32 \cdot 10^{-3}$
10^6	10^5	$3.81 \cdot 10^{-4}$	$2.72 \cdot 10^{-4}$	$1.97 \cdot 10^{-4}$	$8.98 \cdot 10^{-4}$	$6.11 \cdot 10^{-4}$	$4.38 \cdot 10^{-4}$	$2.72 \cdot 10^{-3}$	$1.78 \cdot 10^{-3}$	$1.39 \cdot 10^{-3}$
10^6	$3 \cdot 10^5$	$8.68 \cdot 10^{-4}$	$7.30 \cdot 10^{-4}$	$4.97 \cdot 10^{-4}$	$2.16 \cdot 10^{-3}$	$1.69 \cdot 10^{-3}$	$1.20 \cdot 10^{-3}$	$1.05 \cdot 10^{-2}$	$5.57 \cdot 10^{-3}$	$3.93 \cdot 10^{-3}$
$3 \cdot 10^5$	$3 \cdot 10^5$	$9.96 \cdot 10^{-4}$	$9.62 \cdot 10^{-4}$	$7.46 \cdot 10^{-4}$	$6.81 \cdot 10^{-3}$	$6.45 \cdot 10^{-3}$	$3.93 \cdot 10^{-3}$	$8.34 \cdot 10^{-2}$	$7.08 \cdot 10^{-2}$	$3.75 \cdot 10^{-2}$
10^6	10^6	$1.53 \cdot 10^{-3}$	$1.50 \cdot 10^{-3}$	$1.17 \cdot 10^{-3}$	$1.31 \cdot 10^{-2}$	$1.27 \cdot 10^{-2}$	$6.82 \cdot 10^{-3}$	0.218	0.189	$7.51 \cdot 10^{-2}$
10^7	10^6	$1.37 \cdot 10^{-3}$	$8.44 \cdot 10^{-4}$	$4.58 \cdot 10^{-4}$	$3.68 \cdot 10^{-3}$	$1.90 \cdot 10^{-3}$	$1.07 \cdot 10^{-3}$	$1.64 \cdot 10^{-2}$	$6.33 \cdot 10^{-3}$	$3.45 \cdot 10^{-3}$
10^7	$3 \cdot 10^6$	$3.87 \cdot 10^{-3}$	$2.41 \cdot 10^{-3}$	$1.21 \cdot 10^{-3}$	$1.47 \cdot 10^{-2}$	$5.93 \cdot 10^{-3}$	$3.03 \cdot 10^{-3}$	0.118	$2.15 \cdot 10^{-2}$	$1.24 \cdot 10^{-2}$
10^7	10^7	0.108	$5.00 \cdot 10^{-2}$	$2.04 \cdot 10^{-2}$	1.20	0.488	0.136	9.77	5.45	1.17
$3 \cdot 10^7$	10^7	0.438	$1.93 \cdot 10^{-2}$	$9.36 \cdot 10^{-3}$	1.87	$6.19 \cdot 10^{-2}$	$3.31 \cdot 10^{-2}$	7.24	0.269	0.147
$3 \cdot 10^7$	$3 \cdot 10^7$	16.8	2.04	1.31	83.6	11.9	5.35	499	61.4	26.3
10^8	10^7	∞	0.256	0.316	∞	1.10	1.35	∞	4.65	5.62
10^8	$3 \cdot 10^7$	∞	3.47	4.19	∞	15.1	16.3	∞	172	185

Table 4.3: Median, 5% and 95% quantiles of the estimated measurement errors on χ_1 for different sets of binaries located at redshift $z = 1$, with low unequal-mass binaries above, low equal-mass binaries in the middle, and high-mass binaries below.

$m_1[M_\odot]$	$m_2[M_\odot]$	$\Delta\chi_2$								
		5% quantile			Median			95% quantile		
		RWF	SWF	FWF	RWF	SWF	FWF	RWF	SWF	FWF
$3 \cdot 10^5$	10^5	$8.05 \cdot 10^{-4}$	$7.19 \cdot 10^{-4}$	$5.40 \cdot 10^{-4}$	$3.23 \cdot 10^{-3}$	$2.70 \cdot 10^{-3}$	$1.91 \cdot 10^{-3}$	$2.30 \cdot 10^{-2}$	$1.34 \cdot 10^{-2}$	$9.81 \cdot 10^{-3}$
10^6	10^5	$1.71 \cdot 10^{-3}$	$1.09 \cdot 10^{-3}$	$8.34 \cdot 10^{-4}$	$5.24 \cdot 10^{-3}$	$3.61 \cdot 10^{-3}$	$2.78 \cdot 10^{-3}$	$3.20 \cdot 10^{-2}$	$2.00 \cdot 10^{-2}$	$1.45 \cdot 10^{-2}$
10^6	$3 \cdot 10^5$	$1.41 \cdot 10^{-3}$	$1.22 \cdot 10^{-3}$	$9.01 \cdot 10^{-4}$	$4.72 \cdot 10^{-3}$	$3.91 \cdot 10^{-3}$	$2.78 \cdot 10^{-3}$	$2.65 \cdot 10^{-2}$	$1.63 \cdot 10^{-2}$	$1.20 \cdot 10^{-2}$
$3 \cdot 10^5$	$3 \cdot 10^5$	$1.02 \cdot 10^{-3}$	$9.58 \cdot 10^{-4}$	$7.83 \cdot 10^{-4}$	$6.66 \cdot 10^{-3}$	$6.34 \cdot 10^{-3}$	$3.95 \cdot 10^{-3}$	$7.84 \cdot 10^{-2}$	$6.33 \cdot 10^{-2}$	$3.68 \cdot 10^{-2}$
10^6	10^6	$1.67 \cdot 10^{-3}$	$1.66 \cdot 10^{-3}$	$1.22 \cdot 10^{-3}$	$1.27 \cdot 10^{-2}$	$1.25 \cdot 10^{-2}$	$6.76 \cdot 10^{-3}$	0.217	0.186	$7.07 \cdot 10^{-2}$
10^7	10^6	$6.33 \cdot 10^{-3}$	$3.68 \cdot 10^{-3}$	$1.98 \cdot 10^{-3}$	$3.31 \cdot 10^{-2}$	$1.63 \cdot 10^{-2}$	$9.66 \cdot 10^{-3}$	0.187	$7.57 \cdot 10^{-2}$	$4.01 \cdot 10^{-2}$
10^7	$3 \cdot 10^6$	$7.35 \cdot 10^{-3}$	$4.64 \cdot 10^{-3}$	$2.42 \cdot 10^{-3}$	$3.32 \cdot 10^{-2}$	$1.72 \cdot 10^{-2}$	$9.46 \cdot 10^{-3}$	0.193	$6.87 \cdot 10^{-2}$	$4.13 \cdot 10^{-2}$
10^7	10^7	0.111	$4.66 \cdot 10^{-2}$	$1.94 \cdot 10^{-2}$	1.22	0.511	0.130	9.94	5.60	1.11
$3 \cdot 10^7$	10^7	0.594	$4.02 \cdot 10^{-2}$	$2.07 \cdot 10^{-2}$	4.44	0.205	0.104	26.8	0.960	0.496
$3 \cdot 10^7$	$3 \cdot 10^7$	16.1	2.20	1.34	83.0	11.4	5.43	515	59.5	26.5
10^8	10^7	∞	1.07	1.38	∞	11.7	13.7	∞	52.8	62.6
10^8	$3 \cdot 10^7$	∞	8.31	9.25	∞	48.0	50.4	∞	657	700

Table 4.4: Median, 5% and 95% quantiles of the estimated measurement errors on χ_2 for different sets of binaries located at redshift $z = 1$, with low unequal-mass binaries above, low equal-mass binaries in the middle, and high-mass binaries below.

$m_1[M_\odot]$	$m_2[M_\odot]$	$2a$ [′]								
		5% quantile			Median			95% quantile		
		RWF	SWF	FWF	RWF	SWF	FWF	RWF	SWF	FWF
$3 \cdot 10^5$	10^5	5.09	4.96	3.18	20.2	18.5	12.7	92.2	85.8	67.2
10^6	10^5	8.67	8.13	7.14	34.1	28.2	20.1	124	100	82.5
10^6	$3 \cdot 10^5$	8.95	8.61	6.28	31.4	28.0	19.8	124	110	85.0
$3 \cdot 10^5$	$3 \cdot 10^5$	6.00	5.81	3.73	26.6	25.4	18.6	113	109	97.7
10^6	10^6	8.45	8.40	5.42	38.5	37.6	26.3	158	154	129
10^7	10^6	19.2	15.5	8.34	64.2	48.4	23.2	316	199	113
10^7	$3 \cdot 10^6$	19.5	17.4	7.31	84.3	65.2	31.0	461	283	158
10^7	10^7	32.7	27.4	11.6	202	155	77.7	1360	818	496
$3 \cdot 10^7$	10^7	169	68.5	24.4	1500	319	133	16600	1550	738
$3 \cdot 10^7$	$3 \cdot 10^7$	7910	537	363	188000	2590	2570	2890000	14700	16400
10^8	10^7	∞	998	1300	∞	3380	4400	∞	18200	23800
10^8	$3 \cdot 10^7$	∞	5900	6510	∞	26300	31000	∞	237000	279000

Table 4.5: Median, 5% and 95% quantiles of the estimated measurement errors on the major axis of the localization ellipse in the sky for different sets of binaries located at redshift $z = 1$, with low unequal-mass binaries above, low equal-mass binaries in the middle, and high-mass binaries below.

$m_1[M_\odot]$	$m_2[M_\odot]$	$2b$ [′]								
		5% quantile			Median			95% quantile		
		RWF	SWF	FWF	RWF	SWF	FWF	RWF	SWF	FWF
$3 \cdot 10^5$	10^5	0.795	0.778	0.453	3.76	3.49	2.10	13.8	12.1	7.40
10^6	10^5	2.17	1.69	0.985	10.2	7.61	4.50	23.6	15.5	10.2
10^6	$3 \cdot 10^5$	1.83	1.63	0.984	8.63	7.70	4.47	24.4	19.2	12.5
$3 \cdot 10^5$	$3 \cdot 10^5$	1.00	1.00	0.575	5.52	5.29	3.17	20.3	18.6	13.8
10^6	10^6	1.62	1.61	0.948	9.11	9.04	5.26	31.9	29.9	19.4
10^7	10^6	3.40	2.81	1.17	15.7	12.5	5.20	41.3	27.2	12.3
10^7	$3 \cdot 10^6$	3.04	2.65	1.11	13.8	11.9	4.87	54.3	37.2	17.3
10^7	10^7	5.77	4.64	1.93	24.8	21.6	9.49	125	90.8	48.3
$3 \cdot 10^7$	10^7	36.4	11.1	4.00	164	47.9	17.5	896	157	69.9
$3 \cdot 10^7$	$3 \cdot 10^7$	727	108	57.2	5740	306	230	85000	1090	1350
10^8	10^7	∞	201	251	∞	724	930	∞	2610	3600
10^8	$3 \cdot 10^7$	∞	1140	1340	∞	3890	4630	∞	44400	52500

Table 4.6: Median, 5% and 95% quantiles of the estimated measurement errors on the minor axis of the localization ellipse in the sky for different sets of binaries located at redshift $z = 1$, with low unequal-mass binaries above, low equal-mass binaries in the middle, and high-mass binaries below.

$m_1[M_\odot]$	$m_2[M_\odot]$	$\Delta d_L/d_L$								
		5% quantile			Median			95% quantile		
		RWF	SWF	FWF	RWF	SWF	FWF	RWF	SWF	FWF
$3 \cdot 10^5$	10^5	$8.67 \cdot 10^{-4}$	$8.24 \cdot 10^{-4}$	$5.76 \cdot 10^{-4}$	$2.94 \cdot 10^{-3}$	$2.43 \cdot 10^{-3}$	$1.75 \cdot 10^{-3}$	$1.28 \cdot 10^{-2}$	$1.01 \cdot 10^{-2}$	$8.43 \cdot 10^{-3}$
10^6	10^5	$2.08 \cdot 10^{-3}$	$1.44 \cdot 10^{-3}$	$1.03 \cdot 10^{-3}$	$4.90 \cdot 10^{-3}$	$3.51 \cdot 10^{-3}$	$2.44 \cdot 10^{-3}$	$1.49 \cdot 10^{-2}$	$8.74 \cdot 10^{-3}$	$7.04 \cdot 10^{-3}$
10^6	$3 \cdot 10^5$	$1.75 \cdot 10^{-3}$	$1.43 \cdot 10^{-3}$	$1.11 \cdot 10^{-3}$	$4.62 \cdot 10^{-3}$	$3.74 \cdot 10^{-3}$	$2.70 \cdot 10^{-3}$	$1.97 \cdot 10^{-2}$	$1.39 \cdot 10^{-2}$	$1.12 \cdot 10^{-2}$
$3 \cdot 10^5$	$3 \cdot 10^5$	$1.13 \cdot 10^{-3}$	$1.08 \cdot 10^{-3}$	$7.20 \cdot 10^{-4}$	$4.41 \cdot 10^{-3}$	$3.80 \cdot 10^{-3}$	$2.88 \cdot 10^{-3}$	$1.89 \cdot 10^{-2}$	$1.48 \cdot 10^{-2}$	$1.27 \cdot 10^{-2}$
10^6	10^6	$1.85 \cdot 10^{-3}$	$1.77 \cdot 10^{-3}$	$1.12 \cdot 10^{-3}$	$6.88 \cdot 10^{-3}$	$6.20 \cdot 10^{-3}$	$4.36 \cdot 10^{-3}$	$2.65 \cdot 10^{-2}$	$2.02 \cdot 10^{-2}$	$1.71 \cdot 10^{-2}$
10^7	10^6	$3.14 \cdot 10^{-3}$	$2.32 \cdot 10^{-3}$	$1.48 \cdot 10^{-3}$	$8.53 \cdot 10^{-3}$	$6.25 \cdot 10^{-3}$	$3.45 \cdot 10^{-3}$	$4.14 \cdot 10^{-2}$	$1.94 \cdot 10^{-2}$	$1.26 \cdot 10^{-2}$
10^7	$3 \cdot 10^6$	$3.84 \cdot 10^{-3}$	$3.11 \cdot 10^{-3}$	$2.18 \cdot 10^{-3}$	$1.09 \cdot 10^{-2}$	$8.03 \cdot 10^{-3}$	$4.69 \cdot 10^{-3}$	$7.26 \cdot 10^{-2}$	$3.43 \cdot 10^{-2}$	$1.99 \cdot 10^{-2}$
10^7	10^7	$1.45 \cdot 10^{-2}$	$8.99 \cdot 10^{-3}$	$6.78 \cdot 10^{-3}$	$6.05 \cdot 10^{-2}$	$2.76 \cdot 10^{-2}$	$2.03 \cdot 10^{-2}$	0.277	0.113	$7.82 \cdot 10^{-2}$
$3 \cdot 10^7$	10^7	0.212	$1.94 \cdot 10^{-2}$	$1.68 \cdot 10^{-2}$	0.801	$4.63 \cdot 10^{-2}$	$3.52 \cdot 10^{-2}$	3.44	0.186	0.101
$3 \cdot 10^7$	$3 \cdot 10^7$	3.52	0.188	0.213	31.7	0.614	0.523	462	2.33	2.23
10^8	10^7	∞	0.257	0.424	∞	0.698	1.11	∞	2.53	4.00
10^8	$3 \cdot 10^7$	∞	1.76	3.17	∞	5.53	9.16	∞	69.7	111

Table 4.7: Median, 5% and 95% quantiles of the estimated measurement errors on d_L for different sets of binaries located at redshift $z = 1$, with low unequal-mass binaries above, low equal-mass binaries in the middle, and high-mass binaries below.

For these systems, the gain in accuracy obtained in the determination of all interesting parameters with respect to the RWF is typically a factor ~ 1.5 for the FWF and a factor ~ 1.2 for the SWF. However, when the mass ratio is close to 1:3, the distribution of the errors on the individual masses for the RWF has a relatively long tail of bad errors, which is absent for the SWF and FWF.

The fact that including such extra structure as contained in the FWF fails to provide much extra accuracy can allow for the inclusion of extra parameters in the template, such as eccentricity or alternative gravity parameters.

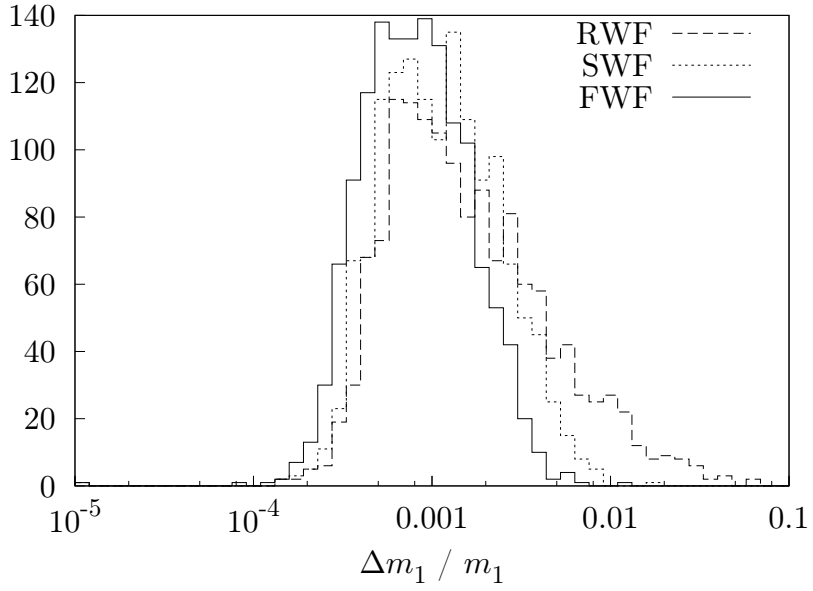

Figure 4.1: Estimated distribution of the measurement error on m_1 for a low unequal-mass binary system with $m_1 = 10^6 M_\odot$ and $m_2 = 3 \cdot 10^5 M_\odot$. We expect errors as high as $8 \cdot 10^{-3}$ with the RWF (95% percentile), whereas we do not expect errors higher than $1.5 \cdot 10^{-3}$ with the FWF.

4.2.2 Low equal-mass binaries

In this class, we place all systems of equal-mass black holes, with total mass smaller than $10^7 M_\odot$. As a representative sample, we choose to present systems with $m_1 = m_2 = 3 \times 10^5 M_\odot$. We plot the estimated distribution of the errors on m_1 in Fig. 4.5, on χ_1 in Fig. 4.6, on the sky positioning in Fig. 4.7, and on d_L in Fig. 4.8.

In these cases, the errors on extrinsic parameters are, as for unequal-mass systems, improved by a factor ~ 1.5 for the FWF with respect to the RWF. The errors on the spins are improved for the worst cases by a factor 2 - 4, and typically by a factor 1.5 - 2 for the FWF with respect to the two other waveforms. However, the error on the individual masses is improved typically by a factor 3.5 - 4.5, and even by a factor 10 - 20 in the worst cases, comparing the FWF with the two others. Thus, far more information can be

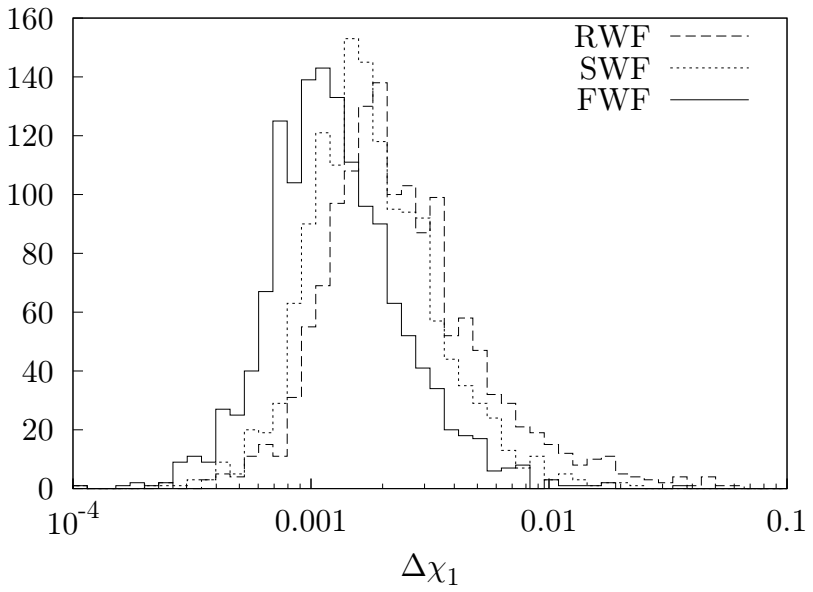

Figure 4.2: Estimated distribution of the measurement error on χ_1 for a low unequal-mass binary system with $m_1 = 10^6 M_\odot$ and $m_2 = 3 \times 10^5 M_\odot$. We expect the error to be 1.5 - 2 times lower using the FWF than using the RWF.

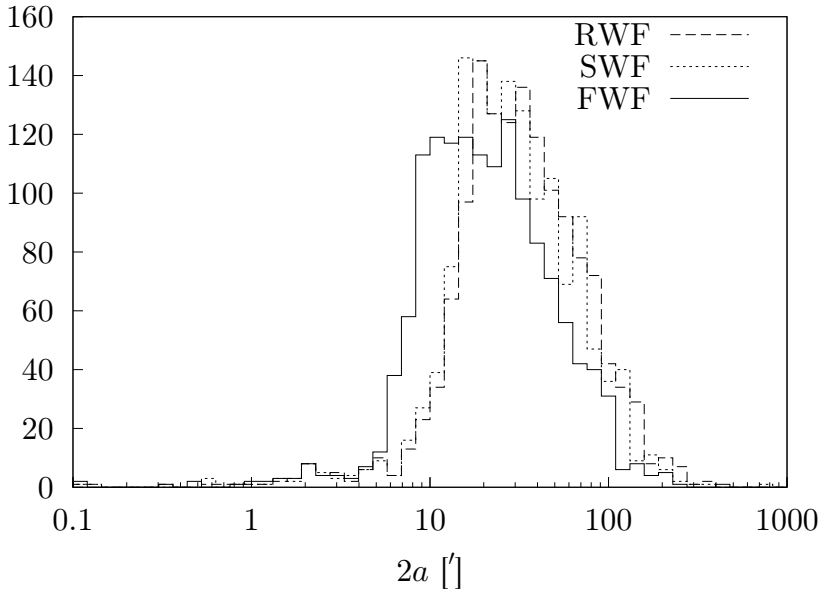

Figure 4.3: Estimated distribution of the major axis of the positioning error ellipse for a low unequal-mass binary system with $m_1 = 10^6 M_\odot$ and $m_2 = 3 \times 10^5 M_\odot$. We expect the error to be ~ 1.5 times lower using the FWF than using the RWF.

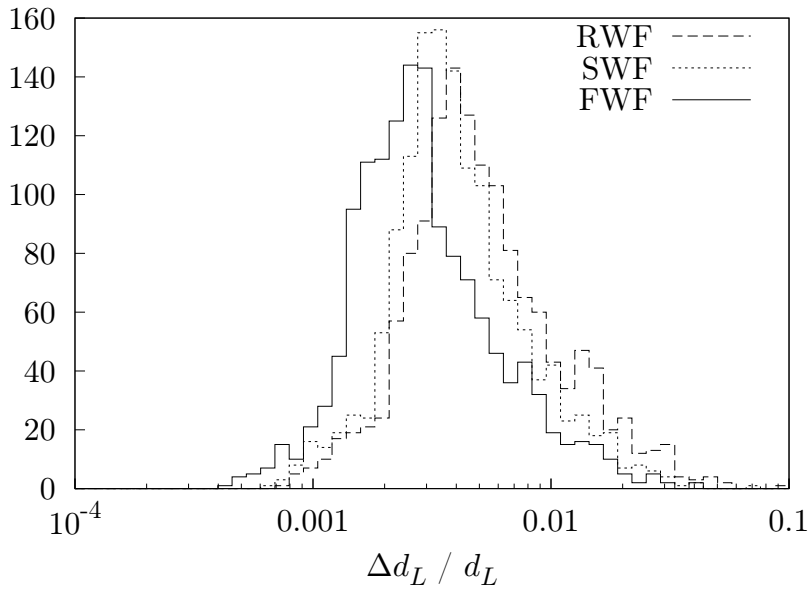

Figure 4.4: Estimated distribution of the measurement error on d_L for a low unequal-mass binary system with $m_1 = 10^6 M_\odot$ and $m_2 = 3 \times 10^5 M_\odot$. We expect the error to be ~ 1.5 times less using the FWF than using the RWF.

extracted from a measure of an equal-mass binary system using the former waveform than one of the latter.

The SWF brings little improvement for intrinsic parameters in these cases, because the odd harmonics are absent. It therefore has only two corrections to the RWF instead of five for unequal-mass systems.

4.2.3 High-mass binaries

In this class, we place all systems with total mass higher than $10^7 M_\odot$. As a representative sample, we choose to present systems with $m_1 = 3 \times 10^7 M_\odot$ and $m_2 = 10^7 M_\odot$. We plot the estimated distribution of the errors on m_1 in Fig. 4.9, on χ_1 in Fig. 4.10, on the sky positioning in Fig. 4.11, and on d_L in Fig. 4.12.

For this class of binaries, the second harmonic is hardly or not at all visible in the LISA band, so the RWF fails to provide good accuracy unless the total mass is close to $10^7 M_\odot$. However, the SWF and FWF still provide relatively high precision for the masses, spins and luminosity distance of a system with $m_1 = 3 \times 10^7 M_\odot$ at redshift $z = 1$.

For equal-mass systems in this class, the FWF provides an improvement of a factor 10 - 30 for the determination of the masses with respect to the SWF in all cases. For other parameters and/or other mass ratios, the improvement using the FWF is a factor 1.5 - 2 with respect to the SWF. The fact that the SWF seems to give better results than the FWF for the highest-mass systems comes from the fact that the SNR for systems in this mass range is higher with the former than with the latter. However, we do not expect to

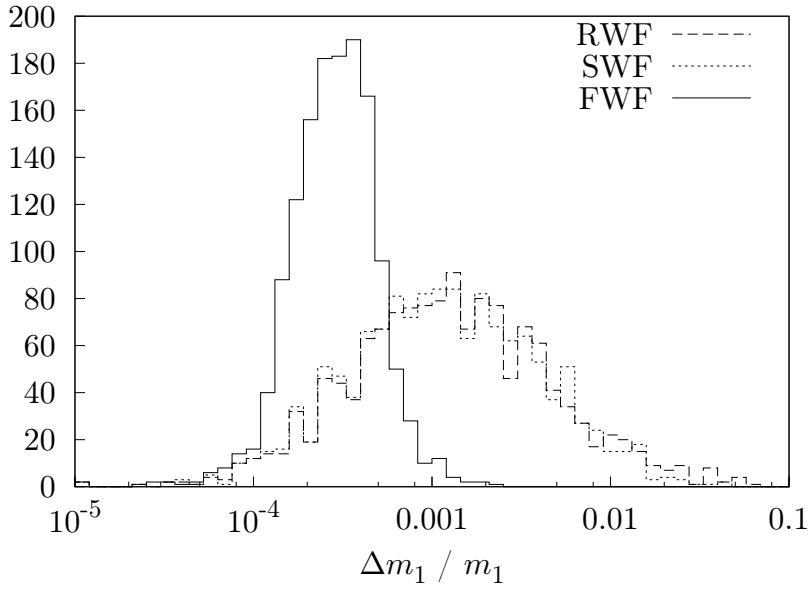

Figure 4.5: Estimated distribution of the measurement error on m_1 for a low equal-mass binary system with $m_1 = m_2 = 3 \cdot 10^5 M_\odot$. The FWF clearly gives better results than the two other waveforms.

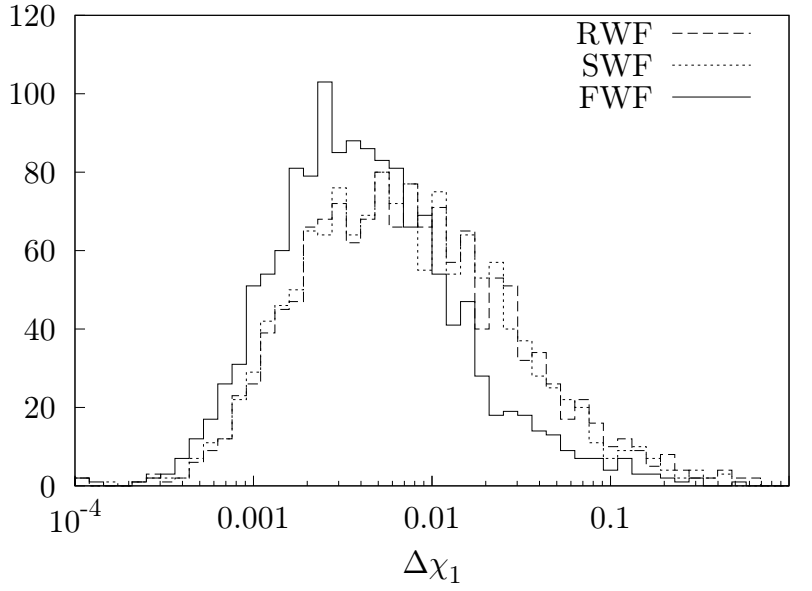

Figure 4.6: Estimated distribution of the measurement error on χ_1 for a low equal-mass binary system with $m_1 = m_2 = 3 \cdot 10^5 M_\odot$. The improvement on the median value is a factor 1.5 - 2 and on the 95% quantile a factor 2 - 4 for the FWF with respect to the other two waveforms.

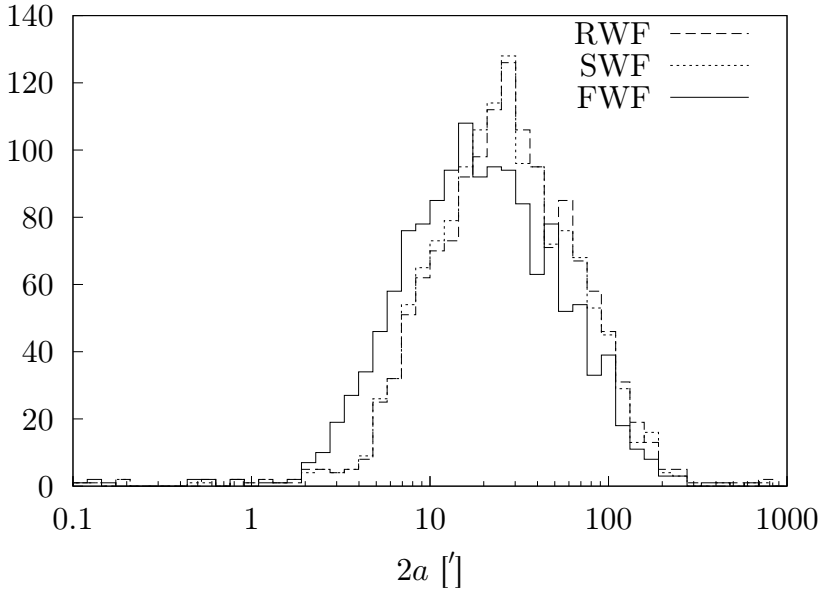

Figure 4.7: Estimated distribution of the major axis of the positioning error ellipse for a low equal-mass binary system with $m_1 = m_2 = 3 \cdot 10^5 M_\odot$. We expect the error to be ~ 1.5 times lower using the FWF than using the RWF.

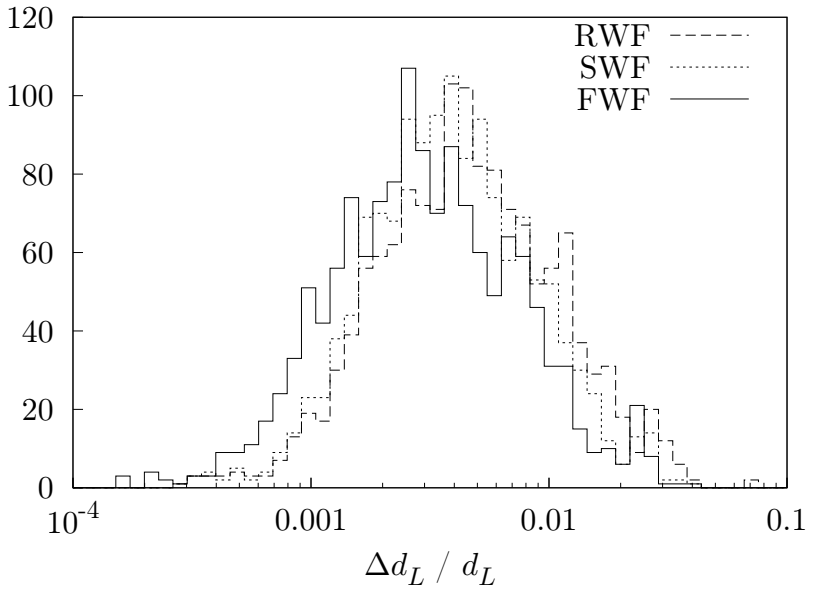

Figure 4.8: Estimated distribution of the measurement error on d_L for a low equal-mass binary system with $m_1 = m_2 = 3 \cdot 10^5 M_\odot$. We expect the error to be ~ 1.5 times lower using the FWF than using the RWF.

extract more information from a more approximate waveform.

Furthermore, some information can still be extracted from binaries that are completely invisible to the RWF using higher harmonics.

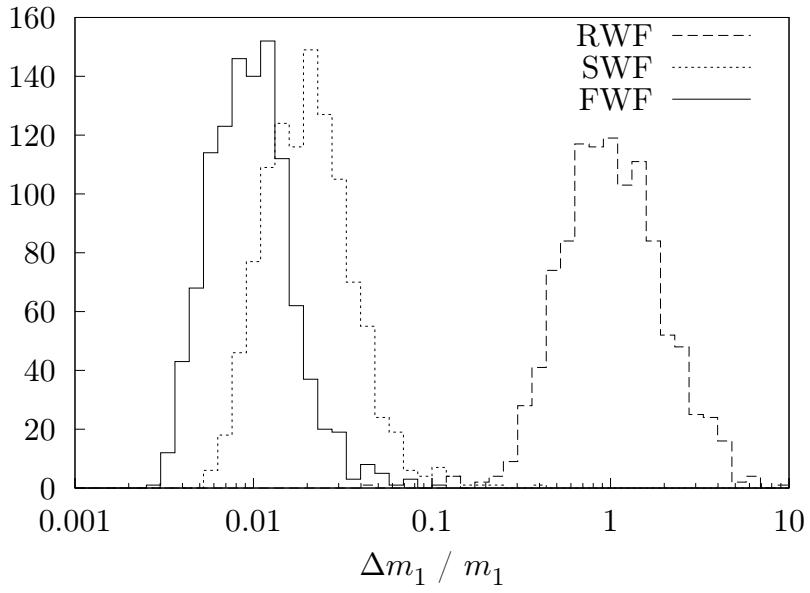

Figure 4.9: Estimated distribution of the measurement error on m_1 for a high-mass binary system with $m_1 = 3 \cdot 10^7 M_\odot$ and $m_2 = 10^7 M_\odot$. Very few systems are measurable with the RWF with a precision less than 50%, whereas the other two waveforms provide in the worst cases a few percent precision, the FWF typically a factor of 1.5 - 2 better than the SWF.

4.2.4 Upper mass limit

We present here the proportion of systems for all samples for which both individual masses can be measured at the level of 25% and 50% at a redshift of $z = 1$ in Table 4.8, as well as the luminosity distance in Table 4.9. When at least 25% accuracy is obtainable for all systems of a sample, we do not show it on the table.

We see in the tables that the RWF reaches its limits for $10^7 M_\odot$ binaries, whereas the SWF and FWF can still provide significant information for $3 \times 10^7 M_\odot$ binaries, and even for some $10^8 M_\odot$ binaries with high enough mass ratio.

Furthermore, we computed from our simulations the maximum redshift at which a binary system is observable, as a function of m_1, for different values of the mass ratio. We choose to call a system with parameters (m_1, m_2, z) observable if at least half of the systems of these masses at this redshift have both individual masses measurable with at least 25% precision. Fig. 4.13 shows the maximum redshift at which equal-mass systems can be observed, in Fig. 4.14 the same for systems with a mass ratio between 1:3 and 3:10,

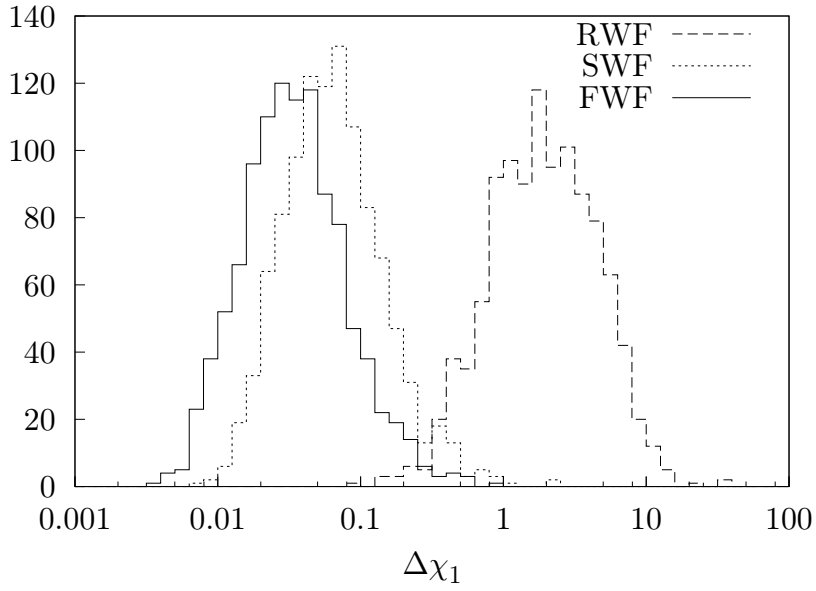

Figure 4.10: Estimated distribution of the measurement error on χ_1 for a high-mass binary system with $m_1 = 3 \cdot 10^7 M_\odot$ and $m_2 = 10^7 M_\odot$. We can see that no information on the spins can be extracted with the RWF, whereas some can be extracted with the two others in all cases, a factor of two better for the FWF than for the SWF.

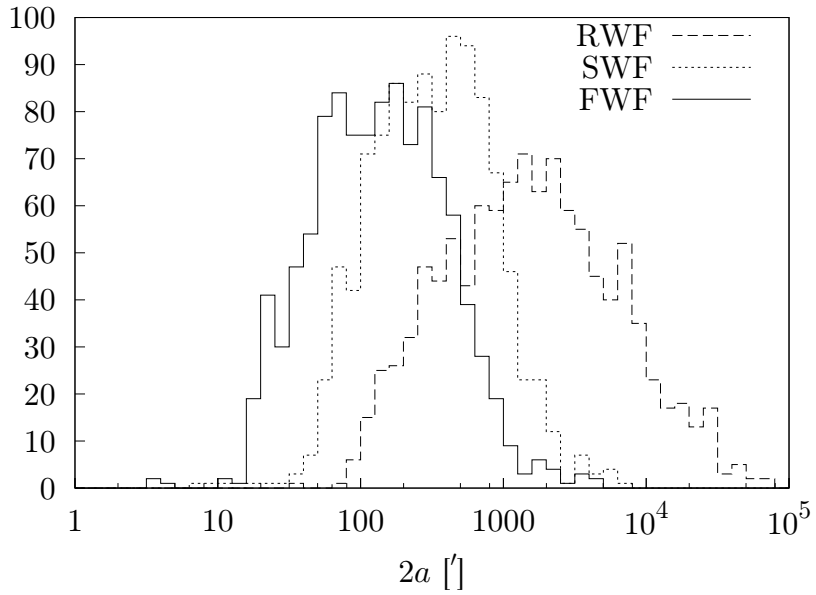

Figure 4.11: Estimated distribution of the major axis of the positioning error ellipse for a high-mass binary system with $m_1 = 3 \cdot 10^7 M_\odot$ and $m_2 = 10^7 M_\odot$. We expect to have a positioning error in the best cases (5% quantile) of 2.8° for the RWF, of 1° for the SWF, and of 25′ for the FWF.

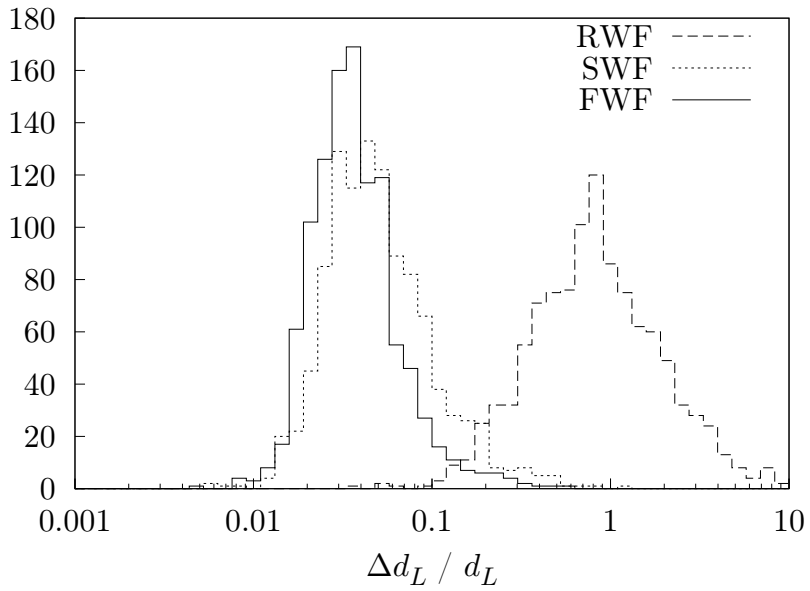

Figure 4.12: Estimated distribution of the measurement error on d_L for a high-mass binary system with $m_1 = 3 \cdot 10^7 M_\odot$ and $m_2 = 10^7 M_\odot$. We do not expect a measurement more accurate than 20% to be possible with the RWF, whereas the accuracy should be always less than 20% with the SWF, and less than 10% with the FWF.

$m_1[M_\odot]$	$m_2[M_\odot]$	25%			50%		
		RWF	SWF	FWF	RWF	SWF	FWF
10^7	$3 \cdot 10^6$	98%	100%	100%	100%	100%	100%
10^7	10^7	50%	75%	100%	71%	89%	100%
$3 \cdot 10^7$	10^7	1%	100%	100%	5%	100%	100%
$3 \cdot 10^7$	$3 \cdot 10^7$	0%	0%	84%	0%	3%	98%
10^8	10^7	0%	4%	2%	0%	21%	15%
10^8	$3 \cdot 10^7$	0%	0%	0%	0%	0%	0%

Table 4.8: Proportion of the systems in all samples where both individual masses can be determined with an accuracy better than 25%, resp. 50%.

$m_1[M_\odot]$	$m_2[M_\odot]$	25%			50%		
		RWF	SWF	FWF	RWF	SWF	FWF
10^7	10^7	94%	99%	100%	99%	100%	100%
$3 \cdot 10^7$	10^7	8%	97%	99%	28%	100%	100%
$3 \cdot 10^7$	$3 \cdot 10^7$	0%	12%	9%	0%	40%	47%
10^8	10^7	0%	5%	1%	0%	29%	10%
10^8	$3 \cdot 10^7$	0%	0%	0%	0%	2%	0%

Table 4.9: Proportion of the systems in all samples where the luminosity distance can be determined with an accuracy better than 25%, resp. 50%.

and in Fig. 4.15 the same for systems with a mass ratio of 1:10. Some points are absent in the plots, because no signal at all could be extracted from the RWF when the higher-mass black hole had a redshifted mass $m_1 \approx 10^8 M_\odot$.

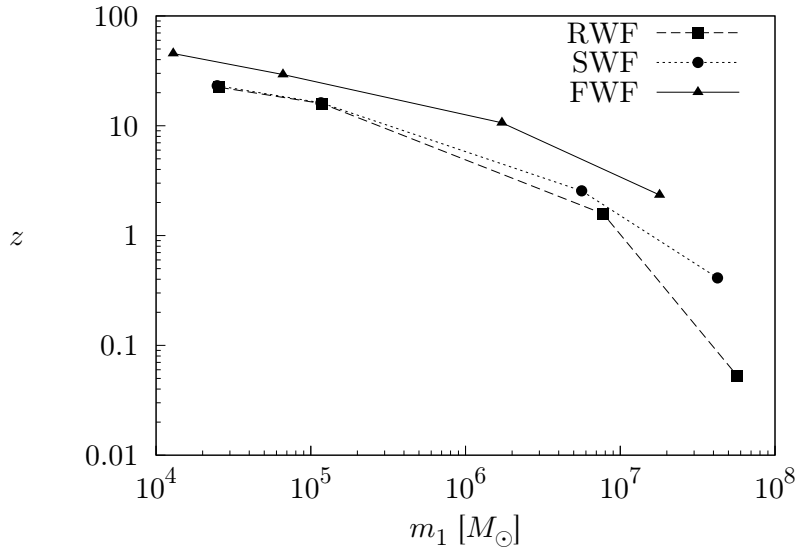

Figure 4.13: Maximum redshift at which a system is observable as a function of the mass of the black holes, for equal-mass systems. The FWF allows to observe 10^4 - $10^5 M_\odot$ binaries up to $z = 30$ - 50, the other two up to $z = 15$ - 25. A binary of $\sim 2 \cdot 10^7 M_\odot$ black holes should be observable up to $z \approx 2$ with the FWF, $z \approx 1$ with the SWF, and $z \approx 0.3$ with the RWF.

The figures show that a much higher redshift can be reached with the FWF than with the other waveforms, and that the difference is bigger for mass ratios closer to 1:1. The FWF is giving the possibility to observe any binary system with total mass of $M \leq 10^7 M_\odot$ up to a redshift of $z \gtrsim 10$, whereas the other waveforms fail, especially for equal-mass systems. The same combinations of redshifted masses can be observed with the FWF at

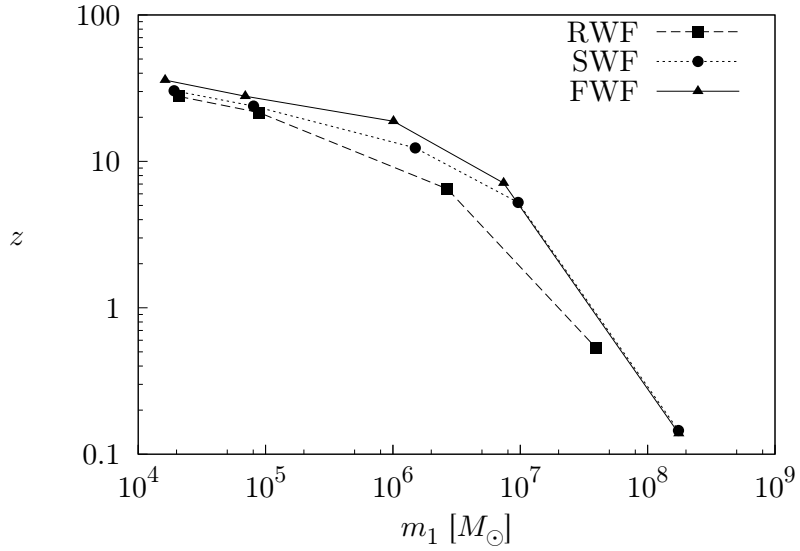

Figure 4.14: Maximum redshift at which a system is observable as a function of the mass of the most massive black hole, for systems with a mass ratio between 1:3 and 3:10. A binary with $m_1 \approx 2 \cdot 10^4 M_\odot$ should be observable up to $z \approx 36$ with the FWF, up to $z \approx 30$ with the SWF, up to $z \approx 28$ with the RWF. A binary with $m_1 \approx 10^7 M_\odot$ should be observable up to $z \approx 7$ with the FWF, up to $z \approx 6$ with the SWF, and up to $z \approx 2$ with the RWF.

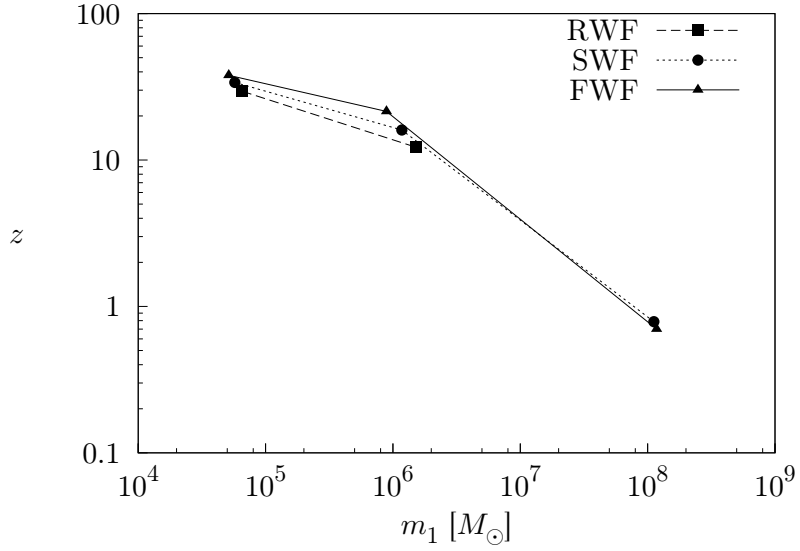

Figure 4.15: Maximum redshift at which a system is observable as a function of the mass of the most massive black hole, for systems with a mass ratio of 1:10. A binary with $m_1 \approx 6 \cdot 10^4 M_\odot$ should be observable up to $z \approx 38$ with the FWF, up to $z \approx 34$ with the SWF, up to $z \approx 29$ with the RWF. A binary with $m_1 \approx 10^8 M_\odot$ should still be observable up to $z \approx 0.7$ with the FWF and SWF, and not visible at all with the RWF.

redshifts 1.5 - 5 times higher than with the RWF, which could greatly help constraining black hole and galaxy formation models [40].

4.2.5 Extrinsic parameters

We show here the maximum redshift at which the observation of a merger event is likely to constrain the Hubble diagram. To do so, we plot the maximum redshift where the major axis of the positioning error ellipse is less than $30'$ for half of the binaries, as a function of the mass of the most massive black hole. Equal-mass binaries are shown in Fig. 4.16, binaries with mass ratio between 1:3 and 3:10 in Fig. 4.17, and binaries with a mass ratio of 1:10 in Fig. 4.18.

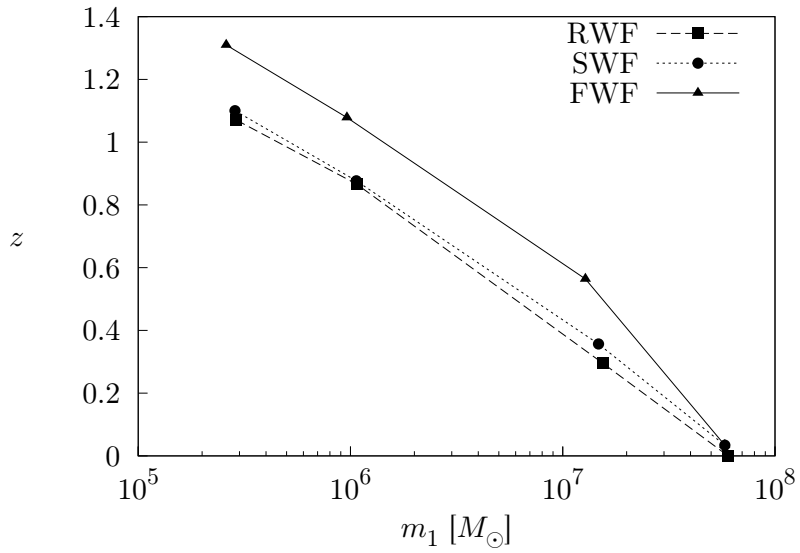

Figure 4.16: Maximum redshift at which the binary can be located with a $30'$ precision as function of the mass of the most massive black hole, for equal-mass systems. The FWF allows to locate a binary accurately up to a redshift of ~ 0.2 greater than the two other waveforms.

We find that in all cases, the localization in the sky is far more difficult than the determination of the luminosity distance. Irrespective of the waveforms, masses and mass ratios, the luminosity distance can be measured with a precision of 0.3% - 0.5% when the major axis of the positioning error ellipse is $30'$.

The FWF could help in locating binaries accurately enough for the observation of their merger to become possible up to redshifts 0.2 - 0.4 greater than the two other waveforms. The SWF could furthermore, in the case of unequal-mass binaries, go up to redshifts ~ 0.1 greater than the RWF.

Our simulations show that supermassive black hole binaries could be very accurate standard candles, and could successfully extend the measurements of the Hubble diagram

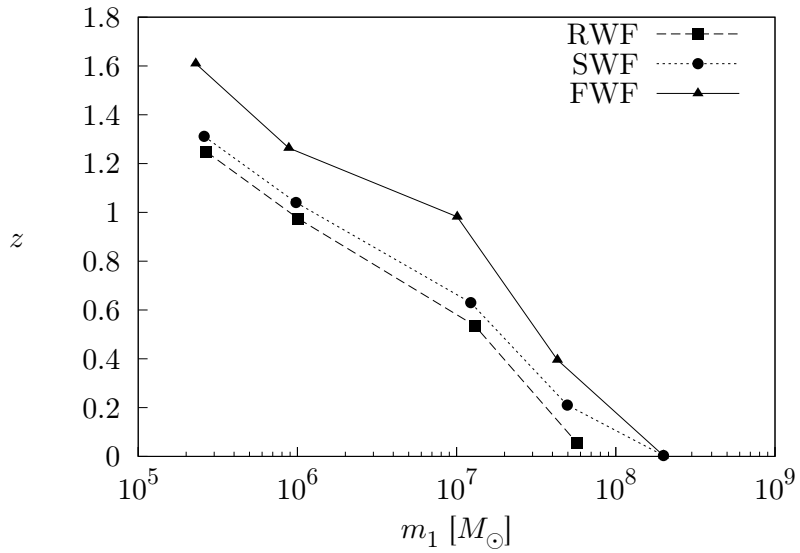

Figure 4.17: Maximum redshift at which the binary can be located with a 30′ precision as a function of the mass of the most massive black hole, for systems with a mass ratio between 1:3 and 3:10. The FWF allows to locate a binary accurately up to a redshift of 0.2 - 0.3 greater than the SWF, and the SWF up to a redshift of ~ 0.1 greater than the RWF.

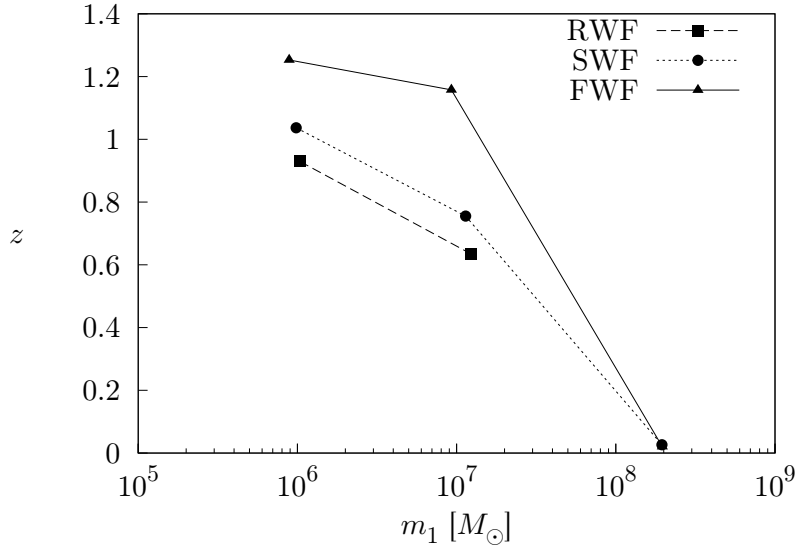

Figure 4.18: Maximum redshift at which the binary can be located with a 30′ precision as a function of the mass of the most massive black hole, for systems with a mass ratio of 1:10. The FWF allows to locate a binary accurately up to a redshift of 0.2 - 0.4 greater than the SWF, and the SWF up to a redshift of ~ 0.1 greater than the RWF.

up to redshifts of $z = 1.6$, with a precision on the luminosity distance of a few per mille. This would be a great breakthrough in the distance ladder, as the current most effective standard candles at large distances, type Ia supernovae, provide much less precision on large luminosity distances.

Chapter 5

Full eccentric waveform

In this chapter, we present a set of simulations which we are currently running using the eccentric templates described in section 3.4. The purpose of this study is to understand the impact of the eccentricity on a waveform including spin-induced precession and subdominant harmonics on parameter estimation for the planned space-based interferometer LISA.

5.1 Simulations

We present here a set of Monte Carlo simulations to estimate the measurement accuracy that could be reachable using the templates described in Section 3.4 to describe supermassive black hole binary mergers with LISA. The parameters we use, gathered in the vector $\boldsymbol{\theta}$, are

- $lm_1 = \log m_1$ and $lm_2 = \log m_2$, the logarithms of the mass of each black hole.
- χ_1 and χ_2, the dimensionless spin parameter of each black hole.
- t_c, the time at which $z = 1/6$, where $z = [GMn(1+k)/c^3]^{2/3}$ is the post-Newtonian parameter associated with the mean angular frequency $\omega = n(1+k)$.
- e_0, the eccentricity at $t = t_0$, where t_0 is the time at which the post-Newtonian parameter x is equal to $x = (256c^3\nu T/5GM)^{-1/4}$, where $T = 10$ years.
- l_0, the mean anomaly at $t = t_0$.
- p_0, the phase of the periastron at $t = t_0$.
- ld_L, the logarithm of the luminosity distance to the source d_L.
- $\mu_L = \cos(\theta_L)$ and ϕ_L, the polar angles of the orbital angular momentum at $t = t_0$.
- $\mu_1 = \cos(\theta_1)$ and ϕ_1, the polar angles of the spin of the first black hole at $t = t_0$.

- $\mu_2 = \cos(\theta_2)$ and ϕ_2, the polar angles of the spin of the second black hole at $t = t_0$.
- $\mu_N = \cos(\theta_N)$ and ϕ_N, the polar angles of the vector pointing to the source from the Solar System.

We first select a mass for the two black holes between $10^5 M_\odot$ and $10^8 M_\odot$ with steps of $\sqrt{10}$ on a logarithmic scale, so that the mass ratio does not exceed 10. We then select an eccentricity e_0 between 10^{-3} and $10^{-0.5}$ with steps of $\sqrt{10}$ on a logarithmic scale, or zero. Whenever the eccentricity is lower than the minimal value $e^2_{\min} = 5x^2[\tau(1,1,0) - \sigma(2,2,0)]/340$ (see Section 3.3), we set $e_0 = e_{\min}$. We finally set the luminosity distance to $d_L(z = 1)$ given a standard ΛCDM cosmology. As it enters the waveform only through a global multiplication factor, the scaling of the error with respect to it is straightforward to compute. For each of these 126 combinations, we then select a set of a thousand parameter points with the other parameters chosen randomly with a flat distribution. For each of these points, we solve the evolution equations (3.106) to (3.120), (3.1), and (3.2) numerically using a fourth order adaptive Runge-Kutta method. We then separate the waveform into different harmonics, each arising from a single term in (3.139) for a given couple (p, q), with a constant sign of the corresponding frequency and a constant sign of its time derivative. Schematically, we get

$$\tilde{h}(f) = \sum_{p\geq 0,q,n} \tilde{h}^{(n)}_{(p,q)}(f), \tag{5.1}$$

with $\tilde{h}^{(n)}_{(p,q)} = H_1$ in (3.148) for $q \geq 0$, and $\tilde{h}^{(n)}_{(p,q)} = H_2$ or H_3 in (3.148) for $q < 0$. Defined this way, the equations (3.152) to (3.154) have only one solution for each harmonic. We implemented 2PN waveforms, which implies that we only have to consider $q \leq 6$, and stop the expansion in the eccentricity at the order e^{10}, which implies that we only have to consider $|q| \leq 10$. Furthermore, we define the loudness of a harmonic as $L^{(n)}_{(p,q)} = \max(x^s)\max(e^q)$, where s is the PN order of harmonic p, taken over the time interval where the particular harmonic is defined; we discard every harmonic for which $L^{(n)}_{(p,q)} < 10^{-10} L_{\max}$, where $L_{\max}$ is the loudness of the loudest harmonic present. We then compute the Fisher matrix elements for each of the detectors using an adaptive Clenshaw-Curtis algorithm. We were able to find five of the needed derivatives analytically. Two simple ones are

$$\frac{\partial \tilde{h}_k}{\partial l d_L} = -\tilde{h}_k, \tag{5.2}$$

$$\frac{\partial \tilde{h}_k}{\partial l_0} = -\sum_{p,q\geq 0} iq\tilde{h}^{(p,q)}_k, \tag{5.3}$$

where $\tilde{h}^{(p,q)}_k = H_1$, $-H_2$ or H_3 described in (3.149), (3.150) and (3.151) when applicable.

The three other derivatives that we were able to determine analytically are the ones with respect to t_c, μ_N and ϕ_N, which are straightforward but lengthy to compute, which is why we do not show them here.

The derivatives that we had to compute numerically were obtained with the formula

$$\frac{\partial \tilde{h}}{\partial \theta^i} = \sum_{p\geq 0,q,n} \left(\frac{\partial H_{p,q,n}}{\partial \theta^i} + i\bar{H}_{p,q,n} \frac{\partial \psi_{p,q,n}}{\partial \theta^i} \right) \exp\left(i\bar{\psi}_{p,q,n}\right), \tag{5.4}$$

where H and $\bar{H}$ correspond to the complex amplitudes in (3.149) to (3.151), and ψ and $\bar{\psi}$ correspond to the phase in these equations. To compute them, we evolve a system with parameters $\theta^i_+ = \theta^i + \epsilon/2$ and another with parameters $\theta^i_- = \theta^i - \epsilon/2$, the other parameters coinciding with the point where we want to compute the derivative. We then use the formulas

$$\frac{\partial H}{\partial \theta^i} = \frac{H(\boldsymbol{\theta}_+) - H(\boldsymbol{\theta}_-)}{\epsilon}, \tag{5.5}$$

$$\bar{H} = \frac{H(\boldsymbol{\theta}_+) + H(\boldsymbol{\theta}_-)}{2}, \tag{5.6}$$

and similarly for ψ. We use a constant value of $\epsilon = 10^{-7}$ for every parameter, except for ϕ_L for which ϵ is divided by $\sin(\theta_L)$, μ_i ($i \in \{1, 2\}$) for which ϵ is divided by $5\chi_i$, and ϕ_i for which ϵ is divided by $5\chi_i \sin(\theta_i)$.

We launched simulations that use this waveform, to probe the impact of the eccentricity on parameter estimation with LISA. They are currently running, and we are waiting for their completion to publish the results.

Chapter 6

Conclusion

The fact that the detection of gravitational waves with interferometric detectors relies on template-based searches demands that the most accurate waveform available must be used for detecting systems emitting such waves. The gravitational waveform of two spinning bodies orbiting each other is however complicated, and each new further step implies further corrections to the waveform. Knowing whether it is worth it using a more accurate waveform, and under what cases, is a must.

6.1 Circular templates

We found that the addition of higher harmonics to the waveform at the 2PN level can help increase the mass limit above which no information can be extracted from the signal. The amplitude corrections can also bring important improvements to the determination of the individual masses, also for lower-mass binaries. The FWF allows for detecting binaries up to redshifts $z > 40$, whereas the other waveforms can allow detection up to $z \approx 30$. This could be very interesting for constraining galaxy and black hole formation models.

The range of LISA could be also extended for the determination of the Hubble diagram by using a more accurate waveform. The RWF would allow the measurement of the redshift-luminosity distance relation at a few per mille precision up to $z \approx 1.2$, whereas the FWF would allow measures with the same precision up to $z \approx 1.6$. It would be interesting to quantify how well LISA would be able to determine the Hubble diagram.

The use of the full waveform as a template for the gravitational radiation of comparable-mass binaries can be important for the extraction of as much information as possible, especially for high-mass and/or close to equal-mass binaries. However, in the case of unequal low-mass binaries at low redshifts, the restricted waveform used in earlier studies can suffice. The fact that using the full waveform in these searches can fail to provide much more accuracy for some systems suggests that including more parameters, such as eccentricity [32] or alternative gravity parameters [41, 42, 43], could keep the accuracy for the other parameters reasonably high, allowing more information from the detection of a wave to be extracted. Gravitational waves can be a powerful tool for constraining

alternative theories of gravitation, in the sense that each event will provide an independent measurement of their parameters.

Even though the spin-coupling effects in the wave amplitude are not yet known at the 2.5PN level, it would be interesting to compare the measurement accuracy we get from a 2.5PN accurate waveform as compared to the 2PN accurate one we used in this study. It has been shown [44, 45] in the case of spinless bodies, that theoretical errors due to the inaccuracy of the waveform can be important for high SNR systems. It would also be interesting to perform the same study for spinning systems.

6.2 Eccentric templates

We presented here a waveform for binaries on eccentric orbits with spin, in the stationary phase approximation. Its advantage over time-domain waveforms is that, while recovering the phase of the original signal with great precision, it is far more efficient to compute. For this reason, it could be a good tool to use for on-the-fly detection in gravitational wave experiments.

Appendix A

Amplitude coefficients for circular waveforms

We give here the plus and cross polarizations we used in the studies described in Chapter 4, in terms of the orbital phase ψ. The plus and cross polarizations of the simplified waveform (SWF) are obtained by keeping only the lowest order in $A_{+}^{(n)}$ and $B_{\times}^{(n)}$, and those of the RWF by keeping only the lowest order of $A_{+}^{(2)}$ and $B_{\times}^{(2)}$. To obtain the SWF and RWF, the function $S(f)$ in Eq. (3.38) should also be set to $S(f) = 1$.

The plus and cross polarization waveforms are:

$$h_{+,\times} = \frac{2GM\nu x}{d_L c^2}\left[\sum_{n\geqslant 0}\left(A_{+,\times}^{(n)}\cos n\psi + B_{+,\times}^{(n)}\sin n\psi\right)\right], \tag{A.1}$$

$$s_i = \left|\hat{\boldsymbol{L}}\times\hat{\boldsymbol{n}}\right|, \tag{A.2}$$

$$c_i = \hat{\boldsymbol{L}}\cdot\hat{\boldsymbol{n}}. \tag{A.3}$$

With the use of the spin-orbit coupling parameter τ defined as:

$$\tau \equiv \frac{c}{GM}\left(\frac{\boldsymbol{S}_1}{m_1} - \frac{\boldsymbol{S}_2}{m_2}\right)\cdot\hat{\boldsymbol{L}}, \tag{A.4}$$

we can write the nonvanishing parameters $A_{+,\times}^{(n)}$ and $B_{+,\times}^{(n)}$, at 2PN level. The value of $\bar{\omega}$ appearing below can be chosen arbitrarily.

$$A_{+}^{(0)} = -\frac{s_i^2}{96}\left(17 + c_i^2\right), \tag{A.5a}$$

$$A_{+}^{(1)} = s_i\sqrt{1-4\nu}\left(-\frac{5}{8} - \frac{c_i^2}{8}\right)x^{1/2} + s_i\tau x + s_i\sqrt{1-4\nu}\left[\frac{19}{64} + \frac{5c_i^2}{16} - \frac{c_i^4}{192} + \nu\left(-\frac{49}{96} + \frac{c_i^2}{8} + \frac{c_i^4}{96}\right)\right]x^{3/2} + s_i\sqrt{1-4\nu}\left(-\frac{5}{8} - \frac{c_i^2}{8}\right)\pi x^2, \tag{A.5b}$$

$$A_+^{(2)} = \left(-1-c_i^2\right) + \left[\frac{19}{6} + \frac{3c_i^2}{2} - \frac{c_i^4}{3} + \nu\left(-\frac{19}{6} + \frac{11c_i^2}{6} + c_i^4\right)\right]x + \Bigg[2\pi\left(-1-c_i^2\right) + \frac{8}{3}\beta\left(3-9c_i^2, 2-10c_i^2\right)\Bigg]x^{3/2} + \Bigg[\frac{11}{60} + \frac{33c_i^2}{10} + \frac{29c_i^4}{24} - \frac{c_i^6}{24} + \nu\left(\frac{353}{36} - 3c_i^2 - \frac{251c_i^4}{72} + \frac{5c_i^6}{24}\right) + \nu^2\left(-\frac{49}{12} + \frac{9c_i^2}{2} - \frac{7c_i^4}{24} - \frac{5c_i^6}{24}\right) - 2\sigma\left(1+c_i^2, 0\right)\Bigg]x^2, \tag{A.5c}$$

$$A_+^{(3)} = s_i\sqrt{1-4\nu}\left(\frac{9}{8} + \frac{9c_i^2}{8}\right)x^{1/2} + s_i\sqrt{1-4\nu}\Bigg[-\frac{657}{128} - \frac{45c_i^2}{16} + \frac{81c_i^4}{128} + \nu\left(\frac{225}{64} - \frac{9c_i^2}{8} - \frac{81c_i^4}{64}\right)\Bigg]x^{3/2} + s_i\sqrt{1-4\nu}\left(\frac{27}{8} + \frac{27c_i^2}{8}\right)\pi x^2, \tag{A.5d}$$

$$A_+^{(4)} = s_i^2\left(1+c_i^2\right)\left(-\frac{4}{3} + 4\nu\right)x + \Bigg[\frac{118}{15} - \frac{16c_i^2}{5} - \frac{86c_i^4}{15} + \frac{16c_i^6}{15} + \nu\left(-\frac{262}{9} + 16c_i^2 + \frac{166c_i^4}{9} - \frac{16c_i^6}{3}\right) + \nu^2\left(14 - 16c_i^2 - \frac{10c_i^4}{3} + \frac{16c_i^6}{3}\right)\Bigg]x^2 \tag{A.5e}$$

$$A_+^{(5)} = s_i^3\sqrt{1-4\nu}\left(\frac{625}{384} - \frac{625\nu}{192}\right)\left(1+c_i^2\right)x^{3/2}, \tag{A.5f}$$

$$A_+^{(6)} = s_i^4\left(1+c_i^2\right)\left(-\frac{81}{40} + \frac{81\nu}{8} - \frac{81\nu^2}{8}\right)x^2, \tag{A.5g}$$

$$A_\times^{(1)} = s_i c_i\sqrt{1-4\nu}\left[-\frac{9}{20} - \frac{3\log 2}{2} + \frac{9}{4}\log\left(\frac{\omega}{\bar{\omega}}\right)\right]x^2, \tag{A.6a}$$

$$A_\times^{(2)} = 12c_i\log\left(\frac{\omega}{\bar{\omega}}\right)x^{3/2}, \tag{A.6b}$$

$$A_\times^{(3)} = s_i c_i\sqrt{1-4\nu}\left[\frac{189}{20} - \frac{27\log(3/2)}{2} - \frac{81}{4}\log\left(\frac{\omega}{\bar{\omega}}\right)\right]x^2, \tag{A.6c}$$

$$B_\times^{(1)} = -\frac{3}{4}s_i c_i\sqrt{1-4\nu}\,x^{1/2} + s_i c_i\tau x + s_i c_i\sqrt{1-4\nu}\left[\frac{21}{32} - \frac{5c_i^2}{96} + \nu\left(-\frac{23}{48} + \frac{5c_i^2}{48}\right)\right]x^{3/2} - \frac{3\pi}{4}s_i c_i\sqrt{1-4\nu}\,x^2, \tag{A.7a}$$

$$B_\times^{(2)} = -2c_i + c_i\left[\frac{17}{3} - \frac{4c_i^2}{3} + \nu\left(-\frac{13}{3} + 4c_i^2\right)\right]x + c_i\left[-4\pi - \frac{4}{3}\beta\left(1+3c_i^2, 3c_i^2\right)\right]x^{3/2} + c_i\Bigg[\frac{17}{15} + \frac{113c_i^2}{30} - \frac{c_i^4}{4} + \nu\left(\frac{143}{9} - \frac{245c_i^2}{18} + \frac{5c_i^4}{4}\right) + \nu^2\left(-\frac{14}{3} + \frac{35c_i^2}{6} - \frac{5c_i^4}{4}\right) - 4\sigma\left(1,0\right)\Bigg]x^2, \tag{A.7b}$$

$$B_{\times}^{(3)} = \frac{9}{4} s_i c_i \sqrt{1-4\nu}\, x^{1/2} + s_i c_i \sqrt{1-4\nu} \left[-\frac{603}{64} + \frac{135 c_i^2}{64} + \nu \left(\frac{171}{32} - \frac{135 c_i^2}{32} \right) \right] x^{3/2} + \frac{27\pi}{4} s_i c_i \sqrt{1-4\nu}\, x^2, \tag{A.7c}$$

$$B_{\times}^{(4)} = c_i s_i^2 \left(-\frac{8}{3} + 8\nu \right) x + c_i \left[\frac{44}{3} - \frac{268 c_i^2}{15} + \frac{16 c_i^4}{5} + \nu \left(-\frac{476}{9} + \frac{620 c_i^2}{9} - 16 c_i^4 \right) + \nu^2 \left(\frac{68}{3} - \frac{116 c_i^2}{3} + 16 c_i^4 \right) \right] x^2, \tag{A.7d}$$

$$B_{\times}^{(5)} = s_i^3 c_i \sqrt{1-4\nu} \left(\frac{625}{192} - \frac{625\nu}{96} \right) x^{3/2}, \tag{A.7e}$$

$$B_{\times}^{(6)} = s_i^4 c_i \left(-\frac{81}{20} + \frac{81\nu}{4} - \frac{81\nu^2}{4} \right) x^2, \tag{A.7f}$$

$$B_{+}^{(1)} = s_i \sqrt{1-4\nu} \left[\frac{11}{40} + \frac{5\log 2}{4} + \left(\frac{7}{40} + \frac{\log 2}{4} \right) c_i^2 + \left(-\frac{15}{8} - \frac{3 c_i^2}{8} \right) \log\left(\frac{\omega}{\bar{\omega}} \right) \right] x^2, \tag{A.8a}$$

$$B_{+}^{(2)} = \left(-6 - 6 c_i^2 \right) \log\left(\frac{\omega}{\bar{\omega}} \right) x^{3/2}, \tag{A.8b}$$

$$B_{+}^{(3)} = s_i \sqrt{1-4\nu} \left[-\frac{189}{40} + \frac{27\log(3/2)}{4} + \frac{81}{8} \log\left(\frac{\omega}{\bar{\omega}} \right) \right] \left(1 + c_i^2 \right) x^2. \tag{A.8c}$$

Bibliography

[1] Lee S. Finn. Detection, measurement, and gravitational radiation. *Phys. Rev. D*, 46(12):5236–5249, Dec 1992.

[2] Curt Cutler. Angular resolution of the lisa gravitational wave detector. *Phys. Rev. D*, 57(12):7089–7102, Jun 1998.

[3] Scott A. Hughes. Untangling the merger history of massive black holes with lisa. *Mon. Not. R. Astron. Soc.*, 331(3):805–816, 2002.

[4] Alberto Vecchio. Lisa observations of rapidly spinning massive black hole binary systems. *Phys. Rev. D*, 70(4):042001, Aug 2004.

[5] Theocharis A. Apostolatos, Curt Cutler, Gerald J. Sussman, and Kip S. Thorne. Spin-induced orbital precession and its modulation of the gravitational waveforms from merging binaries. *Phys. Rev. D*, 49(12):6274–6297, Jun 1994.

[6] Ryan N. Lang and Scott A. Hughes. Measuring coalescing massive binary black holes with gravitational waves: The impact of spin-induced precession. *Phys. Rev. D*, 74(12):122001, 2006.

[7] K. G. Arun, Bala R. Iyer, B. S. Sathyaprakash, Siddhartha Sinha, and Chris Van Den Broeck. Higher signal harmonics, lisa's angular resolution, and dark energy. *Phys. Rev. D*, 76(10):104016, 2007.

[8] Edward K. Porter and Neil J. Cornish. Effect of higher harmonic corrections on the detection of massive black hole binaries with lisa. *Phys. Rev. D*, 78(6):064005, 2008.

[9] Miquel Trias and Alicia M. Sintes. Lisa observations of supermassive black holes: Parameter estimation using full post-newtonian inspiral waveforms. *Phys. Rev. D*, 77(2):024030, 2008.

[10] K G Arun et al. Massive black-hole binary inspirals: results from the lisa parameter estimation taskforce. *Class. Quantum Grav.*, 26(9):094027, 2009.

[11] Steven Weinberg. *Gravitation and Cosmology.* John Wiley & Sons, 1972.

[12] Michele Maggiore. *Gravitational Waves Volume 1: Theory and Experiments*. Oxford University Press, 2008.

[13] Norbert Straumann. *General Relativity With Applications to Astrophysics*. Springer-Verlag, 2004.

[14] B. S. Sathyaprakash and Bernard F. Schutz. Physics, astrophysics and cosmology with gravitational waves. *Living Reviews in Relativity*, 12, 2009. http://www.livingreviews.org/lrr-2009-2.

[15] T. Damour and N. Deruelle. General relativistic celestial mechanics of binary systems. i. the post-newtonian motion. *Ann. Inst. Henri Poincaré*, 43(1):107–132, 1985.

[16] Luc Blanchet. Gravitational radiation from post-newtonian sources and inspiralling compact binaries. *Living Reviews in Relativity*, 9, 2006. http://www.livingreviews.org/lrr-2006-4 .

[17] Curt Cutler and Éanna E. Flanagan. Gravitational waves from merging compact binaries: How accurately can one extract the binary's parameters from the inspiral waveform? *Phys. Rev. D*, 49(6):2658, 1994.

[18] Eric Poisson and Clifford M. Will. Gravitational waves from inspiraling compact binaries: Parameter estimation using second-post-newtonian waveforms. *Phys. Rev. D*, 52(2):848, 1995.

[19] K. Danzmann et al. Lisa - laser interferometer space antenna for the detection and observation of gravitational waves. Technical Report MPQ-208, Max-Planck-Institut für Quantenoptik, 1996.

[20] Antoine Klein and Philippe Jetzer. Spin effects in the phasing of gravitational waves from binaries on eccentric orbits. *Phys. Rev. D*, 81(12):124001, 2010.

[21] B. M. Barker and R. F. O'Connell. Gravitational two-body problem with arbitrary masses, spins, and quadrupole moments. *Phys. Rev. D*, 12(2):329–335, 1975.

[22] Luc Blanchet, Alessandra Buonanno, and Guillaume Faye. Higher-order spin effects in the dynamics of compact binaries. ii. radiation field. *Phys. Rev. D*, 74(10):104034, 2006.

[23] K G Arun, Luc Blanchet, Bala R Iyer, and Moh'd S S Qusailah. The 2.5pn gravitational wave polarizations from inspiralling compact binaries in circular orbits. *Class. Quantum Grav.*, 21(15):3771–3801, 2004.

[24] K. G. Arun, Alessandra Buonanno, Guillaume Faye, and Evan Ochsner. Higher-order spin effects in the amplitude and phase of gravitational waveforms emitted by inspiraling compact binaries: Ready-to-use gravitational waveforms. *Phys. Rev. D*, 79(10):104023, 2009.

[25] Thibault Damour, Archamveedu Gopakumar, and Bala R. Iyer. Phasing of gravitational waves from inspiralling eccentric binaries. *Phys. Rev. D*, 70(6):064028, 2004.

[26] Lawrence E. Kidder, Clifford M. Will, and Alan G. Wiseman. Spin effects in the inspiral of coalescing compact binaries. *Phys. Rev. D*, 47(10):R4183, 1993.

[27] Lawrence E. Kidder. Coalescing binary systems of compact objects to $(\text{post})^{5/2}$-newtonian order. v. spin effects. *Phys. Rev. D*, 52(2):821, 1995.

[28] László Á Gergely. Spin-spin effects in radiating compact binaries. *Phys. Rev. D*, 61:024035, 1999.

[29] Zoltán Keresztes, Balázs Mikóczi, and László Á Gergely. Kepler equation for inspiralling compact binaries. *Phys. Rev. D*, 72:104022, 2005.

[30] László Á Gergely, Zoltán I Perjés, and Mátyás Vasúth. Spin effects in gravitational radiation back reaction. iii. compact binaries with two spinning components. *Phys. Rev. D*, 58:124001, 1998.

[31] Balázs Mikóczi, Mátyás Vasúth, and László Á Gergely. Self-interaction spin effects in inspiralling compact binaries. *Phys. Rev. D*, 71:124043, 2005.

[32] Nicolas Yunes, K. G. Arun, Emanuele Berti, and Clifford M. Will. Post-circular expansion of eccentric binary inspirals: Fourier-domain waveforms in the stationary phase approximation. arXiv:0906.0313, 2009.

[33] Ronald Rieth and Gerhard Schäfer. Spin and tail effects in the gravitational-wave emission of compact binaries. *Class. Quantum Grav.*, 14:2357–2380, 1997.

[34] Norbert Wex. The second post-newtonian motion of compact binary-star systems with spin. *Class. Quantum Grav.*, 12:983–1005, 1995.

[35] Archamveedu Gopakumar and Bala R. Iyer. Second post-newtonian gravitational wave polarizations for compact binaries in elliptical orbits. *Phys. Rev. D*, 65(084011):084011, 2002.

[36] Antoine Klein, Philippe Jetzer, and Mauro Sereno. Parameter estimation for coalescing massive binary black holes with lisa using the full 2-post-newtonian gravitational waveform and spin-orbit precession. *Phys. Rev. D*, 80(6):064027, 2009.

[37] Alessandra Buonanno, Gregory B. Cook, and Frans Pretorius. Inspiral, merger, and ring-down of equal-mass black-hole binaries. *Phys. Rev. D*, 75(12):124018, 2007.

[38] John G. Baker, James R. van Meter, Sean T. McWilliams, Joan Centrella, and Bernard J. Kelly. Consistency of post-newtonian waveforms with numerical relativity. *Phys. Rev. Lett.*, 99(18):181101, 2007.

[39] P. Chang, L. E. Strubbe, K. Menou, and E. Quataert. Fossil gas and the electromagnetic precursor of supermassive binary black hole mergers. arXiv:0906.0825, 2009.

[40] Alberto Sesana, Marta Volonteri, and Francesco Haardt. The imprint of massive black hole formation models on the lisa data stream. *Mon. Not. R. Astron. Soc.*, 377(4):1711–1716, 2007.

[41] Emanuele Berti, Alessandra Buonanno, and Clifford M. Will. Estimating spinning binary parameters and testing alternative theories of gravity with lisa. *Phys. Rev. D*, 71(8):084025, Apr 2005.

[42] K G Arun and Clifford M Will. Bounding the mass of the graviton with gravitational waves: effect of higher harmonics in gravitational waveform templates. *Class. Quantum Grav.*, 26(15):155002, 2009.

[43] Adamantios Stavridis and Clifford M. Will. Bounding the mass of the graviton with gravitational waves: Effect of spin precessions in massive black hole binaries. *Phys. Rev. D*, 80(4):044002, 2009.

[44] Curt Cutler and Michele Vallisneri. Lisa detections of massive black hole inspirals: Parameter extraction errors due to inaccurate template waveforms. *Phys. Rev. D*, 76(10):104018, 2007.

[45] Richard Umstatter and Massimo Tinto. Bayesian comparison of post-newtonian approximations of gravitational wave chirp signals. *Phys. Rev. D*, 77(8):082002, 2008.